Retarded Decays of Low-Lying (~30 keV) Mössbauer Levels as a Result of Their Combined Structure

P. I. Romasheva

Institute of Theoretical and Experimental Physics, Bol'shaya Cheremushkinskaya ul. 25,
Moscow, 117259 Russia
Received June 26, 2000; in final form, July 24, 2000

The possibility that "combined" levels with splitting considerably smaller than the natural width exist in slightly deformed nuclei with odd mass numbers is considered within the framework of the shell model. Such a structure of Mössbauer levels does not contradict the available spectroscopic data but, rather, explains large time delays and conversion coefficients for their decay. Experimental verification of the hypothesis is discussed. © 2000 MAIK "Nauka/Interperiodica".

PACS numbers: 23.20.Nx; 21.10.Tg; 21.60.Cs

Recently, new aspects have arisen in experimental [1–3] and theoretical [4–7] investigations of the fundamental nuclear process of resonance gamma quanta scattering. Experimental data on the frequency spectra of Mössbauer gamma radiation scattered by the 14.4 keV level of the $^{57}_{26}\text{Fe}_{31}$ nucleus [1, 2] indicate that the spectrum of scattered radiation is appreciably narrower than is predicted by theoretical estimates. These estimates [4–7] were made under the assumption that the scattering of gamma quanta does not depend on the presence of an incoherent decay channel through internal conversion for the 14.4 keV level. Note that the inelastic scattering of gamma quanta through the conversion channel differs in character from the elastic scattering, as immediately follows from the calculations [4]. In contrast, it is assumed in [7] (where the results for frequency spectra coincide with the ones obtained in [4, 6]) that the dynamics of the processes in the coherent and incoherent channels should be identical. The results obtained in [4] indicate the necessity of including the structure of an excited nuclear level if it decays through many channels. The necessity of such an inclusion also follows from experiment [3], where radioactive decay retardation was observed for the $^{119}_{50}\text{Sn}_{69}$ isomer, below which the Mössbauer 23.87 keV level lies.

Isomerism and lifetimes of Mössbauer levels in odd-*A* nuclei. It is known that retardation of the decay of classical nuclear isomers by 18–20 orders of magnitude, as compared to the characteristic nuclear times $t_N \sim 10^{-14}–10^{-15}$ s, is due to the large (~3–4) angular momenta carried away by the gamma quantum upon level de-excitation.

The available spectroscopic data on Mössbauer levels (MLs) ($E \sim 100$ keV) [8] demonstrate the following features. First, MLs concentrate in odd-*A* nuclei. Second, the gamma transition to the ground state proceeds with parity conservation and is accompanied by a change in spin of unity in the majority of cases, and only ~10% of transitions proceed either with a change in spin of two units or with parity change. Third, the states with energies ~10–60 keV decay predominantly through internal conversion. Experimental values of the conversion coefficients a_c in the energy range below 30 keV exceed the calculated values [9] by a factor from several units to several tens. These facts allow one to conclude that the majority of MLs do not satisfy the generally accepted definition of isomers. Nevertheless, the lifetimes of these states vary from 1 ns to hundreds of nanoseconds and, therefore, are ~6–8 orders of magnitude longer than t_N.

Possible structure of low-lying levels of some odd-*A* nuclei in the shell model. The decay retardation and the large a_c values may probably be explained by the structure of MLs. Let us choose the MLs with $E \sim 30$ keV for a detailed analysis and use the well-known positions of the nuclear shell model [10, 11], together with Fig. 1, for describing the structure of the ground ($|n_0\rangle$) and the first excited states. The analysis was performed for all nuclei presented in the table. Let us consider some cases.

The 14.4 keV level in $^{57}_{26}\text{Fe}_{31}$. The number of neutrons is $N = 31$, and the number of protons is $Z = 26$ (Fig. 2). Twenty-eight neutrons completely fill the first and second oscillator levels (OLs) and the $1f_{7/2}$ subshell of the third OL. The last three neutrons are at the $2p_{3/2}$ subshell of the third OL. Here, 7/2 and 3/2 are the total angular momenta j of the indicated subshells. According to the tight *jj*-coupling rule, the total nuclear angular momentum J and the spin I_0 in the ground state $|n_0\rangle$ are determined by the j value of the last odd nucleon and should be equal to 3/2, and parity should be negative. The experiment gives evidence for spin
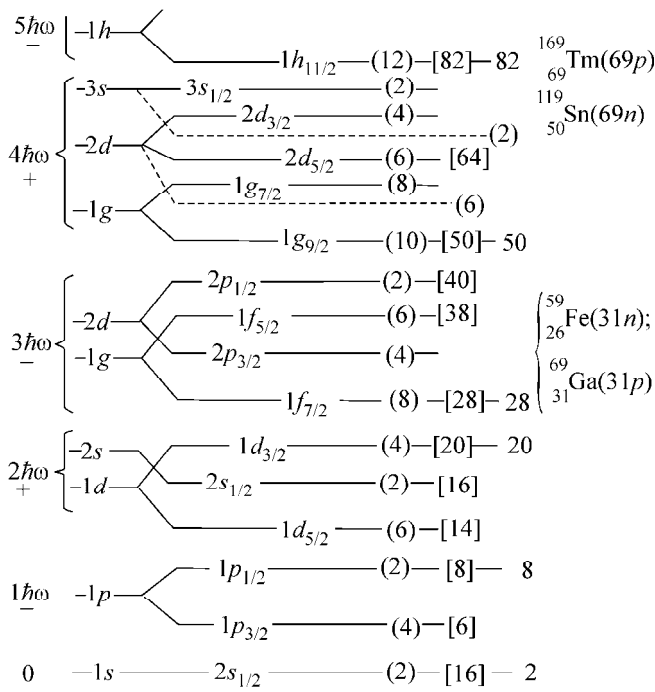
Fig. 1. The level scheme in the shell model [11]. The neutron and proton schemes are identical up to $N = 50$. The dashed lines show the neutron shells for $N > 50$.
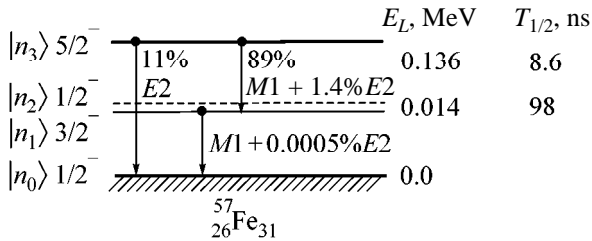

Fig. 2. Low-lying levels of $^{57}_{26}\text{Fe}_{31}$ [12].

"zombie" and denote it by $(|n_2\rangle, E_2)$. The shell model does not determine energy splitting for the states $|n_1\rangle$ and $|n_2\rangle$, but it is obviously small. It is quite possible that $\delta E = |E_1 - E_2| \ll \Gamma$ (Γ is the natural width of the E_1 level), because $|n_1\rangle$ and $|n_2\rangle$ are degenerate in the tight-coupling limit.

The configuration $\{1f_{5/2}-\}^{-1}$ of the last odd neutron, with two neutrons completely paired in the $\{2p_{3/2}-\}^2$ configuration, is likely to be the first purely one-particle excited state. This state is denoted by $(|n_3\rangle, E_3)$. All neutron transitions in $^{57}_{26}\text{Fe}_{31}$ occur within one OL and with close values of the total angular momentum J. This is apparently the reason why the classical isomeric state is absent for this nucleus. The experiment gives the following level ordering in $^{57}_{26}\text{Fe}_{31}$: $(1/2^-, |n_0\rangle)$; $(3/2^-, 14.4$ keV, $T_{1/2} = 97$ ns, $|n_1\rangle)$; $(5/2^-, 136.4$ keV, $T_{1/2} = 8.6$ ns, $|n_3\rangle)$. The multipolarities of the gamma transitions $|n_3\rangle \longrightarrow |n_1\rangle$, $|n_1\rangle \longrightarrow |n_0\rangle$, and $|n_3\rangle \longrightarrow |n_0\rangle$ are $M1 + 1.4\%E2$, $M1 + \sim0.0005\%E2$, and E_2, respectively. The ratio of gamma intensities is $B(|n_3\rangle \longrightarrow |n_0\rangle)/B(|n_3\rangle \longrightarrow |n_1\rangle) \sim 10\%$.

The assumption about the combined 14 keV level does not contradict the above spectroscopic data but, rather, is invoked to explain these data. According to the selection rules, the gamma transition $|n_2\rangle \longrightarrow |n_0\rangle$ between two states with identical spins and parities can be of the $E0$, $M1$, or $E2$ type [10]. Because of the transverse character of electromagnetic field, the matrix element for $E0$ radiation is zero, so that de-excitation occurs through conversion. The population of the $|n_2\rangle$ state due to the cascade transition from the $|n_3\rangle$ state (122 keV, $M1 + 1.4\%E2$ type) is low, but the presence of the $|n_2\rangle$ state may be evident from the presence of weak quadrupolal 122 keV radiation, the decay retardation of the combined $|n_1\rangle \oplus |n_2\rangle$ level, and the large experimental a_c value. The time delay for the $|n_3\rangle$ state is much shorter than for the $|n_1\rangle \oplus |n_2\rangle$ state but is considerable compared to t_N; it can be explained by the "mild" selection rules for the orbital quantum number l in the shell model. According to [10], magnetic dipole radiation is possible only for the transitions satisfying the condition $|l_i - l_k| < |I_i - I_k| - 1$; i.e., the $\Delta l = 0$ transitions are allowed: $p_{1/2} \longleftrightarrow p_{3/2}$, $d_{3/2} \longleftrightarrow d_{5/2}$, $f_{5/2} \longleftrightarrow f_{7/2}$. The transitions $s_{1/2} \longleftrightarrow d_{3/2}$, $p_{3/2} \longleftrightarrow f_{5/2}$, etc. are l-forbidden; the 122-keV transition is among the latter.

The 23 keV level in the $^{119}_{50}\text{Sn}_{69}$ nucleus. The nucleus contains 69 neutrons. The experiment indicates the following level ordering (Fig. 3): $(1/2^+, |n_0\rangle)$; $(3/2^+, 23$ keV, $T_{1/2} = 17.8$ ns, $|n_1\rangle)$; $(11/2^-, 89$ keV, $T_{1/2} = 293$ days, $|n_3\rangle)$. According to Fig. 1, the neutron configuration is $\{2d_{3/2}+\}^3$ above the closed subshell $\{3s_{1/2}+\}^2$. However, the $|n_0\rangle$ state is "anomalous" and not purely one-particle. It can be constructed either as the

$I_0 = 1/2$ and negative parity, i.e., for the $1/2^-$ state. If there are several neutrons or protons at the last subshell, the shell model does not exclude the larger number of different J values satisfying the Pauli exclusion principle (see Table 6 in [10]) and treats them as anomalous from the viewpoint of classical positions of the shell model. In the case under consideration, the angular momenta of three neutrons can give $J = 1/2$ in the combination $3/2 \oplus 3/2 \oplus 3/2 \propto 1/2$, where $\oplus$ means the composition of angular momenta. The first excited state $(3/2^-)$ also cannot be treated as a strictly one-particle state. It can be constructed in two ways: (1) from one neutron in the $\{1f_{5/2}-\}^{-1}$ configuration and two neutrons in the $\{2p_{3/2}-\}^2$ configuration, $3/2 \oplus 3/2 \oplus 5/2 \propto 3/2$, and (2) from three neutrons in the $\{2p_{3/2}-\}^3$ configuration, $3/2 \oplus 3/2 \oplus 3/2 \propto 3/2$. Denote this state by $(|n_1\rangle, E_1)$. Therefore, one more excited state can be constructed as $3/2 \oplus 3/2 \oplus 5/2 \propto 1/2$. Let us call this state

$\{2d_{3/2}+\}^4 \oplus \{3s_{1/2}+\}^1$ configurations or by forming the nuclear $1/2^+$ state through the combination $3/2 \oplus 3/2 \oplus 3/2 \propto 1/2$. The first excited $3/2^+$ state $|n_1\rangle$ may result from the one-particle state $3/2 \oplus 3/2 \oplus 3/2 \propto 3/2$ ($|n_1\rangle$) or from the interaction of one unpaired neutron with two neutrons of the lower subshell: $3/2 \oplus 1/2 \oplus 1/2 \propto 3/2$ ($|n_1\rangle$). In the latter case, this interaction may result in $3/2 \oplus 1/2 \oplus 1/2 \propto 1/2$ ($|n_2\rangle$), which affords the combined level $|n_1\rangle \oplus |n_2\rangle$ and, hence, the large time delay and the a_c value for the transition $|n_1\rangle \oplus |n_2\rangle \longrightarrow |n_0\rangle$. A normal, purely one-particle excited state forms upon the transition of one neutron from the $3s_{1/2}+$ subshell to the $1h_{11/2}-$ subshell to give the nuclear ($11/2^-$, $|n_3\rangle$) state. The $11/2^-$ state is a classical isomer manifesting itself in the $|n_3\rangle \longrightarrow |n_1\rangle \oplus |n_2\rangle$ transition.

The table demonstrates the existence of a possible combined level in other nuclei. Below, a detailed description of the level structure for the relevant mirror nuclei is omitted and only the basic results are presented.

The $|n_0\rangle$ state of the $^{69}_{31}\text{Ga}_{38}$ nucleus is one-particle. The combination of the configurations $\{1f_{5/2}\}^1 \oplus \{2p_{3/2}\}^2$ determines the spin of the $|n_1\rangle$ state. The ($3/2^-$, $|n_2\rangle$) state is constructed from the same combination and likely does not form the combined level. The $T_{1/2}$ value for the first excited state is small (<0.07 ps), as also is $a_c \sim 5 \times 10^{-2}$.

The $^{169}_{69}\text{Tm}_{100}$ nucleus has a one-particle ground state $1/2^+$ $|n_0\rangle$. The combination of configurations $\{3s_{1/2}\}^1 \oplus \{2d_{3/2}\}^2$ can determine spins of the $|n_1\rangle$ and $|n_2\rangle$ states. A combined level with energy $E_1 = 8$ keV is possible. Note that this nucleus is not described by the shell model, because the $11/2^-$ isomer is absent, in contrast to the $^{119}_{50}\text{Sn}_{69}$ nucleus.

Discussion. The following regularities of formation of the first excited levels are noteworthy. Whenever three nucleons are at the unfilled subshell or a one-particle state is near the $1s_{1/2}$, $2s_{1/2}$, $3s_{1/2}$, and $2p_{1/2}$ states, three nucleons can probably be combined in such a way as to form "split" states with different J values. According to the Pauli exclusion principle, these combinations correspond to different nuclear eigenfunctions providing different nuclear characteristics. In the tight-coupling approximation, the states described by these combinations are degenerate. In a real nucleus, the pairing effect and interaction between all pairs of particles remove the degeneracy. Since this interaction cannot be taken into account in terms of the meson field, the shell model fails to give the splitting values.

A qualitative estimate can be obtained from the experimental data on the hyperfine interaction for the magnetic dipole transitions involving the 14.4 keV level of the $^{57}_{26}\text{Fe}_{31}$ nucleus. Knowing the maximum magnetic splitting of $\sim 80\Gamma$ for iron in a magnetic field of $\sim 10^6$ Oe induced by electrons and taking into account that the nuclear magneton is $\sim 2 \times 10^3$ times smaller than the Bohr magneton, we obtain the electromagnetically induced energy splitting $\delta E \sim 0.04\Gamma$ for the combined level.

Table

Mössbauer nucleus	$^{57}_{26}\text{Fe}$	$^{73}_{32}\text{Ge}$	$^{83}_{36}\text{Kr}$	$^{129}_{53}\text{I}$	$^{191}_{63}\text{Eur}$	$^{119}_{50}\text{Sn}$	$^{133}_{56}\text{Ba}$	$^{149}_{62}\text{Sm}$	$^{161}_{66}\text{Dy}$
E_1, keV	14.4	13.3	9.4	27.8	21.5	23.9	12.3	22.5	25.7
a_c	8.5	1095	19.6	5.1	28.6	5.1	110	50	2.9
$T_{1/2}$, ns	97.8	2953	147	16.8	9.4	17.9	8.1	5.1	28.2
Combined level	+	+	+	+	+	+	+	+	−
Remarks									~~SM~~
Mirror nucleus	$^{69}_{31}\text{Ga}$	$^{93}_{41}\text{Nb}$	$^{107.9}_{47}\text{Ag}$	$^{97}_{44}\text{Ru}$	$^{112}_{49}\text{In}$	$^{169}_{69}\text{Tm}$	$^{191}_{77}\text{Ir}$	$^{225}_{87}\text{Fr}$	$^{243}_{95}\text{Am}$
E_1, keV	320	30	~100	108		8.4	82		2.3
a_c				0.01	Beta-active nucleus	29.1	~1	Beta-active nucleus	0.2
$T_{1/2}$, ns	~0.07	13.6 y	~3	0.23		4.0	4		1.4
Combined level	−	−	+	−	−	+	+	−	−
Remarks	Anomalous level	Isomer	+	Anomalous level	~~SM~~	ML	ML	~~SM~~	~~SM~~

Note: Sign ~~SM~~ indicates that the first levels cannot be constructed in the shell model.
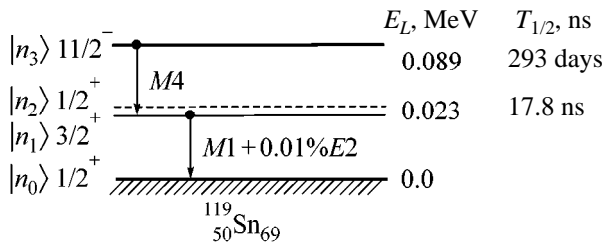
Fig. 3. Low-lying levels of $^{119}_{50}Sn_{69}$ [12].

To describe the ground and low-lying excited states of nuclei, the possible combinations (pairing and jj coupling of three nucleons) are considered for the distribution of nucleons among two $2d_{3/2}+$ and $3s_{1/2}+$ subshells of the fourth OL and the $1h_{11/2}-$ subshell of the fifth OL. The occurrence of splitting and, as a consequence, a large time delay and a_c value can be assumed for the Mössbauer level, although it is difficult to explain this within the framework of the classical shell model because of the highly nonspherical shape of nuclei [10]. The closeness of the next OL with a high J value is responsible for the existence of classical isomeric states in these nuclei. When nucleon transitions occur within the same OL and for close values of the total angular momenta J, the classical isomeric states are not realized, as in the case of $^{57}_{26}Fe_{31}$. A comparison of the mirror nuclei shows that the odd-N nuclei are less deformed and the shell model is more suitable than for the odd-Z nuclei, which are neutron-excessive and more deformed.

The possibility of the combined levels existing is presented in the table, but the following remarks should be made. (i) In most cases, the combined level occurs if the $|n_1\rangle$ level can be considered not only as purely one-particle, but also as anomalous. The splitting of anomalous states mixes in the one-particle state. (ii) If the excited state can only be anomalous, not all variants may be possible for the composition of angular momenta j, so that the combined level does not occur, as in the $^{69}_{31}Ga_{38}$ nucleus. (iii) The pairing effect is more preferable for one odd nucleon with high $J \geq 5/2$ and can determine the spin of the first excited state, as takes place for the isomeric $1/2^-$ state of the $^{93}_{41}Nb_{52}$ nucleus, thereby preventing the formation of the combined level. Under the assumption that $\delta E \ll \Gamma$, the splitting does not contradict the spectroscopic data (spin ordering, transition multiplicity) for the levels of interest (this is illustrated in detail for $^{57}_{26}Fe_{31}$) but rather explains the large time delays and a_c coefficients for the first excited states. The currently available nuclear spectroscopic methods of determining the spin, parity, multipolarity, and a_c cannot identify the combined state $|n_1\rangle \oplus |n_2\rangle$.

The Mössbauer methods that use scattered radiation are more preferable, because the nuclear and solid-state origins of the line shifts and shapes often cannot be differentiated in the conventional transmission mode. According to the theoretical estimates taking into account a combined structure of the 14 keV radiation from $^{57}_{27}Co_{30}$ [13], the line shape of Mössbauer radiation from a source is rather informative. In this case, the scattered radiation line not only loses the Breit–Wigner shape, but also tangibly narrows in direct proportion to the contribution of the conversion channel to the excited-state decay. These preliminary estimates [13] explain most important result obtained in experiments [1, 2]. Experiments on the line shapes of the Mössbauer radiation scattered from the $^{57}_{26}Fe_{31}$, $^{73}_{32}Ge_{41}$, $^{83}_{36}Kr_{47}$, $^{129}_{53}I_{76}$, $^{119}_{50}Sn_{69}$, $^{169}_{69}Tm_{100}$, $^{133}_{56}Ba_{77}$, and $^{191}_{77}Ir_{114}$ nuclei are also of interest. The experiments on the line shapes should be carried out using a source, scatterer, and analyzer with a line width close to natural.

Recent observation of an increase in $T_{1/2}$ of the $|n_3\rangle$ (our notation) level in the $^{119}_{50}Sn_{69}$ nucleus in the presence of resonance nuclei can be explained if one assumes the existence of a combined $|n_1\rangle \oplus |n_2\rangle$ level. Indeed, if the population of the $|n_1\rangle$ state in a system of quantum states $|n_1\rangle$, $|n_2\rangle$, and $|n_3\rangle$ somehow increases, the gamma transition $|n_3\rangle \longrightarrow |n_1\rangle \oplus |n_2\rangle$ will be more retarded. On additional population of the $|n_1\rangle$ state $(3/2^+)$, the $|n_3\rangle \longrightarrow |n_1\rangle \oplus |n_2\rangle$ transition proceeds only through the $|n_3\rangle \longrightarrow |n_2\rangle$ channel, which is clearly more retarded. For example, if the decay of the Mössbauer source ^{119m}Sn leads to the accumulation of additional $^{119}_{50}Sn_{69}$ nuclei, the back resonance scattering of the 23 keV quanta will result in an increase in the population of the $|n_1\rangle$ state in the source. This process may be responsible for the increase in $T_{1/2}$ of the $|n_3\rangle$ level observed in [3] for "old" tin Mössbauer sources. As far as I know, an experiment with non-Mössbauer ^{119m}Sn sources was not performed. The system of low-lying levels considered allows one to propose a number of experiments of the "[3] type": $^{57}_{26}Fe_{31}$, $^{73}_{32}Ge_{41}$, $^{83}_{36}Kr_{47}$, $^{107, 109}_{47}Ag_{60, 62}$, $^{119}_{50}Sn_{69}$, $^{133}_{56}Ba_{77}$, and $^{151}_{63}Eu_{88}$. An analysis of the effect of excitation on the $T_{1/2}$ values of the $|n_3\rangle$ levels of these nuclei can serve as an experimental verification of the existence of combined levels. The excitation may be provided not only by Mössbauer scattering, but also by the bremsstrahlung with a band edge slightly above the first excited state.

Radioactive Nuclide Diagnostics, Faculty of Chemistry, Moscow State University.

REFERENCES

1. P. I. Romasheva and V. M. Novikov, Vopr. At. Nauki Tekh., Ser. Fiz. Tekh. Yad. Reakt., Spec. Iss. TIYaS-XI, 91 (1997).

2. P. I. Romasheva, V. M. Novikov, and S. A. Kutilin, Izv. Ross. Akad. Nauk, Ser. Fiz. **62**, 2282 (1998).

3. S. K. Godovikov, Pis'ma Zh. Éksp. Teor. Fiz. **68**, 599 (1998) [JETP Lett. **68**, 629 (1998)].

4. P. I. Romasheva and D. V. L'vov, Vopr. At. Nauki Tekh., Ser. Teor. Prikl. Fiz. **2–3**, 6 (1997).

5. P. I. Romasheva and D. V. L'vov, Izv. Akad. Nauk, Ser. Fiz. **63**, 232 (1999).

6. P. I. Romasheva, in *Proceedings of the 1st Moscow International School of Physics of the Institute of Theoretical and Experimental Physics, Modern Problems of Nuclear Physics, Physics and Chemistry of Condensed Media, Zvenigorod, 1998.*

7. F. S. Dzheparov and D. V. L'vov, in *Proceedings of the 1st Moscow International School of Physics of the Institute of Theoretical and Experimental Physics, Modern Problems of Nuclear Physics, Physics and Chemistry of Condensed Media, Zvenigorod, 1998.*

8. *A Reference Book of Nuclides* (TsNIIATOM, Moscow, 1995).

9. *Gamma Rays*, Ed. by L. A. Sliv (Akad. Nauk SSSR, Leningrad, 1961).

10. M. Goeppert-Mayer and J. Jensen, *Elementary Theory of Nuclear Shell Structure* (Wiley, New York, 1955; Inostrannaya Literatura, Moscow, 1958).

11. *Alpha-, Beta-, and Gamma-Ray Spectroscopy*, Ed. by K. Siegbahn (North-Holland, Amsterdam, 1968; Atomizdat, Moscow, 1968), Vol. 2.

12. *Table of Isotopes*, Ed. by C. M. Lederer and V. S. Shorley (Wiley, New York, 1978).

13. A. V. Volodin, Talk Given at the Conference of Young Scientists, Institute of Theoretical and Experimental Physics, 1999.

Translated by R. Tyapaev

Excitation of an Atom in a Nonstationary Cavity

Yu. E. Lozovik*, N. B. Narozhnyĭ*, and A. M. Fedotov**

* Institute of Spectroscopy, Russian Academy of Sciences, Troitsk, Moscow region, 142092 Russia
* e-mail: lozovik@isan.troitsk.ru
** Moscow Institute of Engineering Physics, Kashirskoe sh. 31, Moscow, 115409 Russia
** e-mail: fedotov@cea.ru
Received June 27, 2000

The effect of excitation of an atom in an initially photon-free nonstationary cavity is predicted. Two excitation mechanisms are considered, both different from the trivial absorption of photons created due to the nonstationary Casimir effect. The first one is based on the fact that the photon states appear simultaneously with atomic excitation if the characteristic time of cavity nonstationarity is of the same order as the atomic transition time. The second one is associated with the "shake-up" effect caused by the modulation of the atomic ground-state Lamb shift upon a fast change in the cavity parameters. The presence of an atom in the nonstationary cavity affects the photon creation process. In particular, it changes the average number of generated photons and removes the constraint (inherent in the nonstationary Casimir effect) that only an even number of photons can be created. In addition, a new mechanism of photon generation associated with the shake-up effect appears. © 2000 MAIK "Nauka/Interperiodica".

PACS numbers: 31.30.Jv; 32.80.–t

In this work, we consider the effect of atomic excitation in an initially photon-free nonstationary cavity. An atom may either be confined in the cavity due to a trap formed by external fields or fly through the cavity in a cold rarefied beam. It turns out that atomic excitation, generally, is not restricted to the absorption of photons created as a result of the nonstationary Casimir effect (NCE). In particular, there is a new mechanism that is associated with a change in the electron self-energy part upon a fast change in the cavity size, i.e., the "shake-up" effect. In addition, the presence of atom affects the photon creation process in a nonstationary cavity, in particular, by changing the average number of created photons and removing the constraint (inherent in the NCE) that only an even number of photons can be created. We will also discuss a new mechanism of photon generation associated with an abrupt change in the dressed states of atom upon shake-up in a nonstationary cavity.

Our consideration is based on a simple model of a two-level atom interacting with a single nonstationary mode of a quantized electromagnetic field. The Hamiltonian of such a two-level system has the form

$$H = E_0 \frac{1 + \sigma_3}{2} + \omega(t) a^\dagger a + i \frac{\dot{\omega}(t)}{4\omega(t)} (a^2 - a^{\dagger 2})$$
$$+ \lambda(\sigma_+ + \sigma_-)(a + a^\dagger), \tag{1}$$

where E_0 is the transition frequency of the system;[1]

---
[1] The system of units used in this work is $\hbar = 1$.

$\omega(t)$ is the time-dependent (through the cavity parameters) frequency of the field mode; $\sigma_3 = 2\sigma_+\sigma_- - 1$ and $\sigma_\pm$ are the Pauli matrices acting in the space of states of the two-level atom; a and $a^\dagger$ are the annihilation and creation operators of the photon mode; and λ is the coupling constant. Recall that the nonresonance part $\lambda(\sigma_- a + \sigma_+ a^\dagger)$ of the interaction between atom and field can be omitted in the vicinity of the resonance, after which the model reduces to the so-called generalized Janes–Cummings model [1] or, at $\omega = \text{const}$, to the exactly integrable standard Janes–Cummings model [2, 3]. Finally, at $\lambda = 0$, our Hamiltonian reduces to the Hamiltonian modeling the NCE for the chosen field mode [4]. Clearly, as distinct from the analogous problem with a stationary cavity, quantitatively correct results cannot, generally, be obtained in the one-mode approximation, even in the vicinity of the resonance. The reason is that the field modes strongly interact with each other in the nonstationary cavity, so that the properties of a "dressed" resonance mode may differ appreciably from an oscillator. Nevertheless, we use a one-mode approximation, because such a simple model allows one to reveal the main qualitative features of the interaction between an atom and a nonstationary quantized electromagnetic field in the cavity.

Let the frequency of the mode change from ω_1 to ω_2 in a finite time τ. Since Hamiltonian (1) is time-independent at $t \longrightarrow \pm\infty$, one can introduce the stationary in- and out-states of the system. In the absence of the interaction between atom and field, i.e., at $\lambda = 0$, the rel-

evant operators of photon creation and annihilation are related by the Bogoliubov transformation

$$a_{\text{out}} = \alpha_\infty a_{\text{in}} + \beta_\infty a_{\text{in}}^\dagger.$$

At $\beta_\infty \neq 0$, the out- and in-states do not coincide with each other. This signifies that photons are created from vacuum in the nonstationary cavity, i.e., that the NCE occurs. If the initial state $|0, \downarrow\rangle$ corresponds to the atomic ground state and the absence of photons in the cavity, then the average number of created photons is $\bar{N} = |\beta_\infty|^2$. It is worth noting that the NCE is fully caused by the third term, proportional to $\dot{\omega}$, in Hamiltonian (1).

At $\lambda \neq 0$, the atom interacts with the nonstationary field in the cavity and is capable of being excited. Let us first consider this effect within the framework of the generalized Janes–Cummings model [i.e., without taking into account the off-resonance terms in Eq. (1)], assuming that the characteristic time τ of changing the frequency $\omega(t)$ is much shorter than all remaining characteristic times of the problem; i.e., $\tau \ll E_0^{-1}$, ω_1^{-1}, ω_2^{-1} (sudden approximation). Under these assumptions, the problem allows an exact solution and does not require the use of perturbation theory for the coupling constant λ. According to the general rules of the theory of sudden perturbations, the probability of a transition with atomic excitation and creation of n photons is equal to the square of the modulus of excitation amplitude:

$$A_{n\uparrow} = {}_{\lambda\omega_2}\langle n, \uparrow | e^{-iW} | 0, \downarrow \rangle, \tag{2}$$

where the operator W of "sudden" action caused by the Casimir term in Hamiltonian (1) has the form

$$W = \frac{i\Theta}{2}(a^2 - a^{\dagger 2}), \quad \Theta = \frac{1}{2}\int_{-\infty}^{\infty} \frac{\dot{\omega}}{\omega} dt = \frac{1}{2}\ln\left(\frac{\omega_2}{\omega_1}\right),$$

and $|n, \uparrow\rangle_{\lambda\omega_2}$ is the exact (dressed) stationary state of the standard Janes–Cummings model (see [2]). Note that the ground state $|0, \downarrow\rangle$ of the system cannot be dressed and cannot suffer the Lamb shift (an artefact of the model).

One can show that amplitude (2) is nonzero only for the odd values $n = 2j + 1$; the corresponding total probability of atomic excitation is

$$w_\uparrow = \frac{2\xi^2\sqrt{\rho}(\rho-1)^2}{(1+\rho)^3} \sum_{j=0}^{\infty} \frac{(2j+1)!!}{2^j j!}$$
$$\times \frac{1}{\frac{1}{2} + 4\xi^2(j+1) + \sqrt{\frac{1}{4} + 2\xi^2(j+1)}} \left(\frac{\rho-1}{\rho+1}\right)^{2j}, \tag{3}$$

where $\xi = \lambda/\Delta_2$ and $\Delta_2 = E_0 - \omega_2$. In the weak coupling limit $\xi \ll 1$, one has

$$w_\uparrow \approx \xi^2 \bar{N}, \quad \bar{N} = (\rho-1)^2/4\rho. \tag{4}$$

Here, $\bar{N}$ has the meaning of the average number of Casimir photons that would be created in the absence of atom. It is seen from Eq. (4) that in the weak coupling limit the probability of atomic excitation is a simple product of the probability $(\lambda/\Delta_2)^2$ of photon absorption by atom and the average number $\bar{N}$ of photons created due to the NCE. This signifies that the atom in this model is excited only through the trivial process of absorption of the created Casimir photons. This conclusion is not specific solely to the weak coupling limit, because the $e^{-iW}|0, \downarrow\rangle$ state appearing in amplitude (2) exactly coincides with the state that would be initial if the atom were placed in the cavity after the latter had again become stationary and the NCE had already occurred. Thus, in the sudden approximation of the generalized Janes–Cummings model, the interaction of the unexcited atom amounts to the absorption of Casimir photons. This inference is also confirmed by the fact that, as one can readily verify, the average number of photons created in the presence of atom is equal, for any λ, to

$$\bar{n} = \sum_{n=0}^{\infty} n(|A_{n\downarrow}|^2 + |A_{n\uparrow}|^2) = \bar{N}_{\text{NCE}} - w_\uparrow, \tag{5}$$

where the amplitude $A_{n\downarrow}$ of creation of n photons without atomic excitation is given by the expression analogous to Eq. (2). The fact that in the resonance approximation the atomic excitation in an initially empty and instantaneously nonstationary cavity amounts to the absorption of Casimir photons is physically explained by the fact that at $\tau \ll E_0^{-1}$ the atom can "feel" nonstationarity only after the cavity has become stationary and the photon out-states have been formed. However, beyond the framework of this model, basically new effects arise.

The model ceases to be exactly integrable after inclusion of the terms $\lambda(\sigma_- a + \sigma_+ a^\dagger)$ in Hamiltonian (1), so that the analysis of the nonresonance effects can only be carried out if the coupling constant λ is considered as a perturbation. At $\omega = $ const, the stationary states of the system are dressed in the first order, while the shift of the corresponding energy levels appears in the second order in λ. It is essential that, contrary to the Janes–Cummings model, the ground state $|0, \downarrow\rangle_{\lambda\omega}$ in the presence of nonresonance interaction is also dressed and acquires the Lamb shift $\delta E_L = -\lambda^2/(\omega + E_0)$.

The calculation of the probability of atomic excitation in the sudden approximation is performed along the same lines as in the preceding case. In doing so, the

amplitude $A_{n\uparrow}$ of atomic excitation and creation of n photons can be conveniently divided into two parts:

$$A_{n\uparrow} = A_{n\uparrow}^{(L)} + A_{n\uparrow}^{(C)}, \quad A_{n\uparrow}^{(L)} = {}_{\lambda\omega_2}\langle n, \uparrow | 0, \downarrow \rangle_{\lambda\omega_1},$$

$$A_{n\uparrow}^{(C)} = {}_{\lambda\omega_2}\langle n, \uparrow | (e^{-iW} - 1) | 0, \downarrow \rangle_{\lambda\omega_1}.$$

Clearly, the nonresonance effects contribute to both terms in the excitation amplitude. However, whereas the contribution to the second term can be regarded as a correction, the first term is fully determined by the nonresonance effects and, for this reason, is absent in the Janes–Cummings model. This is formally explained by the fact that the $|0, \downarrow\rangle$ state is the exact dressed state for any frequency of the photon mode and hence is orthogonal in the resonance approximation to all excited states. Moreover, the $A_{n\uparrow}^{(C)}$ term is determined by the NCE-induced change $(e^{-iW} - 1) | 0, \downarrow \rangle_{\lambda\omega_1}$ of the ground state of the system and disappears if the Casimir term proportional to $\dot\omega$ is omitted in Hamiltonian (1), which is formally equivalent to replacing the operator of sudden perturbation W by zero. At the same time, this procedure does not affect the $A_{n\uparrow}^{(L)}$ term. Hence it follows that this term is responsible for a new physical effect, viz., the dynamic Lamb shift analogous to Migdal's shake-up effect and having no relevance to the NCE. Of course, the probability of atomic excitation includes the contributions both from this effect and the NCE separately and from the interference of these effects.

In the leading order of perturbation theory, the contribution of the shake-up effect to the excitation probability is

$$w_{\uparrow}^{(L)} = \sum_{n=0}^{\infty} \left| A_{n\uparrow}^{(L)} \right|^2$$

$$= \lambda^2 \left(\frac{1}{\omega_2 + E_0} - \frac{1}{\omega_1 + E_0} \right)^2 = \left(\frac{\delta E_L}{\lambda} \right)^2, \quad (6)$$

where δE_L is the change in the atomic ground-state Lamb shift. One can see from Eq. (6) that the excitation due to the shake-up effect is accompanied by the creation of one photon (or more, but necessarily an odd number of photons, in the higher orders of perturbation theory) as a result of the modulation of the ground-state Lamb shift. Note that the quadratic dependence of the excitation probability on a (small) change in the Lamb shift is specific not only to the simple model considered but is also inherent in the realistic three-dimensional problem of a real atom confined in a nonstationary cavity. This is due to the fact that, upon a small change in any parameter of the cavity, the Lamb shift will change in proportion to the first power of this parameter. In this case, the overlap amplitude between the new and previous stationary states will also be proportional to the first power of this parameter, while the excitation probabil-

ity is determined by the amplitude squared. As for our model, these speculations allow reproduction of Eq. (6), at least to a constant factor. Indeed, in the first order of perturbation theory, the excitation probability $w_{\uparrow}^{(L)}$ is proportional to the coupling constant λ squared. Considering that $w_{\uparrow}^{(L)} \sim \delta E_L^2$, while the Lamb shift $\delta E_L \sim \lambda^2$, one immediately obtains $w_{\uparrow}^{(L)} \sim (\delta E_L/\lambda)^2$, in accordance with Eq. (6). These arguments also explain why the non-Casimir excitation channel is absent in the Janes–Cummings model, where the ground-state Lamb shift is absent.

To reveal how the finite time of nonstationarity τ influences the excitation probability, let us turn again to the generalized Janes–Cummings model. Using the standard time-dependent perturbation theory, one can show that the probability of atomic excitation, to first order, is equal to

$$w_{\uparrow} = \frac{\lambda^2}{\Delta_2^2} |\beta_\infty(\tau)|^2 F(\tau),$$

$$F(\tau) = \left| \int_{-\infty}^{\infty} dt' e^{i\Delta_2 t'} \frac{d}{dt'} \left[\frac{\beta(t')}{\beta_\infty} e^{i\omega_2 t'} \right] \right|^2, \quad (7)$$

where the dimensionless function $F(\tau)$ characterizes the relative efficiency of atomic excitation during the cavity nonstationarity time τ, as compared to excitation through the absorption of $\overline{N}_{NCE} = |\beta_\infty|^2$ photons. Insofar as $F(0) = 1$, Eqs. (4) and (7) are consistent with each other.

Physically, $F \approx 1$ corresponds to atomic excitation predominantly through the absorption of Casimir photons, while the F values well above unity correspond to excitation in a time $\leq \tau$ during the transient process, when the final photon states have not yet formed. Numerical analysis shows that the function $F(\tau)$ monotonically increases with τ, so that the estimate $F(\tau) > 1$ holds for $\tau > 0$. Moreover, for certain values of the parameters, the excitation efficiency F may be as high as several tens or even hundreds at $\tau \sim E_0^{-1}$. As a result, the excitation probability at $\tau \sim E_0^{-1}$ may be appreciably higher than in the sudden limit $\tau = 0$, despite the fast decrease in the number of created photons, which suppresses the $F(\tau)$ growth for very small and large τ.

The second-order effects in coupling constant λ also influence the number of photons created in the cavity, thereby evidencing the back action of an atom in the cavity on the NCE. Since the number of photons created due to the fast Lamb-shift modulation in the weak coupling limit is on the order of $(\delta E_L/\lambda)^2$ and hence far smaller than unity, we turn our attention to the stronger finite-time effects and analyze them within the frame-

work of the generalized Janes–Cummings model. As is known, the operator

$$N = a^\dagger a + \frac{1}{2}(1 + \sigma_3)$$

is the integral of motion in the standard Janes–Cummings model [3]. For the nonstationary cavity, it depends on time; one can show by the standard methods that, to first order in the coupling constant λ, the average value $\overline{N}(\infty) = {}_\infty\langle 0, \downarrow|N|0, \downarrow\rangle_\infty$ is equal to

$$\overline{N}_\infty = \overline{N}(+\infty) = |\beta_\infty|^2 + o(\lambda) = \overline{N} + o(\lambda). \qquad (8)$$

At the same time, using equality $\overline{N}_\infty = \bar{n} + w_\uparrow$, where $\bar{n} = \langle a^\dagger a\rangle$ is the average number of photons, one finds that the average number of photons created in the presence of an atom is determined by Eq. (5), i.e., at first glance, by the number of photons created in the absence of the atom minus the average number of absorbed photons (provided that the atom absorbs a photon with probability $w_\uparrow$). In reality, as was already shown, the atomic excitation at $\tau \neq 0$ is generally not the mere absorption of a photon, and, hence, the probability $w_\uparrow$ does not coincide with the probability of photon absorption.

Furthermore, the second-order perturbation theory gives a correction to Eq. (8). An important fact is that the corresponding correction $\delta\overline{N}_\infty$ to the right-hand side of Eq. (5) is of the same order in λ as the $w_\uparrow$ term, so that both are comparable in magnitude. This implies that the correction to the average number of created photons in the leading order of perturbation theory differs from the average number of absorbed photons taken with the minus sign or, in other words, that the influence of an atom on the NCE extends further than the mere atomic absorption of photons, even if one disregards the shake-up effect.

To focus only on that part of the effect which is associated with the correction $\delta\overline{N}$, we write

$$\overline{N}_\infty = \overline{N}\left(1 + \frac{\lambda^2}{E_0^2}\eta(\tau)\right). \qquad (9)$$

The dimensionless parameter $\eta(\tau)$ characterizes the level of back action of an atom on the NCE. This action was studied by numerical methods. It turns out that the $\eta(\tau)$ function is quadratic at $\tau \sim E_0^{-1}$ and linear at $\tau \gg E_0^{-1}$. This effect will be discussed elsewhere in more detail.

Note in conclusion that the effects considered in this work can be experimentally implemented, e.g., by passing an atomic beam though a microcavity whose optical walls change rapidly upon illumination by ultrashort laser pulses. The situation where the characteristic time of changing the optical properties of the cavity walls coincides, in order of magnitude, with the characteristic time of atomic transition can easily be attained (the quasi-static case was considered in [5]).

REFERENCES

1. V. V. Dodonov, Phys. Lett. A **207**, 126 (1995).
2. E. T. Janes, Microwave Laboratory Report No. 502 (Standford Univ., 1958).
3. E. T. Janes and F. W. Cummings, Proc. IEEE **51**, 89 (1963).
4. C. K. Law, Phys. Rev. Lett. **73**, 1931 (1994).
5. Yu. E. Lozovik, in *Proceedings of the 1st Soviet-British Symposium on Ion Spectroscopy, Troitsk, 1986*; J. Phys. B **22**, L101 (1989).

Translated by V. Sakun

Self-Consistent Equations for the Interaction of an Atom with an Electromagnetic Field of Arbitrary Intensity

A. V. Andreev

International Laser Center, Faculty of Physics, Moscow State University, Vorob'evy gory, Moscow, 119899 Russia
Received June 20, 2000; in final form, July 28, 2000

A system of equations is suggested for the interaction of an atom with an electromagnetic field of arbitrary intensity. The distinctive feature of the equations is that, in the absence of the field, the electron density in the atom is determined by the Schrödinger equation and, in the presence of the field, by the equation resembling the classical equation for an electron in the Lorentz force field. © *2000 MAIK "Nauka/Interperiodica".*

PACS numbers: 32.80.–t

1. Recent investigations into atomic and molecular interactions with ultrastrong laser fields have shown [1–5] that standard perturbative approaches, although adequate in describing the atomic interactions with moderately strong fields, become inapplicable if the intensity of the external field is comparable with the intensity of the intraatomic field. The approaches based on the two- or any-finite-level atomic models also lose their generality. The fundamental cause is that the ratio of the interaction Hamiltonian to the Hamiltonian H_0 of a free atom ceases to be a small parameter [6]. The classical approach based on the use of equations for a point-like electron subjected simultaneously to the external and intraatomic fields is an alternative to the quantum-mechanical approach. One may anticipate that this approach applies when the atom is ionized or the electron is in a highly excited state. However, it is clear that one should not count on quantitative agreement when using this approach for the calculation of atomic ionization rates or atomic response to moderately strong fields.

In this work, an attempt is undertaken to join the simplicity of the classical approach and the accuracy of the quantum-mechanical approach in the description of atomic interaction with an external field. A closed system of self-consistent equations is derived for the atomic charge densities and transitional currents. It is shown that in limiting cases the equations coincide with the Schrödinger equation or with the equation of a classical electron in the Lorentz force field.

2. Analysis of the interaction of a nonrelativistic atom with an external electromagnetic field can be carried out on the basis of a joint solution of the equations for the vector $\mathbf{A}(\mathbf{r}, t)$ and scalar $\varphi(\mathbf{r}, t)$ field potentials and the Schrödinger equation for the atomic wave function $\psi(\mathbf{r}, t)$:

$$\Delta\mathbf{A} - \frac{1}{c^2}\frac{\partial^2\mathbf{A}}{\partial t^2} = -\frac{4\pi}{c^2}\mathbf{J}(\mathbf{r}, t) + \frac{1}{c}\nabla\frac{\partial\varphi}{\partial t}, \tag{1a}$$

$$\Delta\varphi(\mathbf{r}, t) = -4\pi(\rho(\mathbf{r}, t) + \rho_z(\mathbf{r}, t)), \tag{1b}$$

$$i\hbar\frac{\partial\psi}{\partial t} = H\psi, \tag{1c}$$

where $\rho(\mathbf{r}, t) = e\psi^+(\mathbf{r}, t)\psi(\mathbf{r}, t)$ is the electron charge density and $\rho_z(\mathbf{r}, t)$ is the nuclear charge density. In Eqs. (1), the Coulomb gauge is used for the field,

$$\operatorname{div}\mathbf{A} = 0, \tag{2}$$

and the generalized transitional current density $\mathbf{J}(\mathbf{r}, t)$ is introduced. It is related to the quantum-mechanical electron current density

$$\mathbf{j}(\mathbf{r}, t) = \frac{i\hbar e}{2m}(\nabla\psi^+(\mathbf{r}, t)\psi(\mathbf{r}, t) - \psi^+(\mathbf{r}, t)\nabla\psi(\mathbf{r}, t)) \tag{3}$$

by the expression

$$\mathbf{J}(\mathbf{r}, t) = \mathbf{j}(\mathbf{r}, t) - \frac{e}{mc}\mathbf{A}(\mathbf{r}, t)\rho(\mathbf{r}, t). \tag{4}$$

The Hamiltonian of an atom in an external field has the well-known form

$$H = \frac{1}{2m}\left(\mathbf{p} - \frac{e}{c}\mathbf{A}\right)^2 + e\varphi. \tag{5}$$

A standard approach to the analysis of atomic interaction with a field amounts to solving the Schrödinger equation for an isolated atom $H_0 = H(\mathbf{A} = 0)$, with the object of determining the eigenfunctions of an unperturbed atom, followed by the calculation of the population probability amplitudes for different atomic levels in the presence of an external field. However, if the external field strength is comparable with that of the intraatomic field, the wave function becomes so heavily distorted that decomposition into the unperturbed wave functions includes a wealth of terms, whose number tends to infinity as the field increases. This renders the use of the indicated classical procedure highly inconve-

nient for the analysis of the atomic interactions with ultrastrong laser fields.

One can see from Eqs. (1a) and (1b) that only the generalized current density $\mathbf{J}(\mathbf{r}, t)$ and the charge density $\rho(\mathbf{r}, t)$ need to be known for calculation of the atomic response. These quantities can be determined from the solution of Schrödinger equation (1c). However, the respective solution for an arbitrary atom subjected to an external field involves well-known problems. For this reason, an approach based on the analysis of a closed system of equations including only the above-mentioned atomic variables and the field potentials seems to be more rational. Such an approach would allow one to develop various iterative procedures for calculating the atomic response to a field of arbitrary strength.

3. Using Schrödinger equation (1c) with Hamiltonian (5), it is straightforward to obtain the following equations for the charge density and the generalized current density:

$$\partial\rho/\partial t + \operatorname{div}\mathbf{J} = 0, \tag{6a}$$

$$\frac{\partial J_a}{\partial t} = \frac{e}{m}\left(\left(-\frac{1}{c}\frac{\partial A_\alpha}{\partial t} - \nabla_\alpha\varphi\right)\rho + \frac{1}{c}[\mathbf{J}\times\operatorname{curl}\mathbf{A}]_\alpha\right)$$

$$+ \frac{e}{mc}\nabla_\beta\left(A_\alpha J_\beta + A_\beta J_\alpha + \frac{e}{mc}A_\alpha A_{\beta\rho}\right) \tag{6b}$$

$$+ \frac{\hbar^2}{4m^2}\nabla_\alpha(\Delta\rho) - \frac{e\hbar^2}{2m^2}\nabla_\beta(\nabla_\alpha\psi^+\nabla_\beta\psi + \nabla_\beta\psi^+\nabla_\alpha\psi).$$

One can see that Eq. (6a) is a continuity equation and the first term on the right-hand side of Eq. (6b) has a simple classical analogy, because it formally coincides with the classical Lorentz force. The last three terms in this equation are unusual. It is also clear that system of equations (6) is not closed, because Eq. (6b) incorporates the new variable $q_{\alpha\beta} = \nabla_\alpha\psi^+\nabla_\beta\psi + \nabla_\beta\psi^+\nabla_\alpha\psi$ containing products of the wave-function derivatives.

Let us show that this variable can be expressed through the known quantities. This can be done with the use of the equalities

$$\nabla_\alpha(\psi^+\psi)\nabla_\beta(\psi^+\psi) = \nabla_\alpha\psi^+\nabla_\beta\psi^+\psi\psi$$

$$+ \psi^+\psi^+\nabla_\alpha\psi\nabla_\beta\psi + \psi^+\psi(\nabla_\alpha\psi^+\nabla_\beta\psi + \nabla_\beta\psi^+\nabla_\alpha\psi),$$

$$(\nabla_\alpha\psi^+\psi - \psi^+\nabla_\alpha\psi)(\nabla_\beta\psi^+\psi - \psi^+\nabla_\beta\psi)$$

$$= \nabla_\alpha\psi^+\nabla_\beta\psi^+\psi\psi + \psi^+\psi^+\nabla_\alpha\psi\nabla_\beta\psi$$

$$- \psi^+\psi(\nabla_\alpha\psi^+\nabla_\beta\psi + \nabla_\beta\psi^+\nabla_\alpha\psi).$$

Hence, one gets

$$eq_{\alpha\beta} = \frac{\nabla_\alpha\rho\nabla_\beta\rho}{2\rho} + \frac{2m^2}{\hbar^2}\frac{j_\alpha j_\beta}{\rho}. \tag{7}$$

Substituting Eq. (7) into Eq. (6b), one finally arrives at

$$\frac{\partial J_\alpha}{\partial t} = \frac{e}{m}\left(\mathbf{E}\rho + \frac{1}{c}[\mathbf{J}\times\mathbf{H}]_\alpha\right)$$

$$- \frac{\rho}{m}\nabla_\alpha\left(e\varphi - \frac{\hbar^2}{4m}\left(\nabla\left(\frac{\nabla\rho}{\rho}\right) + \frac{1}{2}\left(\frac{\nabla\rho}{\rho}\right)^2\right)\right) - \nabla_\beta\left(\frac{J_\alpha J_\beta}{\rho}\right), \tag{8}$$

where $\mathbf{E} = -(1/c)(\partial\mathbf{A}/\partial t)$ is the strength of the transverse component of the electric field and $\mathbf{H} = \operatorname{curl}\mathbf{A}$.

Therefore, Eqs. (1a), (1b), (6a), and (8) form a closed system of equations for the variables $\mathbf{A}(\mathbf{r}, t)$, $\varphi(\mathbf{r}, t)$, $\mathbf{J}(\mathbf{r}, t)$, and $\rho(\mathbf{r}, t)$.

4. Note that, in the formalism of secondary quantization of the Schrödinger equation, the last two terms on the right-hand side of Eq. (6b) stem from the commutator $[\mathbf{j}, H_0]$ of the current density operator $\mathbf{j}$ and the intraatomic Hamiltonian H_0, while the second term is due to the nonpointlike character of the electron. To simplify the comparison with the classical equation for a pointlike electron, it is convenient to introduce the local electron current

$$\mathbf{V}(\mathbf{r}, t) = \mathbf{J}(\mathbf{r}, t)/\rho(\mathbf{r}, t). \tag{9}$$

Inserting Eq. (9) into Eq. (8), one obtains

$$\frac{1}{\rho}\left(\frac{\partial\rho}{\partial t} + \mathbf{v}\nabla\rho\right) = -\operatorname{div}\mathbf{V}, \tag{10a}$$

$$\frac{\partial\mathbf{V}}{\partial t} + (\mathbf{V}\nabla)\mathbf{V} = \frac{e}{m}\left(\mathbf{E} + \frac{1}{c}[\mathbf{V}\times\mathbf{H}]\right)$$

$$- \frac{1}{m}\nabla\left[e\varphi - \frac{\hbar^2}{4m}\left(\nabla\left(\frac{\nabla\rho}{\rho}\right) + \frac{1}{2}\left(\frac{\nabla\rho}{\rho}\right)^2\right)\right]. \tag{10b}$$

System of equations (10) has the form of a system of equations of plasma hydrodynamics and differs from it only by the presence of terms depending on the charge density on the right-hand side of Eq. (10b).

5. To elucidate the meaning of the additional terms on the right-hand side of Eq. (10b), let us solve Eqs. (10) in the stationary case

$$\partial\rho/\partial t = 0, \quad \mathbf{V} = 0. \tag{11}$$

Eqs. (11) are fulfilled if

$$e\varphi - \frac{\hbar^2}{4m}\left(\nabla\left(\frac{\nabla\rho}{\rho}\right) + \frac{1}{2}\left(\frac{\nabla\rho}{\rho}\right)^2\right) = C, \tag{12}$$

where C is a constant. Let us introduce the following notations: $\rho = en$ and $n = f^2$. Then Eq. (12) can be recast in the form

$$\left(-\frac{\hbar}{2m}\Delta + e\varphi(\mathbf{r})\right)f(\mathbf{r}) = Ef(\mathbf{r}), \tag{13}$$

where the C constant is denoted by E to achieve analogy with the Schrödinger equation.

Therefore, one can see that in the stationary case the charge density in an atom is determined by the Schrödinger equation for a real wave function $f(\mathbf{r})$. This is not surprising, because one has for the wave-function representation $\psi(\mathbf{r}, t) = f(\mathbf{r}, t)\exp[i\Phi(\mathbf{r}, t)]$: $\rho = ef^2$ and $\mathbf{v} = \mathbf{j}/\rho = (\hbar/m)\boldsymbol{\nabla}\Phi$.

6. Thus, the stationary charge distribution in an atom obeys the Schrödinger equation. Now let the initial atomic state be different from stationary and the external field be absent. Let us determine the dynamics of the charge density and current in an atom. Introducing substantive derivative $d/dt = \partial/\partial t + (\mathbf{V}\boldsymbol{\nabla})$, one can rewrite Eqs. (10) as

$$\frac{d}{dt}\left(\frac{1}{\rho}\frac{d\rho}{dt}\right)$$
$$-\frac{1}{m}\Delta\left[e\varphi - \frac{\hbar^2}{4m}\left(\boldsymbol{\nabla}\left(\frac{\boldsymbol{\nabla}\rho}{\rho}\right) + \frac{1}{2}\left(\frac{\boldsymbol{\nabla}\rho}{\rho}\right)^2\right)\right] = 0. \tag{14}$$

The charge density and the generalized current density can be represented in the following general form:

$$\rho(\mathbf{r}, t) = \rho_0(\mathbf{r}) - \mathrm{div}\mathbf{P}(\mathbf{r}, t),$$

$$\mathbf{J}(\mathbf{r}, t) = \frac{\partial \mathbf{P}}{\partial t} + \mathrm{curl}\mathbf{M}(\mathbf{r}, t),$$

where $\mathbf{P}$ and $\mathbf{M}$ are the polarization and magnetization vectors, respectively. The density $\rho_0(\mathbf{r})$ is caused by inner-shell electrons tightly coupled to the nucleus, and the $\rho(\mathbf{r}, t) - \rho_0(\mathbf{r})$ part is due to the outer-shell atomic electrons. Accordingly, the electron density can be represented in the form

$$n(\mathbf{r}, t) = n_0(\mathbf{r}) + n_1(\mathbf{r}, t) = n_0(\mathbf{r})\exp(\eta(\mathbf{r}, t)). \tag{15}$$

Substituting Eq. (15) into Eq. (14) and taking into account that

$$\frac{\hbar^2}{2m}\frac{\Delta\sqrt{n_0}}{\sqrt{n_0}} = -E + e\varphi_0(\mathbf{r}),$$

one obtains

$$\frac{d^2\eta}{dt^2} + \frac{4\pi e^2 n_0}{m}(\exp(\eta) - 1)$$
$$+ \frac{\hbar^2}{4m^2}\Delta\left(\frac{\boldsymbol{\nabla} n_0}{n_0}\boldsymbol{\nabla}\eta + \Delta\eta + \frac{(\boldsymbol{\nabla}\eta)^2}{2}\right) = 0. \tag{16}$$

Therefore, for $\eta(\mathbf{r}, t) = \eta(t)$ and $|\eta| \ll 1$ one has

$$\frac{d^2\eta}{dt^2} + \frac{4\pi e^2 n_0}{m}\eta = 0. \tag{17}$$

Hence, a weakly perturbed electron density oscillates with plasma frequency

$$\omega_p = \sqrt{\frac{4\pi e^2 n_0(r_0)}{m}},$$

where r_0 is the radius of the inner electronic shells. In the general case where η is not small and depends on the coordinate, the terms depending on the η gradient in Eq. (16) play a role analogous to the viscous terms in the equations of hydrodynamics.

7. In conclusion, Eqs. (8) and (10) combine the classical and quantum descriptions of electron motion in the self-consistent field of the intraatomic potential and the field of an external wave. The calculations have shown that the stationary electron density in an atom is determined from the solution of the Schrödinger equation, while the weak perturbations of the electron density oscillate with a plasma frequency depending on the density for a given equipotential. Because of an increase in the electron density near the atomic center, the motion of inner-shell electrons is screened from long-wavelength (e.g., optical) radiation but can be perturbed by X-ray radiation. The qualitative distinction of the suggested equations from the fundamental equations of classical and quantum mechanics is that they are nonlinear. The nonlinearity arises because of the elimination of the second derivatives from the bilinear combinations of wave functions [the term $q_{\alpha\beta}$ in Eq. (6b)]. In principle, system of equations (6) can be continued ad infinitum by introducing terms with higher order derivatives while retaining the linearity in atomic variables ρ, j_α, $q_{\alpha\beta}$, … . Consequently, it seems likely that the effects of nonlocal atomic response are mainly responsible for the nonlinearity.

REFERENCES

1. N. B. Delone and V. P. Krainov, *Multiphoton Process in Atoms* (Springer-Verlag, Berlin, 1994).

2. M. V. Fedorov, *Atomic and Free Electrons in a Strong Light Field* (World Scientific, Singapore, 1997).

3. V. T. Platonenko and V. V. Strelkov, Kvantovaya Élektron. (Moscow) **25**, 586 (1998).

4. A. V. Kim, M. Yu. Ryabikin, and A. M. Sergeev, Usp. Fiz. Nauk **169**, 58 (1999).

5. M. V. Fedorov, Usp. Fiz. Nauk **169**, 66 (1999).

6. A. V. Andreev, Zh. Éksp. Teor. Fiz. **116**, 793 (1999) [JETP **89**, 421 (1999)].

Translated by V. Sakun

New Regime of Anomalous Penetration of Relativistically Strong Laser Radiation into an Overdense Plasma[1]

A. Kim*, F. Cattani**, D. Anderson**, and M. Lisak**

* Institute of Applied Physics, Russian Academy of Sciences, ul. Ul'yanova 46, Nizhni Novgorod, 603600 Russia
** Department of Electromagnetics, Chalmers University of Technology, S-412 96 Göteborg, Sweden
Received March 20, 2000; in final form, July 13, 2000

It is shown that penetration of relativistically intense laser light into an overdense plasma, accessible by self-induced transparency, occurs over a finite length only. The penetration length depends crucially on the overdense plasma parameter and increases with increasing incident intensity after exceeding the threshold for self-induced transparency. Exact analytical solutions describing the plasma-field distributions are presented. © 2000 MAIK "Nauka/Interperiodica".

PACS numbers: 52.40.Nk; 52.35.Mw; 52.60.+h

In the past few years, there has been much research devoted to the nonlinear interaction of superintense laser pulses with plasmas [1]. At intensities where electrons quiver with relativistic velocities, the interaction can be characterized as nonlinear optics in relativistic plasmas and new regimes, not evident at nonrelativistic intensities, may appear. As was previously shown, superintense electromagnetic radiation can propagate through a classically overdense plasma due to the relativistic correction to the electron mass, the so-called induced transparency effect, [2–10]. This work has resulted in the identification of a new fundamental process in the relativistic laser overdense plasma interaction.

In order to understand the nonlinear regime of the interaction of superintense laser light with an overdense plasma, it is enough, without loss of generality, to consider a stationary model. We present here a new class of exact analytical solutions describing the penetration of an electromagnetic wave normally incident onto a cold, overdense plasma with a sharp boundary. In particular, we show that, when the incident intensity exceeds the threshold for self-induced transparency, the laser energy penetrates into the dense plasma without any losses, but over a finite length only. At the same time, the electron density distribution becomes structured as a sequence of electron layers separated by depleted regions about half a wavelength wide, so that this strongly nonlinear plasma structure acts as a distributed Bragg reflector.

The ultrahigh intensity laser–plasma interaction is described by the relativistic equation of motion and the equation of continuity for the electrons, together with Maxwell's equations. Ions are treated as a uniform neutralizing background. We will consider circularly polarized laser radiation with normalized amplitude of the

vector potential $e\mathbf{A}/mc^2 = (a/\sqrt{2})\mathrm{Re}[(\mathbf{y} + i\mathbf{z})\exp(i\omega t)]$ normally incident from vacuum ($x < 0$) onto a semi-infinite plasma ($x \geq 0$). Assuming a stationary regime, the basic equations may be written in the form

$$\phi'' = n_o(n - 1), \qquad (1)$$

$$a'' + \left(1 - \frac{n_o}{\gamma}n\right)a = 0, \qquad (2)$$

$$\phi' = \gamma' \text{ if and only if } n(x) \neq 0 \qquad (3)$$

(where the variables are normalized as $x \longrightarrow \omega x/c$, $n \longrightarrow n/n_o$, $n_o = \omega_p^2/\omega^2$; ω is the carrier frequency of the laser radiation; ω_p is the plasma frequency of the initial unperturbed plasma; $\gamma = (1 + a^2)^{1/2}$ is the relativistic factor; and n and ϕ are the normalized electron density and scalar potential of the plasma, respectively). Equation (3) indicates that only in the region where the electron density $n(x) \neq 0$ must the ponderomotive force $\gamma'(x)$ be compensated by the force of a longitudinal field. This statement will be important for constructing solutions of interest in the present analysis.

For homogeneous ion density, the system has the following Hamiltonian:

$$\mathscr{H}_E = \frac{1}{2(1 + a^2)}a'^2 - \frac{1}{2}(2n_o\sqrt{1 + a^2} - a^2), \qquad (4)$$

which was analyzed in [5].

As we are interested in a semi-infinite plasma, we first consider the case when $n(x) \longrightarrow 1$ and both $a(x)$ and $a'(x)$ vanish as $x \longrightarrow \infty$. In this case, the integral of motion equals

$$\mathscr{H}_E = -n_o \equiv \mathscr{H}_0. \qquad (5)$$

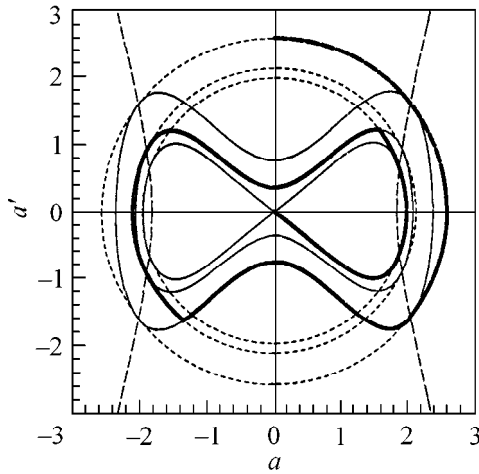[1] This article was submitted by the authors in English.

Fig. 1. Phase portrait of the system for $n_o = 1.6$ and homogeneous ion density, according to Eqs. (4) and (8); see also Fig. 2. The dashed lines stand for vacuum regions; the continuous lines stand for plasma regions; the actual trajectory is given by the thick line, and it runs clockwise. The large dashed line denotes the regions where the electron density is negative.

Equation (4) can then be easily integrated to yield the following single-parameter solitary solution:

$$a(x) = \frac{A_m \cosh[|\varepsilon_0|^{1/2}(x - x^{(0)})]}{n_o \cosh^2[|\varepsilon_0|^{1/2}(x - x^{(0)})] - |\varepsilon_0|}, \qquad (6)$$

where $\varepsilon_0 = 1 - n_o$ is the dielectric permittivity of the plasma and the parameter $x^{(0)}$ defines the position of the maximum of function (6), which is given by $A_m = 2[n_o(n_o - 1)]^{1/2}$.

For $n_o > 1.5$, this solution contains a region where the electron density is negative, which is clearly unphysical. Requiring the minimum electron density $n_m = 1 - 4(n_o - 1)^2$ to be positive, i.e., $n_m \geq 0$, we obtain a condition on the background plasma density and an argument in favor of the depletion region: for $n_o > 1.5$, we have to take into account only that part of the solution where the corresponding electron density is positive, $n(x) \geq 0$. By using the part of solution (6) corresponding to a ponderomotive force that pushes electrons into the plasma and matching it to the vacuum solution, an exact expression for the intensity threshold of self-induced transparency was found [11]. It should be noted that Hamiltonian (5) corresponds to a zero energy flux, but there are solutions with nonzero flux as well [2, 6]. They can arise even in correspondence with incident amplitudes smaller than the penetration threshold. However, for the realization of such nonlinear hysteresis-like solutions [10,12], preliminary modifications of the plasma must be induced by extremely intense fields. For the description of the steady-state of

a problem involving laser radiation with a turn-on shape, it is natural to choose the zero-flux approach.

The left side of function (6) gives rise to an unbalanced ponderomotive force pulling electrons out of the plasma towards the incident wave, and, at first glance, it seems that the charge quasineutrality condition cannot be satisfied. However, after a length of about half a wavelength, these electrons will be stopped by the ponderomotive force acting in the opposite direction. Thus, in the general case, we may expect that the full plasma field structure will consist of a sequence of alternating depletion and nondepletion regions.

This can be understood from Fig. 1, where the phase portraits described by Eqs. (1)–(3) and by the corresponding equation for the depletion (vacuum) region are presented. For a half-space plasma, the limiting case corresponds to motion with an infinite period along the separatrix determined by Eq. (5), i.e., an exponentially decreasing field inside the overdense plasma. Going backwards toward the initial vacuum–plasma boundary, before the last semi-infinite electron layer, there must exist a depletion region. Here, the amplitude of the field corresponds to a forward-going wave along the incident direction, with an intensity below the threshold value (corresponding to the motion along the first circular trajectory in phase space, coming from the vacuum Hamiltonian). Then, in front of this layer, we have to put another electron layer, where the solution for the field $a(x)$ follows from Hamiltonian (4) with a magnitude $\mathcal{H} > -n_o$ (corresponding to an oscillatory motion about zero). This construction is repeated until the initial plasma boundary is reached. At the boundary between each depletion and nondepletion region, the solution for the field must satisfy continuity conditions for both a and its derivative a'. It is also clear that there exists a family of stationary solutions that differ from each other by the number of electron density layers and their shapes. When the incident amplitude is increased, the number of layers will increase as well, as follows from the phase portraits in Fig. 1.

In order to quantify the above discussion, we present a more rigorous analytical description. Starting at the inside of the plasma region, the solution for the field is an exponentially decreasing function of the spatial coordinate, in fact, a part of the localized solution given by Eq. (6) with $\mathcal{H}_E = \mathcal{H}_0$ for $x_0 \leq x < \infty$. The point $x = x_0$ can be determined self-consistently from the global solution and the boundary conditions

$$a(x = x_0) = a_0, \quad a'(x = x_0) = a'_0. \qquad (7)$$

The next region ($x_1 < x < x_0$) must be a depletion layer where $n(x) = 0$. The second boundary position of this depletion layer, x_1, must also be determined self-

consistently. The Hamiltonian here is the vacuum one and reads

$$\mathcal{H}_V = \frac{1}{2}(a'^2 + a^2) = \frac{1}{2}(a_0'^2 + a_0^2) \equiv \mathcal{H}_1, \qquad (8)$$

where we have taken into account the boundary conditions for the field and its first derivative. The solution of the field in this depletion region reads

$$a(x) = A_1\cos(x + \psi_1). \qquad (9)$$

Using Eq. (7), we have $A_1 = (a_0'^2 + a_0^2)^{1/2} = (2\mathcal{H}_1)^{1/2}$, $\psi_1 = -\arctan(a_0'/a_0) - x_0$. The boundary position x_1 can be calculated by integrating Poisson's equation in the interval $x_1 < x < x_0$:

$$\phi'(x_0) - \phi'(x_1) = -n_o(x_0 - x_1), \qquad (10)$$

which, together with relation (3), leads to a transcendental equation for $\xi = x_0 - x_1$:

$$\xi = g(\xi) - g(0), \qquad (11)$$

where

$$g(\xi) = \frac{A_1^2\sin[2(\xi + \xi_1)]}{2n_o[1 + A_1^2\cos^2(\xi + \xi_1)]^{1/2}}, \qquad (12)$$

$$\xi_1 = \arctan\left(\frac{a_0'}{a_0}\right).$$

Since the left-hand side of Eq. (11) is a linear function, while its right-hand side is a periodic function of ξ, this equation has a nontrivial solution only if $g'(\xi = -\xi_1) > 1$; i.e.,

$$g'(\xi = -\xi_1) = \frac{A_1^2}{n_o(1 + A_1^2)^{1/2}} > 1. \qquad (13)$$

However, if $n_o \leq 1.5$, this condition is never satisfied, because its maximum value reaches unity at $n_o = 1.5$. Consequently, for plasma densities $n_o < 1.5$, we conclude that there are no stationary regimes of anomalous penetration: there can only exist dynamical solutions. For $n_o > 1.5$, Eq. (11) always has nontrivial solutions, which can be found numerically. Formally, Eq. (11) admits several roots but we have to consider only those corresponding to a positive electron density.

Having solved Eq. (11), we know $a_1 = a(x_1)$ and $a_1' = a'(x_1)$. The next region must again be an electron layer. Denoting this region as $x_2 \leq x \leq x_1$, Hamiltonian (4) will be

$$\mathcal{H}_E = \mathcal{H}_E(a_1, a_1') \equiv \mathcal{H}_2, \qquad (14)$$

with the corresponding field solution written in terms of two-parameter elliptic functions for the field strength as

$$a(x) = \begin{cases} \dfrac{2q\,\mathrm{cn}[\varepsilon_2^{1/2}(x - x^{(2)})]}{2 + [(q^2 + 1)^{1/2} - 1]\mathrm{sn}^2[\varepsilon_2^{1/2}(x - x^{(2)})]}, \\ \quad \mathcal{H}_2 < n_o, \\[1.5em] \dfrac{2\bar{q}\,\mathrm{sn}[((\varepsilon_2 + 1)^2 - n_o^2)^{1/2}(x - x^{(2)})/2]}{\bar{q}^2 - \mathrm{sn}^2[((\varepsilon_2 + 1)^2 - n_o^2)^{1/2}(x - x^{(2)})/2]}, \\ \quad \mathcal{H}_2 > n_o. \end{cases} \qquad (15)$$

Two parameters ε_2 and $x^{(2)}$ are determined by the boundary conditions at $x = x_1$. Here, $\varepsilon_2 = (n_o^2 + 1 + 2\mathcal{H}_2)^{1/2}$, $q = [(\varepsilon_2 + n_o)^2 - 1]^{1/2}$ and $\bar{q} = [(\varepsilon_2 + n_o + 1)/(\varepsilon_2 + n_o - 1)]^{1/2}$, $k = [(n_o^2 - (\varepsilon_2 - 1)^2)/4\varepsilon_2]^{1/2}$ and $\bar{k} = [((\varepsilon_2 - 1)^2 - n_o^2)/((\varepsilon_2 + 1)^2 - n_o^2)]^{1/2}$ are the moduli of the elliptic integrals of the first kind, respectively, for the two cases. This solution is realized over about a quarter of a period, where the electron density is positive and is given by

$$n(x) = \frac{2\sqrt{1 + a^2}}{n_o}\left(\mathcal{H}_2 + \frac{3}{2}n_o\sqrt{1 + a^2} - a^2\right). \qquad (16)$$

The second boundary position of this layer can now be defined with a certain arbitrariness; namely, it can be taken within the whole interval $x^* \leq x_2 \leq x^{**}$; where x^* is such that $n(x^*) = 0$, while x^{**} is defined by the existence of a solution of transcendental Eq. (11). This problem comes up for every layer; therefore, the global solution for a given incident amplitude, in general, may not be unique, because the thickness of each plasma layer is not uniquely fixed, with the realization of each specific solution depending on the prehistory of the process. This is also confirmed by our preliminary simulations based on a hydrodynamics approach, where, at fixed incident amplitude, the thickness of various electron layers in the quasi-stationary stage is quite different, depending on the turn-on shape of the incident radiation. The appearance of nonunique solutions is typical of phenomena involving nonlinear media (see, e.g., [12]).

For the sake of concreteness, in what follows, we choose the next boundary position x_2 as the point where the electron density vanishes; i.e., $n(x_2) = 0$. In this case, transcendental Eq. (11) always has nontrivial solutions, because, if the condition given by Eq. (13) is satisfied for the semi-infinite layer, it will automatically be satisfied for all the preceding electron layers, for the point where the electron density vanishes. As follows from Eq. (16), the field at this boundary is such that

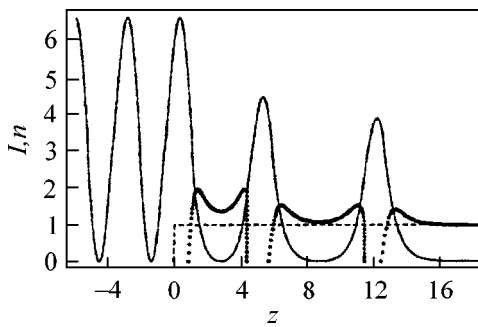$$3n_o(1 + a_2^2)^{1/2} = 2(a_2^2 - \mathcal{H}_2) \qquad (17)$$

Fig. 2. The continuous line represents the plasma-field structures in a semi-infinite plasma initially occupying the region $x \geq 0$ for $n_o = 1.6$, the unperturbed electron density being represented by the dashed line. The dotted line represents the resulting electron density distribution. All quantities are dimensionless.

and, making use of the equation for Hamiltonian (14), we can calculate the first derivative of the field. Thus, for the next depletion layer located within $x_3 < x < x_2$, we know the boundary values of a_2 and a_2' that are required to generate a solution by using the same procedure as before for $x_1 < x < x_0$. This procedure is repeated for every layer $x_{i+1} < x < x_i$ up to the final layer; and, if $\mathcal{H}_i > n_o$, the field solution has to be taken as in the second expression of Eq. (15). The last layer will be a depletion region $0 < x < x_N$, where $x = 0$ is the real plasma–vacuum boundary. At this point, the electric field due to charge separation must vanish. Integrating Poisson's equation over the plasma interval, the plasma neutrality condition gives

$$x_0 = \frac{1}{n_0} \frac{a_N a_N'}{\sqrt{1 + a_N^2}}, \tag{18}$$

which defines the last free parameter. Thus, matching the solution for the field to the vacuum solution at the electron layer boundary $x = x_N$, we can relate the obtained plasma-field distribution to the incident electromagnetic wave. In this way, we can construct an exact stationary solution for the anomalous penetration regime. An example of such a solution is presented in Fig. 2. Notice that the maximum of the electron density in a layer increases from layer to layer, reaching an absolute maximum in the last layer nearest to the vacuum boundary, while the width of the layers becomes more and more narrow. This may be easily understood from Fig. 1: higher lying trajectories have higher values of the integrals of motion. It also means that, at higher incident wave amplitudes, there are more layers, so that the penetration length will increase with increasing incident intensity. These solutions can naturally be extended to cover the case of plasma slabs with finite

thickness, if the penetration length is smaller than the slab thickness.

The following consequence of the previous analysis should be emphasized: for a fixed amplitude, the laser field penetrates only a finite length into the overdense plasma. Consequently, if the incident laser pulse has a finite duration, the electromagnetic energy deposited in the plasma will be reflected back into the vacuum after the laser field has vanished. Evidently, the transient regime will be more complicated if vacuum (depletion) regions surrounded by electron layers show a resonator-like behavior, with the electromagnetic energy excited by the incident pulse. We expect this field structure to evolve and be slowly reflected back into the vacuum region.

In conclusion, we have presented a new class of exact analytical stationary solutions describing a new feature of the interaction between a superintense laser and an overdense plasma. This analysis shows how, depending on the initial plasma density, the interaction can result in the generation of a new plasma field structure consisting of alternating electron and "vacuum" regions, with the electromagnetic energy penetrating into the overdense plasma over a finite length determined by the incident intensity.

REFERENCES

1. S. C. Wilks and W. Kruer, IEEE J. Quantum Electron. **33**, 1954 (1997); see also in *Superstrong Fields in Plasmas: 1st International Conference, Varenna, 1997*, Ed. by M. Lontano *et al.* (American Inst. of Physics, Woodbury, 1998), AIP Conf. Proc., Vol. 426.
2. A. I. Akhiezer and R. V. Polovin, Sov. Phys. JETP **3**, 696 (1956).
3. P. Kaw and J. Dawson, Phys. Fluids **13**, 472 (1970).
4. C. Max and F. Perkins, Phys. Rev. Lett. **27**, 1342 (1971).
5. J. H. Marburger and R. F. Tooper, Phys. Rev. Lett. **35**, 1001 (1975).
6. C. S. Lai, Phys. Rev. Lett. **36**, 966 (1976); F. S. Felber and J. H. Marburger, Phys. Rev. Lett. **36**, 1176 (1976).
7. E. Lefebvre and G. Bonnaud, Phys. Rev. Lett. **74**, 2002 (1995).
8. H. Sakagami and K. Mima, Phys. Rev. E **54**, 1870 (1996).
9. S. Guerin, P. Mora, J. C. Adam, *et al.*, Phys. Plasmas **3**, 2693 (1996).
10. V. V. Goloviznin and T. J. Schep, Pis'ma Zh. Éksp. Teor. Fiz. **70**, 445 (1999) [JETP Lett. **70**, 450 (1999)].
11. F. Cattani *et al.*, Phys. Rev. E (in press).
12. A. G. Litvak, Rev. Plasma Phys. **10**, 294 (1992).

High-Density Phenomena in Hydrogen Plasma[1]

V. S. Filinov*, M. Bonitz**, and V. E. Fortov***

* Mercator guest professor at Rostock University
** Fachbereich Physik, Universität Rostock, D-18051 Rostock, Germany
*** High Energy Density Research Center, Joint Institute for High Temperatures, Russian Academy of Sciences, Izhorskaya ul. 13/19, Moscow, 127412 Russia
Received June 27, 2000; in final form, August 1, 2000

A novel path-integral representation of the many-particle density operator is presented which makes direct Fermionic path-integral Monte Carlo simulations feasible over a wide range of parameters. The method is applied to compute the pressure, energy, and pair distribution functions of a hydrogen plasma in the region of strong coupling and strong degeneracy. Our numerical results allow one to analyze the atom and molecule formation and breakup and predict, at high density, proton ordering and pairing of electrons. © 2000 MAIK "Nauka/Interperiodica".

PACS numbers: 52.25.Kn; 52.65.Pp

Coulomb systems continue to attract the interest of researchers in many fields, including plasmas, astrophysics and solids; see [1, 2] for an overview. The most interesting phenomena, such as metallic hydrogen, plasma phase transition, bound states, etc., occur in situations where the plasma is both strongly coupled and strongly degenerate. However, in this region, the thermodynamic properties of the plasma are only poorly known. The need for the simultaneous account of strong Coulomb and quantum effects makes a theoretical treatment very difficult. Among the most promising theoretical approaches to these systems are path-integral quantum Monte Carlo (PIMC) techniques; see, e.g., [3, 4].

In this letter, we demonstrate that for many current problems in dense warm plasmas ($k_B T > 0.1$ Ry), direct PIMC simulations can, in fact, be carried out with acceptable efficiency. We report results for the internal energy, equation of state, and pair distribution functions of partially ionized hydrogen in a wide range of coupling and degeneracy parameters, $\Gamma = (4\pi n_e/3)^{1/3} e^2/4\pi\epsilon_0 k_B T$ and $\chi = n_e \lambda_e^3$ (λ_e is the electron thermal wave length $\lambda_e^2 = 2\pi\hbar^2\beta/m_e$). Furthermore, our calculations predict ordering of protons, as well as pairing of electrons, at high density.

As is well known, the thermodynamic properties of a quantum system are fully determined by the partition function Z. For a binary mixture of N_e electrons and N_i

protons, Z is conveniently written as

$$Z(N_e, N_i, V, \beta) = Q(N_e, N_i, \beta)/N_e! N_i!,$$

$$Q(N_e, N_i, \beta) = \sum_{\sigma} \int_V dq\, dr\, \rho(q, r, \sigma; \beta). \tag{1}$$

Here, $q \equiv \{\mathbf{q}_1, \mathbf{q}_2, \ldots, \mathbf{q}_{N_i}\}$ comprises the coordinates of the protons and $\sigma = \{\sigma_1, \ldots, \sigma_{N_e}\}$ and $r \equiv \{\mathbf{r}_1, \ldots, \mathbf{r}_{N_e}\}$ are the electron spins and coordinates, respectively. The density matrix ρ in Eq. (1) is represented in the standard way by a path integral [5]:

$$\rho(q, r, \sigma; \beta) = \frac{1}{\lambda_i^{3N_i} \lambda_\Delta^{3N_e}} \sum_P (\pm 1)^{\kappa_P} \int_V dr^{(1)} \ldots dr^{(n)} \tag{2}$$

$$\times \rho(q, r, r^{(1)}; \Delta\beta) \ldots \rho(q, r^{(n)}, \hat{P} r^{(n+1)}; \Delta\beta) \mathscr{S}(\sigma, \hat{P}\sigma'),$$

where $\Delta\beta \equiv \beta/(n+1)$ and $\lambda_\Delta^2 = 2\pi\hbar^2\Delta\beta/m_e$. Further, $r^{(n+1)} \equiv r$ and $\sigma' = \sigma$; i.e., the particles are represented by fermionic loops with the coordinates (beads) $[r] \equiv [r, r^{(1)}, \ldots, r^{(n)}, r]$. The electron spin gives rise to the spin part of the density matrix $\mathscr{S}$, whereas exchange effects are accounted for by the permutation operator $\hat{P}$ and the sum over the permutations with parity κ_P. Following [3, 6, 7], we use a modified representation (3) of the high-temperature density matrices on the r.h.s. of Eq. (2), which is suitable for efficient direct fermionic PIMC simulations of plasmas. With the error of order $\epsilon \sim (\beta Ry)^2 \chi/(n+1)$ vanishing with a growing number of beads, we obtain the approximation

$$\sum_{\sigma} \rho(q, r, \sigma; \beta) = \frac{1}{\lambda_i^{3N_i} \lambda_\Delta^{3N_e}} \sum_{s=0}^{N_e} \rho_s(q, [r], \beta),$$
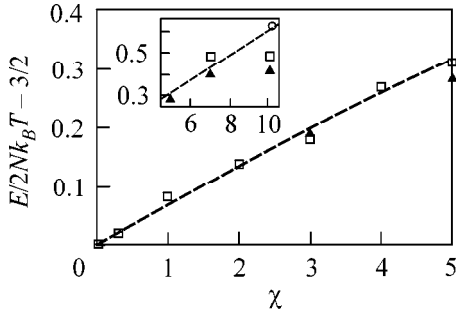

Fig. 1. Energy *E* of an *ideal* plasma of degenerate electrons and classical protons in excess of the classical energy. PIMC simulation results with varied particle number are shown: *N* = 32 (triangles), *N* = 50 (squares), and *N* = 90 (circles) are compared to the exact analytical result (dashed line).

$$\rho_s(q, [r], \beta) = \frac{C_{N_e}^s}{2^{N_e}} \exp\{-\beta U(q, [r], \beta)\}$$

$$\times \prod_{l=1}^{n} \prod_{p=1}^{N_e} \phi_{pp}^l \det|\psi_{ab}^{n,1}|_s, \tag{3}$$

$$U(q, [r], \beta) = U^i(q) + \sum_{l=0}^{n} \frac{U_l^e([r], \beta) + U_l^{ei}(q, [r], \beta)}{n+1},$$

where U^i, U_l^e, and U_l^{ei} denote the sum of the binary interaction Kelbg potentials Φ^{ab} [8] between protons, electrons at vertex *l*, and electrons (vertex *l*) and protons, respectively.

In Eq. (3), $\phi_{pp}^l \equiv \exp[-\pi|\xi_p^{(l)}|^2]$ arises from the kinetic energy density matrix of the electron with index *p*, and we introduced dimensionless distances between neighboring vertices on the loop, $\xi^{(1)}, \ldots, \xi^{(n)}$. Thus, explicitly, $[r] \equiv [r; r + \lambda_\Delta \xi^{(1)}; r + \lambda_\Delta (\xi^{(1)} + \xi^{(2)}); \ldots]$. The exchange matrix is given by

$$\|\psi_{ab}^{n,1}\|_s \equiv \left\|\exp\left\{-\frac{\pi}{\lambda_\Delta^2}|(r_a - r_b) + y_a^n|^2\right\}\right\|_s,$$

$$y_a^n = \lambda_\Delta \sum_{k=1}^{n} \xi_a^{(k)}. \tag{4}$$

As a result of the spin summation, the matrix carries a subscript *s* denoting the number of electrons having the same spin projection.

As an example, we present the equation of state $\beta p = \partial \ln Q / \partial V = [\alpha/3V \partial \ln Q / \partial \alpha]_{\alpha=1}$:

$$\frac{\beta p V}{N_e + N_i} = 1 + \frac{(3Q)^{-1}}{N_e + N_i} \sum_{s=0}^{N_e} \int dq \, dr \, d\xi \, \rho_s(q, [r], \beta)$$

$$\times \left\{\left[\sum_{p<t}^{N_i} \frac{\beta e^2}{|q_{pt}|} - \sum_{p<t}^{N_e} |r_{pt}| \frac{\partial \Delta\beta\Phi^{ee}}{\partial|r_{pt}|} - \sum_{p=1}^{N_i}\sum_{t=1}^{N_e} |x_{pt}| \frac{\partial \Delta\beta\Phi^{ie}}{\partial|x_{pt}|}\right.\right.$$

$$- \sum_{l=1}^{n}\left[\sum_{p<t}^{N_e} A_{pt}^l \frac{\partial \Delta\beta\Phi^{ee}}{\partial|r_{pt}^l|} + \sum_{p=1}^{N_i}\sum_{t=1}^{N_e} B_{pt}^l \frac{\partial \Delta\beta\Phi^{ie}}{\partial|x_{pt}^l|}\right] \tag{5}$$

$$\left.+ \frac{\alpha}{\det|\psi_{ab}^{n,1}|_s} \frac{\partial \det|\psi_{ab}^{n,1}|_s}{\partial\alpha}\right\},$$

$$A_{pt}^l = \frac{\langle r_{pt}^l | r_{pt}\rangle}{|r_{pt}^l|}, \quad B_{pt}^l = \frac{\langle x_{pt}^l | x_{pt}\rangle}{|x_{pt}^l|}.$$

Here, α is a length scaling; $\alpha = L/L_0$, $\langle\ldots|\ldots\rangle$ denotes the scalar product; and q_{pt}, r_{pt}, and x_{pt} are the differences of two coordinate vectors: $q_{pt} \equiv q_p - q_t$, $r_{pt} \equiv r_p - r_t$, $x_{pt} \equiv r_p - q_t$, $r_{pt}^l = r_{pt} + y_{pt}^l$, $x_{pt}^l \equiv x_{pt} + y_p^l$, $y_p^l = \lambda_\Delta \sum_{k=1}^{n} \xi_p^{(k)}$, and $y_{pt}^l \equiv y_p^l - y_t^l$. Other thermodynamic quantities have an analogous form.

We demonstrate our numerical scheme for a two-component electron–proton plasma. In the simulations, we used $N_e = N_p = 50$. To test the MC procedure, we first consider a mixture of *ideal* electrons and protons for which the thermodynamic quantities are known analytically, e.g., [9]. Figure 1 shows our numerical results for the pressure, together with the theoretical curve. The agreement, up to the degeneracy parameter χ as large as 10, is evident and improves with increasing particle number. This clearly proves that our method correctly samples the fermionic permutations. Note that for fast generation of a MC sequence of *N*-particle configurations it is necessary to efficiently compute the acceptance probability of new configurations, which is proportional to the absolute value of the ratio of the exchange determinants of two subsequent configurations, while the sign of the determinants is included in the weight function of each configuration.

Let us now turn to the case of *interacting* electrons and protons. We performed a series of calculations in which the classical coupling parameter Γ was kept constant while the degeneracy parameter χ was varied, cf. Fig. 2. One can see that, for weak coupling ($\Gamma = 0.4$) and small degeneracy parameters $\chi < 0.5$, there is good agreement with analytical theories and quantum MC simulations without exchange [10]. However, as expected, with increasing χ and Γ, the deviations grow rapidly. Figure 2 also contains a comparison with restricted path-integral results of Militzer *et al.* [11] (the large triangles) corresponding to values of the coupling parameter in the range of 0.17, ..., 0.672. Evidently, the agreement, in particular, of the energies, is very good. The deviations in the pressure are apparently related to the fixed-node approximation used in [11] and need further investigation.
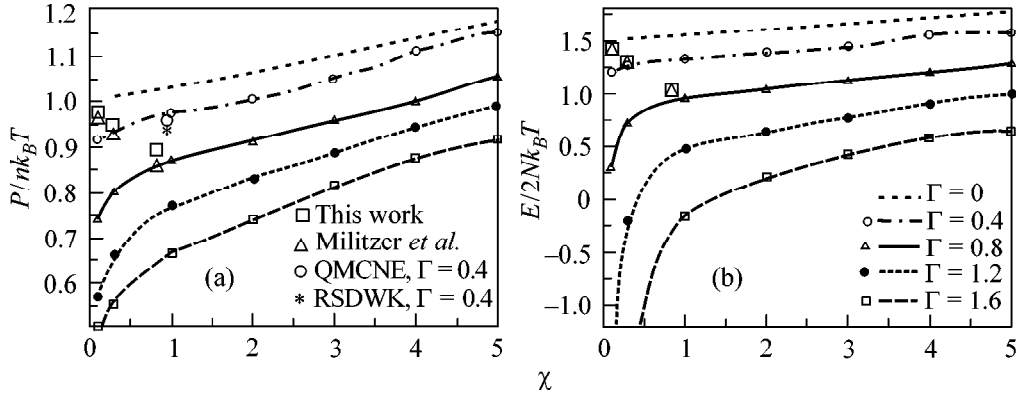
Fig. 2. (a) Pressure P and (b) energy E of the *nonideal* plasma as functions of the quantum parameter χ. Curves correspond to different values of the coupling parameter Γ given in the inset of the right figure. Large circle denotes quantum MC simulations without exchange (QMCNE), and large asterisk denotes the weak coupling model of Riemann *et al.* (RSDWK), using data from [10]. The large triangles are recent restricted PIMC results of Militzer *et al.* [11], which are compared to our results (large squares) for three values of Γ, from top to bottom: $\Gamma = 0.169$, 0.338, and 0.672.
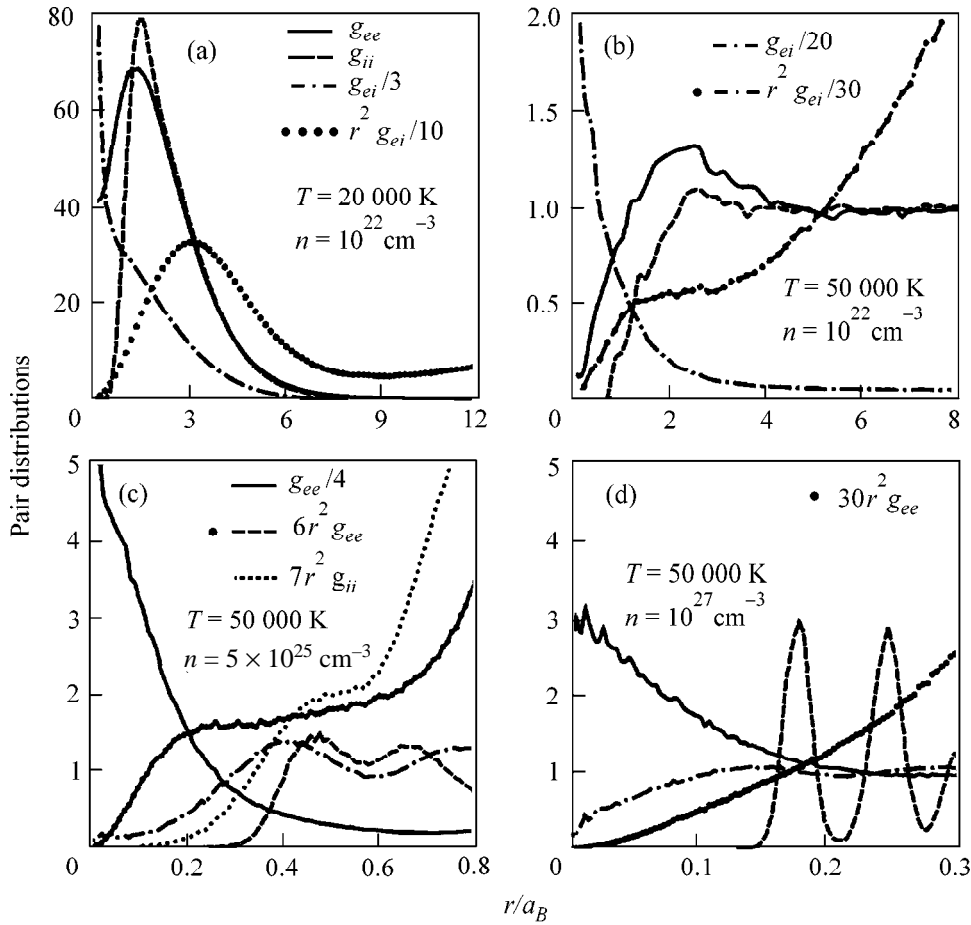
Fig. 3. Electron–electron (g_{ee}, full line), ion–ion (g_{ii}, dashed line) and electron–ion (g_{ei}, dash–dotted line) pair distribution functions for dense hydrogen. The line styles in (b) and (c) are the same as in (a). Notice the varying scalings of the curves. The values for the coupling, degeneracy, and Brueckner parameters are (a) $\Gamma = 2.9$, $\chi = 1.46$, $r_s = 5.44$; (b) $\Gamma = 1.16$, $\chi = 0.37$, $r_s = 5.44$; (c) $\Gamma = 19.8$, $\chi = 1848$, $r_s = 0.318$; and (d) $\Gamma = 53.8$, $\chi = 37.000$, $r_s = 0.117$.

A very interesting result is that the energy curves in Fig. 2 become almost parallel as the degeneracy increases. In contrast, for $\Gamma > 0.6$, reduction of χ leads to a rapid decrease in the energy, which is due to the formation of atoms and molecules, as will be shown below.

The main advantage of the presented method is that it allows one to investigate dense plasmas in a variety

of physical situations which are very difficult to describe reliably by other approaches. This includes partial ionization and dissociation, Mott effect, and ionic ordering at high densities. To investigate these phenomena, we show, in Fig. 3, the pair distribution functions for the four most interesting physical situations. Figure 3a clearly shows the existence of hydrogen molecules (cf. the peaks of the proton–proton and electron–electron pair distribution functions at a separation of about $1.4a_B$) and atoms. We note that the peak of the electron–proton function (multiplied by r^2) in our calculations appears at $r = 1a_B$ if no molecules are present (e.g., at lower density). But for the situation of Fig. 3a, the presence of molecules leads to a shift of the peak to larger distances. Figure 3b shows that, with increasing temperature, atoms and molecules break up, which is clearly seen by the drastic lowering of the mentioned peaks in the pair distribution functions.

Let us now consider the case of higher densities, but keep the temperature constant. Here, our calculations predict interesting physical phenomena. In Figs. 3b–3d, one clearly sees increased ordering of protons from a partially ionized plasma (3b, $\Gamma \approx 1.2$), to liquidlike (3c, $\Gamma \approx 20$) and solidlike (3d, $\Gamma \approx 54$) behavior, cf. the proton–proton pair distribution functions.

Notice further a qualitative change in the electron–electron function upon a density increase from Fig. 3b to 3d: g_{ee} in Fig. 3b is typical of partially ionized plasmas, whereas in Fig. 3c a strong peak at small distances is observed. A further increase in the density leads to an almost uniform electron distribution in Fig. 3d. For better understanding of the electron behavior, we also included in Fig. 3c the functions $r^2 g_{ee}$ and $r^2 g_{ii}$. The shoulders in these curves indicate that the most probable interelectronic distance is almost two times smaller than the average distance between two protons. The reason for the behavior in Fig. 3c is *pairing of electrons* with opposite spin projections. An analysis of the electronic bead distribution allows us to conclude that the "extension" of the electrons is of the order of the interion distance and that there is partial overlap of individual electrons. Under these conditions, pairing of (part of) the electrons minimizes the total energy of the system. This effect vanishes with increasing density due to the growing wave function overlap.

REFERENCES

1. H. E. DeWitt *et al.*, W. Ebeling *et al.*, and D. Klakow *et al.*, in *Proceedings of the International Conference on Strongly Coupled Plasmas*, Ed. by W. D. Kraeft and M. Schlanges (World Scientific, Singapore, 1996).

2. J. Shumway and D. M. Ceperley, in *Proceedings of the International Conference on Strongly Coupled Coulomb Systems, Saint-Malo, France, 1999*; J. Phys. IV **10** (5), 3 (2000); J. P. Hansen, D. Goulding, and R. van Roij, in *Proceedings of the International Conference on Strongly Coupled Coulomb Systems, Saint-Malo, France, 1999*; J. Phys. IV **10** (5), 27 (2000); M. Rosenberg, in *Proceedings of the International Conference on Strongly Coupled Coulomb Systems, Saint-Malo, France, 1999*; J. Phys. IV **10** (5), 73 (2000).

3. V. M. Zamalin, G. E. Norman, and V. S. Filinov, *The Monte Carlo Method in Statistical Thermodynamics* (Nauka, Moscow, 1977).

4. D. Ceperley, *The Monte Carlo and Molecular Dynamics of Condensed Matter Systems*, Ed. by K. Binder and G. Cicotti (SIF, Bologna, 1996).

5. R. P. Feynman and A. R. Hibbs, *Quantum Mechanics and Path Integrals* (McGraw-Hill, New York, 1965).

6. V. S. Filinov, High Temp. **13**, 1065 (1975); **14**, 225 (1976).

7. B. V. Zelener, G. E. Norman, and V. S. Filinov, High Temp. **13**, 650 (1975).

8. G. Kelbg, Ann. Phys. (Leipzig) **12**, 219 (1963); **13**, 354 (1963); **14**, 394 (1964); W. Ebeling, H. J. Hoffmann, and G. Kelbg, Beitr. Plasmaphys. **7**, 233 (1967) and references therein.

9. W. D. Kraeft, D. Kremp, W. Ebeling, and G. Röpke, *Quantum Statistics of Charged Particle Systems* (Akademie, Berlin, 1986; Mir, Moscow, 1988).

10. J. Riemann, M. Schlanges, H. E. DeWitt, and W. D. Kraeft, in *Proceedings of the International Conference on Strongly Coupled Plasmas*, Ed. by W. D. Kraeft and M. Schlanges (World Scientific, Singapore, 1996), p. 82.

11. B. Militzer and D. Ceperley, submitted to Phys. Rev. Lett.

Physical Effect in Ranque Vortex Tubes

V. M. Trofimov

Institute of Theoretical and Applied Mechanics, Siberian Division, Russian Academy of Sciences, Institutskaya ul. 4/1, Novosibirsk, 630090 Russia

e-mail: trofimov@itam.nsc.ru

It is established that application of the model of a continuous medium with distributed internal angular momenta (angular-momentum medium) to the description of real flows in Ranque vortex tubes allows the revelation of a physical effect that is responsible for the experimentally observed separation of temperatures and for some other flow properties. Simplified relations describing changes in the total enthalpy are deduced in the approximations of equilibrium and nonequilibrium thermodynamics. The inhomogeneity of temperature is explained by the properties of a complex (three-parameter) thermodynamic system; its increase is caused by the strengthening of the angular momentum field M under the action of angular velocity Ω in the vortex tube, while its decrease is due to the destruction of this field because of a rapid decrease in vorticity in the near-axial region of the tube. Both these processes provide additional entropy production $2\gamma_t(\Omega - \lambda^{-2}M)^2/T$, where γ_t is the coefficient of rotary viscosity of the angular-momentum medium. The same mechanism is operative in incompressible flows. © *2000 MAIK "Nauka/Interperiodica"*.

PACS numbers: 47.60.+i; 47.32.Cc; 05.70.Ln

The vortex effect [1] lies in the fact that, upon tangential gas inlet into a vortex tube (Fig. 1), the gas flow is separated into two flows: a peripheral flow with total temperature higher than the total temperature of the inlet gas and a central flow with total temperature lower than the total temperature of the inlet gas. Technically, cooling by $\Delta T \approx 50$ K can easily be attained, and, for the best tube constructions, this value may be as high as 200 K. The unusual properties of a gas whirled in Ranque vortex tubes were observed in a great variety of more recent experiments. Among these observations are a sizable increase in flow turbulence in the near-axial region of the tube; an additional abrupt (by ~5 K) decrease in the temperature of the tube wall at the outlet of a cooled gas upon a sharp pressure release at the inlet; the observation of temperature separation in incompressible flows [2]; and the observation of large-scale structures [3].

To explain the main cooling effect, several interpretations were suggested, each based on considering a certain attendant physical factor, such as turbulence, compressibility, and acoustics, or on the "description of a gas (or fluid) flow as a collection of microvolumes with different translational velocities" [2]. The fact that such an "extreme" requirement as the violation of the principle of entropy increase was discussed in connection with this phenomenon, in particular, in the scientific literature [4, 5], is evidence of serious problems in the understanding of its physical origin.

It is established in this work that application of the model of a continuous medium with distributed internal

angular momenta [6] to real flows in Ranque tubes allows at least a qualitative description of the literature experimental data and a quantitative estimation of the main (cooling) effect without violating the laws of thermodynamics.

One of the principal features of the dynamic processes occurring in the Ranque tubes is that the residence time (0.05–0.1 s) of an elementary volume of gas in the tube is much shorter than the characteristic times of ordinary thermodynamic processes. This time should be compared with the characteristic time of establishing dynamic equilibrium for sufficiently large-scale (on the order of λ) vortices (including those of turbulence origin) at the inlet of the Ranque vortex tube. The relaxation time τ of the angular momenta of these vortices in the course of their involvement in the vortex field $\boldsymbol{\Omega}$ of the main (circular) flow in the tube is on the order of λ^2/γ_t, where γ_t is the effective rotary viscosity. According to [7], the $\rho\gamma_t$ value for the turbulent flows in tubes is on the order of $(1.0–0.5) \times 10^{-2}$ kg/(m s). Using this estimate for the rotary viscosity in the vortex tube and setting $\lambda \sim R_0$ (where R_0 is the tube radius), one arrives at a value of $\tau \sim 0.05$ s for the relaxation time, which is comparable to the time of residence of an elementary volume of gas in the Ranque tube. Because of this, the excess angular momenta arising in volumes of the order of λ, in contrast to rigid rotation, have no time to relax, as a result of which a field of internal angular momenta $\mathbf{M}$ with zero volume average is retained in the flow. For such systems, the moment of external forces is equal to the increment (per unit time) in the gas angu-
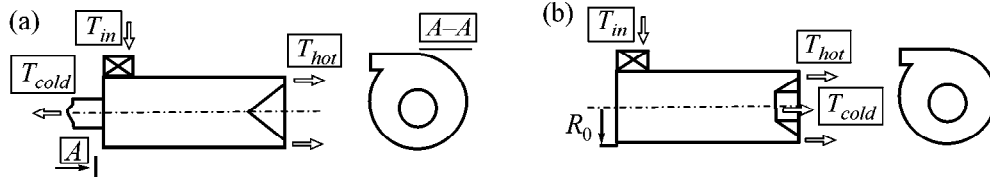
Fig. 1. Principal schemes of the Ranque vortex tube: (a) counterflow and (b) direct-flow.

lar momentum plus the angular momentum transferred to the internal degrees of freedom. In each volume unit, the angular momentum transferred to the internal degrees of freedom is $\sim\gamma_t\nabla\mathbf{v}$. In the classical case, $\gamma_t = 0$, so that this quantity is zero. In the simplest case of linear relationships, a change in the internal angular momentum is estimated as (see also [8])

$$D\mathbf{M}/Dt = \gamma_t\mathbf{\Omega} - \mathbf{M}/\tau; \qquad (1)$$

i.e., the internal angular momentum increases in proportion to the angular velocity $\mathbf{\Omega} = \frac{1}{2}\nabla\mathbf{v}$ of the fluid at a given point and decreases in proportion to its magnitude. In Eq. (1), $\tau = \lambda^2/\gamma_t$ is the relaxation time of the internal angular momentum.

As distinct from ordinary viscous fluids, the stress tensor in a medium with distributed internal angular momenta (angular-momentum medium) has a nonzero antisymmetric component, so that the equation of conservation of angular momentum is not a trivial consequence of the fact that the cross tangential stresses are equal to one another, because $\pi_{ij} \neq \pi_{ji}$. The thermodynamic relations additionally include the work of changing the internal angular momentum under the action of the external rotation field $\mathbf{\Omega}$; i.e., the system is three-parametric [9].

It is known from experiment that the rotation of a gas in the Ranque tube at $r_0 \leq r \leq 0.3R_0$ is close to rigid rotation $v/r = \text{const}$, where v is the circular component of the velocity, R_0 is the tube radius, and r_0 is a certain (small) radius. At $r \geq 0.5R_0$, the flow is close to a potential vortex $vr = \text{const}$, and near the axis it approximately obeys the $vr^{-2} = \text{const}$ law; i.e., the angular velocity near the axis is close to zero.

Let us consider the following model flow in a circular section tube. Gas rotates with an angular velocity whose projection onto the tube axis is Ω, with $\Omega = 0$ near the axis.

The internal energy per unit mass of a medium with distributed internal angular momenta $\mathbf{M}$ (angular-momentum medium) in a coordinate frame rotating with angular velocity Ω can be written, according to [10, 11], in the following model form:

$$u = u_{00} + \frac{1}{2}\lambda^{-2}M^2 - \mathbf{\Omega} \cdot \mathbf{M}.$$

This approach is valid because of the well-known fact that the main fraction of the energy of turbulent motion is concentrated in the vortices of maximum size.

Let, for some ideal angular-momentum medium (equilibrium for $\mathbf{M}$),

$$\partial u/\partial\mathbf{M} = 0, \text{ i.e., } \lambda^{-2}\mathbf{M} - \mathbf{\Omega} = 0,$$

$$u = u_{00} - \frac{1}{2}\lambda^{-2}M^2.$$

The energy conservation law is then written as

$$\delta q = d(u_{00} + p/\rho + v^2/2) - \lambda^{-2}\mathbf{M}d\mathbf{M}.$$

For the adiabatic conditions $\delta q = 0$, one has $0 = di_{00} - \lambda^{-2}\mathbf{M}d\mathbf{M}$, where i_{00} is the stagnation enthalpy. For equilibrious $\mathbf{M}$, $di_{00} = \lambda^2\mathbf{\Omega}d\mathbf{\Omega}$. It is seen that the total enthalpy increases with increasing absolute value of the $\mathbf{M}$ (or $\mathbf{\Omega}$) field and vice versa. Integrating between the states at the inlet (+) and outlet (−) of the Ranque tube, one gets

$$i_{00}^- - i_{00}^+ = \frac{1}{2}\lambda^2(\Omega_-^2 - \Omega_+^2) \approx -\frac{1}{2}\lambda^2\Omega_+^2 \quad (\Omega_- \approx 0). \quad (2)$$

A quantitative estimate with the characteristic angular velocities and sizes $\lambda = R_+$ (R_+ is the inlet pipe radius) yields a value of $-\Delta t = -(30$–$50)$ K coinciding with the experimentally observed temperature decrease. If one draws the curves for the entropy change without applied rotation field in the T–S diagram (Fig. 2),

$$S_0 = c_{M,p}\ln(T_{00}p_{00}^{(1-\gamma)/\gamma}) + \text{const},$$

together with

$$S_M = c_{M,p}\ln(T_{00}p_{00}^{(1-\gamma)/\gamma} - \lambda^2\Omega^2/T_{00}) + \text{const}$$

(it is assumed that $c_{M,p} \approx c_p$), then the cooling effect can be described as a consequence of two equilibrium processes: an isothermal increase in the internal angular momenta $\mathbf{M}$ under the action of the orienting $\mathbf{\Omega}$ field at the periphery of the Ranque tube and an adiabatic decrease in the $\mathbf{M}$ field under the action of a reorienting factor of turbulent chaos arising on the λ scale because of a rapid decrease in the $\mathbf{\Omega}$ field near the tube axis. The process is isothermal because the released heat is removed due to turbulent transfer, while the gas flows out through the peripheral discharge channel. It should be emphasized that the thermodynamic processes of increase and decrease in the $\mathbf{M}$ field in a three-parame-

ter system are, in a sense, analogous to the processes occurring in other three-parameter systems, e.g., to the processes of magnetization and demagnetization known in the physics of paramagnets.

The real variations of the **M** and **Ω** fields in the Ranque tube and in the corresponding model flow are due to inhomogeneous processes. In this work, an attempt is undertaken to carry out thermodynamic analysis for a gas microvolume.

The energy conservation law for a microvolume of an ideal angular-momentum medium is written as

$$\frac{di_{00}}{dt} = \lambda^{-2} M \frac{dM}{dt}. \tag{3}$$

It is convenient to divide the problem into two simpler partial problems: (a) an increase in the **M** field in a stationary angular velocity field Ω_0 and (b) a decrease in the **M** field upon an abrupt decrease in the angular velocity field to a small (ω_0) level.

Integrating the set of Eqs. (1) and (2) for the first problem, one gets for the increasing **M** field

$$|\Delta i_{00}| = \frac{\lambda^2}{2}$$
$$\times \left\{ \Omega_0^2 \left[1 - \left(1 - \frac{\lambda^{-2} m_0}{\Omega_0} \right) \exp(-\gamma_t \lambda^{-2} t) \right]^2 - (\lambda^{-2} m_0)^2 \right\}, \tag{4}$$

where $\Omega_0 = \Omega_z$ and m_0 is the initial internal angular momentum at the tube inlet. On the one hand, the m_0 value can be specified from the roughness of the inlet nozzle walls as a new boundary condition formulated within the framework of the adopted continuum model. On the other hand, the tangential gas inlet into the tube gives rise to a shear layer in the region where a high-velocity inlet flow contacts the lower velocity flow in the Ranque tube. The axes of the vortices originating in this region are predominantly aligned with the angular velocity vector of the main vortex. These vortices can more greatly contribute to m_0, thus diminishing undesirable gas heating, e.g., while achieving the cooling effect. Note that this assumption is confirmed by the optimum inlet shape—planar and extended along the axis of the Ranque tube—that was empirically determined for technical devices.

With the second problem, for the near-axial **M** field one has

$$-|\Delta i_{00}| = \frac{\lambda^2}{2}$$
$$\times \left\{ \omega_0^2 \left[1 - \left(\frac{\Omega_0}{\omega_0} - 1 \right) \exp(-\gamma_t \lambda^{-2} t) \right]^2 - \Omega_0^2 \right\}, \tag{5}$$

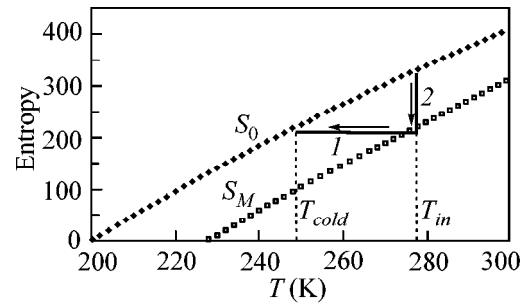where ω_0 is the low angular velocity in the near-axial region.

Fig. 2. *T–S* diagram; (*1*) adiabatic decrease and (*2*) isothermal increase in the **M** field.

It is seen from Eqs. (4) and (5) that (a) the increase in **M** is accompanied by the release of heat, which must be removed from the working zone, and (b) both processes can be efficient only if the time $\tau_0 = \lambda^2/\gamma_t$ is shorter than the time of residence of a microvolume in the Ranque tube, i.e., if the sizes of the vortices, whose angular momenta undergo, respectively, orientation and reorientation, are small enough. This condition competes with the requirement that the λ^2 value be large enough for the cooling effect to be achieved in the steady-state regime [see Eq. (5) for $t \longrightarrow \infty$ and Eq. (2)]. This may serve as a plausible explanation of the fact that the Ranque tube has optimum sizes.

Both the increase and decrease in the **M** field are accompanied by considerable entropy production. The expression for the latter includes the $2\gamma_t(\Omega - \lambda^{-2} M)^2/T > 0$ term (the entire expression for the entropy production in a viscous fluid with internal rotations is given in [12]). Therefore, the temperature separation (ordering) in a vortex flow proceeds via the above-mentioned processes, in full conformity with the principle of entropy increase.

The intensification of the flow turbulence near the Ranque tube axis is explained by the fact that the mechanical energy of the ordered **M** motion converts into turbulent chaos on the λ scale. An additional abrupt decrease in the temperature of the outlet tube wall, which was observed in [13] upon a sharp release in the input pressure, can be caused by an additional decrease in the angular velocity ω_0 [see Eq. (5)] in the near-axial region.

The right-hand side of the equations of motion of the angular-momentum medium contains a term proportional to $\nabla \times (\lambda^{-2} \mathbf{M} - \mathbf{\Omega})$ (angular-momentum stresses), which may change sign near the tube axis, thereby explaining the experimentally observed [13] counterrotation of a thin rod placed at the tube axis. Note that, within the framework of the thermodynamic system of interest, the counterrotation may be dictated in itself by the Le Chatelier principle, when it is considered that the angular velocity field **Ω**, being the external factor with respect to this thermodynamic system, sharply changes its magnitude near the Ranque tube axis.

One can readily verify that the dynamics of internal angular momenta lead to temperature separation in the incompressible fluids as well, which was also experimentally observed in [2].

REFERENCES

1. G. L. Ranque, J. Phys. Radium **4**, 112 (1933).

2. A. F. Gutsol, Usp. Fiz. Nauk **167**, 665 (1997) [Phys. Usp. **40**, 639 (1997)].

3. V. A. Arbuzov, Yu. N. Dubnishchev, A. V. Lebedev, *et al.*, Pis'ma Zh. Tekh. Fiz. **23** (23), 84 (1997) [Tech. Phys. Lett. **23**, 938 (1997)].

4. G. V. Skornyakov, Pis'ma Zh. Tekh. Fiz. **21** (23), 1 (1995) [Tech. Phys. Lett. **21**, 949 (1995)].

5. G. V. Skornyakov, Zh. Tekh. Fiz. **66** (1), 3 (1996) [Tech. Phys. **41**, 1 (1996)].

6. Y. A. Berezin and V. M. Trofimov, Continuum Mech. Thermodyn. **7**, 415 (1995); Izv. Akad. Nauk, Mekh. Zhidk. Gaza **1**, 47 (1996).

7. Yu. V. Nemirovskiĭ and Ya. L. Heĭnloo, Izv. Sib. Otd. Akad. Nauk SSSR, Ser. Tekh. Nauk **3** (13), 74 (1978).

8. V. S. Sorokin, Zh. Éksp. Teor. Fiz. **13** (7–8), 306 (1943).

9. V. V. Sychev, *Complex Thermodynamic Systems* (Nauka, Moscow, 1970), p. 232.

10. L. D. Landau and E. M. Lifshitz, *Statistical Physics* (Akad. Nauk SSSR, Moscow, 1964; Pergamon, Oxford, 1980).

11. M. I. Shliomis, Zh. Éksp. Teor. Fiz. **51**, 258 (1966) [Sov. Phys. JETP **24**, 173 (1966)].

12. S. R. de Groot and P. Mazur, *Nonequilibrium Thermodynamics* (North-Holland, Amsterdam, 1962; Mir, Moscow, 1964).

13. V. E. Fin'ko, Zh. Tekh. Fiz. **53**, 1770 (1983) [Sov. Phys. Tech. Phys. **28**, 1089 (1983)].

Translated by V. Sakun

Localization of Long-Lived States in *trans*-Poly(acetylene): Probing by Photoinduced Polarimetry

V. A. Ruilova-Zavgorodniĭ*, D. Yu. Paraschuk*, and V. M. Kobryanskiĭ**

* Faculty of Physics, Moscow State University, Vorob'evy gory, Moscow, 119899 Russia
e-mail: paras@polys.phys.msu.su
** Semenov Institute of Chemical Physics, Russian Academy of Sciences, ul. Kosygina 4, Moscow, 117997 Russia
Received July 20, 2000

A weak polarization response of the photoexcited states of a conjugated π-electron chain is investigated by cw photoinduced polarimetry. The experiments are carried out with films and solutions of isotropic nano-poly(acetylene) at room temperature. It is found that the polarization response is caused by a weak linear dichroism of the long-lived excited state of nano-*trans*-poly(acetylene) with a ratio of ≈0.6 between the absorption coefficients of light polarized transverse to and along the polymer chain. It is suggested that the π electrons in long-lived states of nano-*trans*-poly(acetylene) are localized at several C–C bond lengths. © *2000 MAIK "Nauka/Interperiodica".*

PACS numbers: 78.66.Qn; 71.24.+q; 42.70.Jk; 33.55.Ad

In recent decades, the physics of elementary excitations in polymer chains containing a π-conjugated system has attracted the particular attention of researchers. The π-conjugated chains are characterized by strong coupling between electronic and lattice degrees of freedom, for which reason a considerable fraction of the excited electronic energy relaxes nonradiatively. The relaxation results in long-lived states, which are commonly related to excitations of the excitonic and/or polaronic types. In particular, it was found for the chemically simplest conjugated poly(acetylene) polymer $(CH)_x$ that the lowest lying excitations do not bear charge (are neutral) [1] and show a photoinduced absorption band slightly below the main dipolar $|1A_g\rangle \longrightarrow |1B_u\rangle$ transition [2].

The delocalization of the π electrons along the polymer chain leads to a strong anisotropy of the optical properties of conjugated polymers. One should expect that the anisotropy will also be seen in the transitions from excited states. The degree of this anisotropy is characterized by the dichroism, i.e., the ratio of absorption coefficients for the probe beams polarized along and transverse to the direction of the excited chains. The data on such an anisotropy allows one to draw conclusions about the degree of localization of π electrons in the excited states of conjugated polymers. We are interested in the relaxed excited states of the neutral type for $(CH)_x$, i.e., on the time scale for which the lattice has time to follow the excitation of the electronic subsystem. Information on the dichroism of the excited chains can be obtained from experiments with nonoriented samples by measuring the absorption coefficients $\delta\alpha_\parallel$ and $\delta\alpha_\perp$ for a probe beam polarized parallel and perpendicular to the polarization of the pump beam, respectively. Such measurements, including those with high time resolution, were carried out for $(CH)_x$ in [3–5]. However, the depolarization signal in these measurements might have been contributed, aside from the dichroism of the excited polymer chain, by other effects, e.g., by excitation diffusion along the chaotically bent polymer chains [3] or by rotation of the axes of the polarizability tensor in the excited state [6]. Moreover, the depolarization signal from the neutral excitations of nonoriented $(CH)_x$ samples lost memory of the polarization of exciting light in hundreds of picoseconds after excitation [4]. An isotropic response to the cw excitation was also observed for oriented $(CH)_x$ samples [7]. At the same time, a high-sensitivity polarimetry technique [8] allowed one to gain information on a weak optical anisotropy that is not seen in the depolarization signal from the excited states. A time-resolution version of this technique was previously used for probing a hidden excited-state anisotropy in inorganic semiconductors [9, 10]. In this work, data on the degree of localization of π electrons in the long-lived neutral excited states of *trans*-$(CH)_x$ were obtained. The experiments were performed by the method of cw photoinduced polarimetry for isotropic samples of nano-poly(acetylene).

Nano-$(CH)_x$ consists of $(CH)_x$ particles of sizes <30 nm dispersed in a transparent matrix of poly(vinyl butyral) with a mass content of 1–2% [11]. The $(CH)_x$ nanoparticles are globule-shaped and formed from the structurally organized π-conjugated chains. The absorption spectrum of nano-$(CH)_x$ shows a sharp edge and a pronounced vibronic structure with zero-phonon line of *trans* isomer at a wavelength of 730 nm. The concentration of the *trans* isomer was higher than the
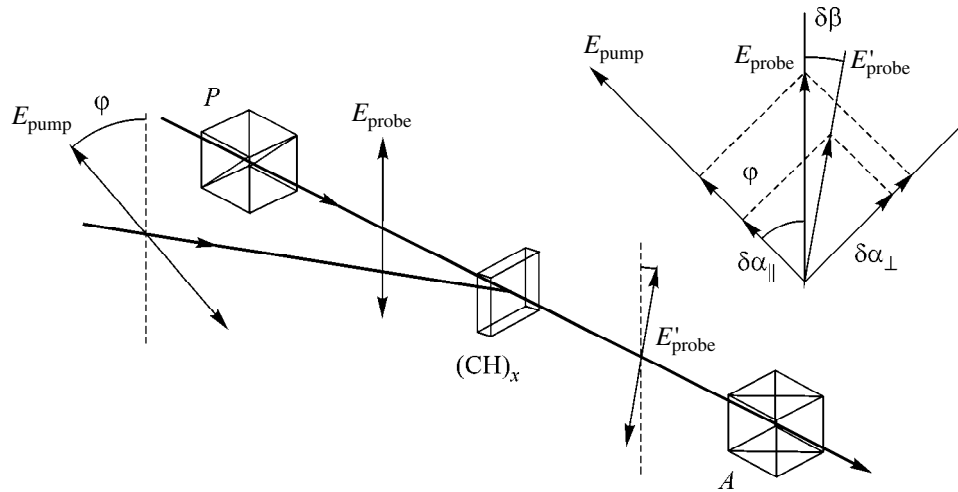
Fig. 1. Scheme of a polarimeter. P is the polarizer; A is the analyzer; E_{pump} and $E_{\text{probe}}(E'_{\text{probe}})$ are the polarizations of the pump and probe beams, respectively; and $\delta\beta = \angle(E_{\text{probe}}, E'_{\text{probe}})$ is the angle of rotation of the polarization of the probe beam after the interaction with the $(CH)_x$ sample. The vectors of interacting fields are shown in the inset; the magnitudes of photoinduced absorption and dichroism are strongly exaggerated.

concentration of the *cis* isomer, as was estimated from the absorption spectra of the samples. The experiments were conducted at room temperature with nonoriented samples of optical density ≈ 1 in the form of ≈ 5-μm-thick films on glass substrates and with solutions of $(CH)_x$ nanoparticles in a butanol–poly(vinyl butyral) composition.

The experiments were carried out in a quasi-collinear pump–probe scheme, in which the linearly polarized probe beam changed its intensity and polarization parameters (polarization direction and ellipticity) upon the interaction with the pump beam. Slight changes in the polarization parameters were transformed into changes in the probe beam intensity (Fig. 1) using a polarimeter tuned to the dark position by a specially developed technique [8, 12]. The cw radiation of a semiconductor laser at a wavelength of 835 nm lying within the photoinduced absorption band of nano-*trans*-$(CH)_x$ was used as a probe beam. The excitation was accomplished by the radiation of a He–Ne laser with a power of ≈ 10 mW at a wavelength of 633 nm corresponding to the strong absorption band of nano-*trans*-$(CH)_x$. The pump and probe beams were focused onto the sample as spots of size ≈ 50 μm. The pump beam was modulated by a mechanical chopper with frequency ≈ 800 Hz, and the corresponding changes in the polarimeter transmittance $\delta T/T$ were recorded by a silicon photodetector using the lock-in detection technique.

The linearly polarized pump beam produces an anisotropic distribution of photoinduced states in the isotropic nano-$(CH)_x$, because the chains directed along the beam polarization are excited with higher probability. Since the conjugated chains are strongly anisotropic, one would expect that the absorption from

the excited state would also be anisotropic; i.e., the absorption coefficients $\delta\alpha_\parallel$ and $\delta\alpha_\perp$ of the probe beams polarized, respectively, along and transverse to the pump beam would be different. A weak photoinduced dichroism can be measured by polarimetric methods. Indeed, upon passing through a dichroic sample, a linear polarization differing from the eigen one rotates toward the eigen polarization corresponding to the minimum absorption (inset in Fig. 1), e.g., as in a film polarizer. The polarization rotation angle $\delta\beta$ and the relative change $\delta T/T$ in the transmittance for $\phi = \pi/4$ can easily be determined for weak photoinduced absorption in a sample of thickness l ($\delta\alpha_\parallel l$, $\delta\alpha_\perp l \ll 1$) [12]:

$$\delta\beta = \frac{\delta\alpha_\parallel - \delta\alpha_\perp}{4}l, \tag{1}$$

$$-\delta T/T = \frac{\delta\alpha_\parallel + \delta\alpha_\perp}{2}l. \tag{2}$$

Equations (1) and (2) can be used to obtain the relationship between the photoinduced dichroism ξ and the experimentally measured $\delta\beta$ and $\delta T/T$ quantities:

$$\xi = \frac{\delta\alpha_\parallel - \delta\alpha_\perp}{(\delta\alpha_\parallel + \delta\alpha_\perp)/2} = \frac{4\delta\beta}{-\delta T/T}. \tag{3}$$

Figure 2a shows the signal $\delta T/T$ from the polarimeter with a nano-$(CH)_x$ film, measured at the output of the lock-in detector as a function of the angle β of detuning the analyzer from the dark position. It is seen that the $\delta T/T$ signal has different signs for detunings of different signs, whence it follows that the polarimeter signal is mainly due to the pump-induced polarization rotation (Fig. 1). Indeed, if the probe beam polarization
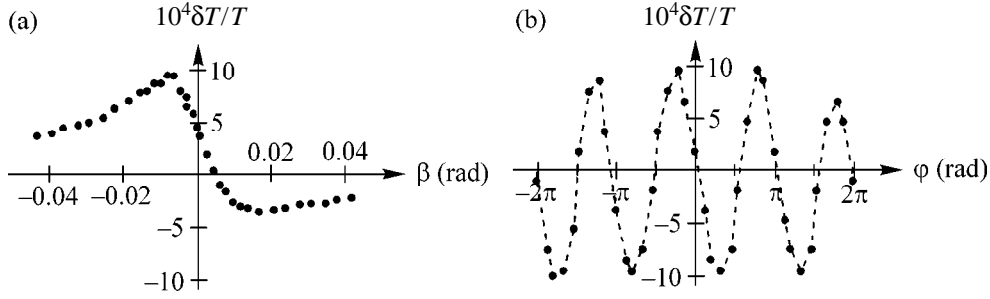
Fig. 2. Transmission signal of a polarimeter with a nano-$(CH)_x$ film vs. (a) the angle β of analyzer detuning from the dark position for $|\phi| = \pi/4$ and (b) the angle ϕ between the polarizations of the pump and probe beams at $\beta \approx -0.01$ rad. The pump polarization was adjusted using a half-wave plate.

turns through a small angle $\delta\beta$ after the interaction with the excited sample, the polarimeter transmission minimum shifts slightly, so that the signals on different sides of the dark position have different signs; i.e., according to Fig. 2a, the polarimeter would "lighten" at $\beta < 0$ and "darken" at $\beta > 0$. It was found that the probe polarization rotated away from the pump polarization, as shown in the inset in Fig. 1. Figure 2b shows the maximum polarimeter signal as a function of the angle ϕ between the pump and probe polarizations. It is seen that the absolute value of the signal is maximum at $\phi = \pm\pi/4$ and minimum at $\phi = 0, \pi/2$. Therefore, the results of polarization measurements are consistent with the above-mentioned picture of interaction between the polarized light and the dichroic medium. The angle of rotation of the probe polarization in the nano-$(CH)_x$ film was found to be $\delta\beta \approx 20$ μrad at $\phi = \pm\pi/4$ at the pump intensity ≈ 0.3 kW/cm^2. The polarization rotation and the photoinduced absorption signals depended linearly on the pump intensity. Note that analogous polarization signals were obtained for solutions of nano-$(CH)_x$. Consequently, the measured photoinduced dichroism is not associated with the effect of a matrix surrounding the $(CH)_x$ nanoparticles.

For large polarimeter detunings from the dark position ($\beta \sim \pi/2$), the measured signal $-\delta T/T \approx 4 \times 10^{-4}$ is mainly due to photoinduced absorption of the $(CH)_x$ film. It does not depend on the orientations of the pump and probe polarizations. Thus, the polarimetric method allows us to observe a weak dichroism of the nano-trans-$(CH)_x$ chains in the photoinduced state. The dichroism can be characterized by the parameter $\xi \approx 0.2$, as defined in Eq. (3).

The coefficients $\delta\alpha_{\parallel}$ and $\delta\alpha_{\perp}$ of photoinduced absorption may be related to the susceptibility tensor $\tilde{\chi}$ in the excited state of nano-$(CH)_x$:

$$\delta\alpha_{\parallel} \propto \text{Im}\tilde{\chi}_{ZZ}, \quad \delta\alpha_{\perp} \propto \text{Im}\tilde{\chi}_{XX}, \qquad (4)$$

where the pump polarization is directed along the Z axis and the pump and probe beams propagate along the Y axis. We assume that the polarizability tensor has a single component γ_{zz} in the chain-fixed system of coordinates. Let us also assume that the excited-state $\tilde{\gamma}$ tensor is diagonal in this coordinate frame. Then, after averaging over the isotropically oriented polymer chains, one obtains the following expressions in the laboratory frame XYZ:

$$\tilde{\chi}_{ZZ} \propto (3\tilde{\gamma}_{zz} + \tilde{\gamma}_{xx} + \tilde{\gamma}_{yy})/15,$$
$$\tilde{\chi}_{XX} \propto (\tilde{\gamma}_{zz} + 2\tilde{\gamma}_{xx} + 2\tilde{\gamma}_{yy})/15. \qquad (5)$$

Note that neglect of the possible excitation-induced rotation of the polarizability tensor of a polymer chain is quite justified. Indeed, if the principal axes of the polarizability tensor γ turn through some angle α upon excitation, then, after angular averaging, this effect will result in the depolarization signal $\sim\alpha^2$ for $\alpha \ll \pi$ rather than in the experimentally observed polarization rotation of the probe beam. Therefore, Eqs. (3)–(5) can be used to obtain the relation between the measured parameter ξ of photoinduced dichroism and the parameter $\tilde{\mu}$ characterizing the ratio of the transverse and longitudinal absorption coefficients for the trans-$(CH)_x$ chain in the photoinduced state:

$$\tilde{\mu} = \frac{\text{Im}(\tilde{\gamma}_{xx} + \tilde{\gamma}_{yy})}{2\text{Im}\tilde{\gamma}_{zz}} = \frac{1 - \xi}{1 + 1.5\xi} \approx 0.6. \qquad (6)$$

It is known that long π-conjugated polymer chains have a strongly anisotropic polarizability tensor γ characterizing the dipolar transition $|1A_g\rangle \longrightarrow |1B_u\rangle$ from the ground state with $\mu \ll 1$. In particular, the high anisotropy of nano-$(CH)_x$ is evident from the results of previous electroabsorption spectroscopy experiments [13, 14]. One usually associates such a strong anisotropy with the delocalization of π electrons over the polymer chain. Indeed, the π-electron motion transverse to the chains is strongly hampered in $(CH)_x$, because the distances between the chains are ≈ 4 Å, while between the carbon atoms in a chain, they are ≈ 1.4 Å. At the same time, the polarization experiments performed in this work are evidence that the absorption anisotropy in the long-lived photoinduced $|2A_g\rangle$ state is tangibly smaller ($\tilde{\mu} \approx 0.6$) than in the ground $|1A_g\rangle$

state ($\mu \ll 1$). Note that the isotropic polarizability corresponds to $\tilde{\mu} = 1$. It is reasonable to explain the weak anisotropy of the $|2A_g\rangle$ state by the fact that the degree of localization of π electrons in this state of the polymer chain is appreciably higher than in the ground state. This inference is consistent with the results of calculations of the chain geometry in *trans*-$(CH)_x$ using the models of the Su–Schrieffer–Heeger–Hubbard type, which suggest (see, e.g., [15]) that the low-lying excited states of the *trans*-$(CH)_x$ chain are characterized by strong local lattice distortions caused by a change in the alternation of the C=C and C–C bond lengths. However, the typical size of the region of local distortion given by these models is on the order of 10–20 C–C bond lengths. If one assumes that the range of local distortion of the *trans*-$(CH)_x$ chain defines the localization range for π electrons in the excited state, then our experimental data give evidence for a considerably higher degree of localization, likely, within a few C–C bond lengths.

In summary, the photoinduced polarimetry method has been used to observe a weak dichroism for the optical transitions from the long-lived photoinduced states of nano-*trans*-$(CH)_x$. According to the suggested interpretation, the observed dichroism is caused by a considerably weaker delocalization of π electrons over the conjugated chain in the photoinduced state, as compared to the ground state.

REFERENCES

1. D. Yu. Paraschuk, T. A. Kulakov, and V. M. Kobryanskii, Phys. Rev. B **50**, 907 (1994).

2. J. Orenstein, in *Handbook of Conducting Polymers*, Ed. by T. A. Skotheim (Marcel Dekker, New York, 1986), Vol. II, p. 1297.

3. Z. V. Vardeny, J. Strait, D. Moses, *et al.*, Phys. Rev. Lett. **49**, 1657 (1982).

4. A. Rosenberg, D. L. Weidman, and D. B. Fitchen, Phys. Rev. B **36**, 6235 (1987).

5. G. S. Kanner and Z. V. Vardeny, Synth. Met. **49–50**, 611 (1992).

6. T. W. Hagler, Chem. Phys. Lett. **218**, 195 (1994).

7. R. H. Friend, D. D. C. Bradley, and P. D. Townsend, J. Phys. D **20**, 1367 (1987).

8. D. Yu. Paraschuk and A. S. Chirkin, Bull. Russ. Acad. Sci., Phys. Suppl. **58**, 63 (1994).

9. N. I. Zheludev and D. Yu. Parashchuk, Pis'ma Zh. Éksp. Teor. Fiz. **52**, 683 (1990) [JETP Lett. **52**, 34 (1990)].

10. N. I. Zheludev, S. V. Popov, Yu. P. Svirko, *et al.*, Phys. Rev. B **50**, 11508 (1994).

11. V. M. Kobryanskii and E. A. Tereshko, Synth. Met. **39**, 367 (1991).

12. V. A. Ruilova-Zavgorodniĭ, Degree Work (Dept. of Physics, Moscow State Univ., Moscow, 1999).

13. D. Yu. Paraschuk, T. A. Kulakov, R. I. Rokitskii, and V. M. Kobryanskii, Synth. Met. **84**, 949 (1997).

14. T. A. Kulakov, Candidate's Dissertation in Physics (Moscow State Univ., Moscow, 1997).

15. R. J. Bursill and W. Barford, Phys. Rev. Lett. **82**, 1514 (1999).

Translated by V. Sakun

Field Emission from Submicron-Grained Tungsten

R. R. Mulyukov*, Yu. M. Yumaguzin**, V. A. Ivchenko***, and L. R. Zubairov*

* Institute of Problems of Metal Superplasticity, Russian Academy of Sciences,
ul. Khalturina 39, Ufa, 450001 Bashkortostan, Russia
e-mail: radik@anrb.ru
** Bashkortostan State University, ul. Frunze 32, Ufa, 450001 Bashkortostan, Russia
*** Institute of Electrophysics, Ural Division, Russian Academy of Sciences, Yekaterinburg, 620049 Russia
Received July 21, 2000

Tungsten specimens subjected to intense plastic strains up to the true logarithmic deformation of $e = 7$ were studied. Transmission electron microscopy revealed a decrease in the mean size of crystal grains down to 100 nm. The field ion- and field electron-emission studies revealed considerable distinctions between the energy distributions for electrons in submicron-grained tungsten and in a coarse-grained metal. © *2000 MAIK "Nauka/Interperiodica".*

PACS numbers: 79.70.+q

In recent years, considerable interest has been attracted to ultrafine-grained materials, which include nanocrystalline materials with a mean size of crystal grains of about 10 nm and submicron-grained (SMG) materials with a mean grain size of about 100 nm (both these types are sometimes referred to as nanocrystalline) [1–4]. The interest is due to the fact that the physical properties of these materials noticeably differ from those of conventional coarse-grained materials. This opens up new possibilities for obtaining materials with prescribed and even record properties. An important role in the formation of the unusual properties of ultrafine-grained materials is played by the high content of grain boundaries in the material volume and by the specific nonequilibrium state of these boundaries [5]. However, the physical nature of the unusual behavior of such materials is still not fully understood. To solve this problem, it seems expedient to study the electronic structure of these materials. At the same time, such studies are of interest by themselves. The changes observed in the physical properties of nanocrystalline and SMG materials allow one to expect that their electronic structure would also exhibit some specific features.

In our previous study [6], we used the method of field electron spectroscopy to study an SMG metal (nickel). We observed qualitative and quantitative changes that occurred in the electron energy distributions as a result of the formation of the SMG structure in this metal. Two types of distributions were revealed for different parts of the emitting surface of the tip. However, analysis of the results of this study was hindered by the lack of experimental data as to where in the microstructure (from the grain bulk or from the vicinity of the grain boundaries) the energy spectra were obtained.

Ultrafine-grained materials are produced by powder techniques, ball grinding, fast cooling of the melt, and by applying heavy plastic strain. The last method [7, 8] provides SMG specimens without pores and impurities. Such specimens are most suitable for studying the physical nature of ultrafine-grained materials.

In the study described in this paper, we obtained SMG metal specimens by the method of intense plastic strains and studied the microstructure and electronic structure of this metal by transmission electron microscopy and by the methods of field ion and field electron emissions.

The material selected for the study was a refractory metal suitable for emission studies, namely, tungsten (99.99% pure). The SMG structure of the specimens was obtained by subjecting them to intense plastic torsional strains under quasistatic pressure in a Bridgman anvil setup until the true logarithmic deformation of $e = 7$ was achieved. To study the microstructure of the SMG specimens, we used a JEM-2000EX transmission electron microscope [9].

Specimens intended for microstructural studies in a field ion microscope were prepared as SMG tungsten needle emitters by electrochemical etching. The curvature radius of the tip of such a needle was ~30–50 nm. The needle was welded to a nickel arc. The field ion microscope was supplied with a microchannel ion–electron converter, which increased the brightness of micrographs by a factor of 10^4. The cooling agent was liquid nitrogen ($T = 78$ K), and the imaging gas was spectrally pure neon.

The field emitters approved for the field emission studies had tips with an atomically smooth surface close to a hemisphere, which was prepared *in situ* by field evaporation of surface atoms. The controlled elim-
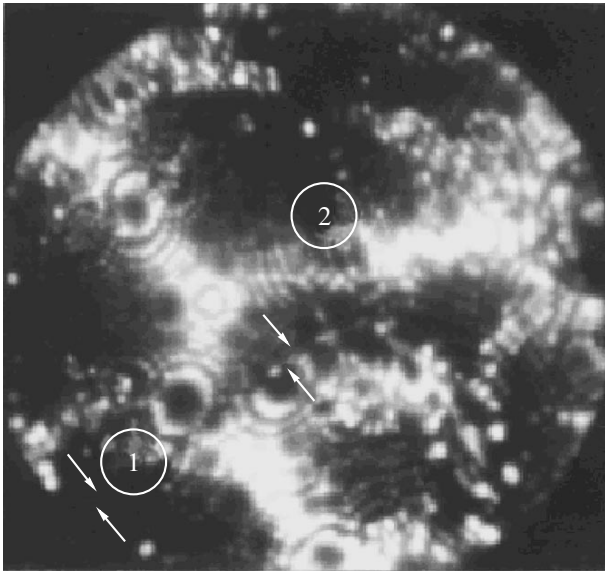
Fig. 1. Field ion image of the surface of SMG tungsten ($V =$ 12.6 kV) with a grain boundary (indicated by arrows). Circles *1* and *2* indicate the surface areas corresponding to the distributions of emitted electrons in the total energy, which are obtained with the field electron spectrometer and shown in Figs. 2a and 2b.

ination of atomic layers from the specimen surface continued until an intercrystalline boundary appeared in the field ion image. The resulting tip with the grain boundary in the emitting area was used as a cathode in the field electron spectrometer to study the electronic structure of the material. Experimental studies were performed in high vacuum ($<10^{-8}$ Pa). The spectrometer contained a field-emission microscope for continuous observation of the emission pattern and a dispersion electrostatic energy analyzer with a resolution of 30 meV or higher [10]. The emission current at the analyzer output was recorded by a secondary-electron multiplier operating in the counting mode. The selection of the emission direction and the tuning to the optical axis of the energy analyzer was performed by a special-purpose manipulator. The size of the probing area of the tip surface was limited by the dimensions of the opening in the screen anode and was about 10 nm. The measurements and the data processing were controlled by using original software and a PC interfaced to a CAMAC system. Immediately before the measurements, the tip was cleaned by the field-desorption method.

To perform a comparative analysis, we studied the tip after it was annealed *in situ* at a temperature near 800°C for 20 min by passing a current through the nickel arc.

As a result of the strain treatment of tungsten, we obtained SMG specimens with a homogeneous granular structure characterized by a mean grain size of about

100 nm [9]. This microstructure was retained in the tips made from SMG tungsten by electrochemical etching.

Figure 1 shows the field ion image of the surface of SMG tungsten with a grain boundary. Such a micrograph of the surface was obtained as a result of evaporation of about 106 atomic layers relative to the {110} face, and the atomic structure of intercrystalline boundaries was studied in the course of eliminating 43 atomic layers. For the subsequent field-emission studies, we selected a high-angle boundary (indicated by arrows in Fig. 1). The analysis of the boundary structure in the volume by means of controlled sequential elimination of surface atoms showed that the crystal structure of this boundary differed from the structure of grain boundaries observed in tungsten not subjected to intense plastic strains. According to our estimates made from the field ion images of the surface, the thickness of the boundary region (the boundary width) does not exceed 0.6–0.8 nm. In undeformed tungsten, the boundary width is 0.3–0.4 nm.

At the next step of our studies, the atomically smooth surface formed for the emitter tip in the field ion microscope was studied in the field electron spectrometer. The energy distributions of field-emission electrons were measured for different areas of the emitting surface of the tip while monitoring the position of each area by the emission image. Although the field electron image visually represented a micrograph whose resolution was an order of magnitude lower than that of the field ion image, the comparison of these two emission images provided the possibility to uniquely identify the microstructure of the areas from which the energy distributions of electrons were obtained. The distributions were measured for 13 areas of the tip by moving the cathode tip in two mutually perpendicular directions with the help of the manipulator.

Two characteristic types of energy distributions were observed for the distribution of field-emission electrons in the total energy, these types being determined by the choice of the emission area on the cathode surface. The spectra obtained from an area containing the grain boundary (Fig. 2a) exhibit an additional maximum in the low-energy region, and this maximum grows with increasing emission voltage.

For the areas that lie away from the grain boundary, the distributions are similar in form to the classical distribution (Fig. 2b). However, the full width at half-height of the spectrum obtained in our experiments sizably (by ~0.4 eV) exceeds the corresponding value for the classical spectrum [11], reaching 0.58–0.64 eV.

As shown in our previous publications [3, 4], the annealing of SMG specimens leads to recovery of their original physical properties. This recovery correlates with the restoration of the microstructure. An *in-situ* annealing of the tip at a temperature of about 800°C for 20 min resulted in a partial recovery of the energy distribution of the emitted electrons (Fig. 3). In our measurements, we observed only one-peak spectra, and,
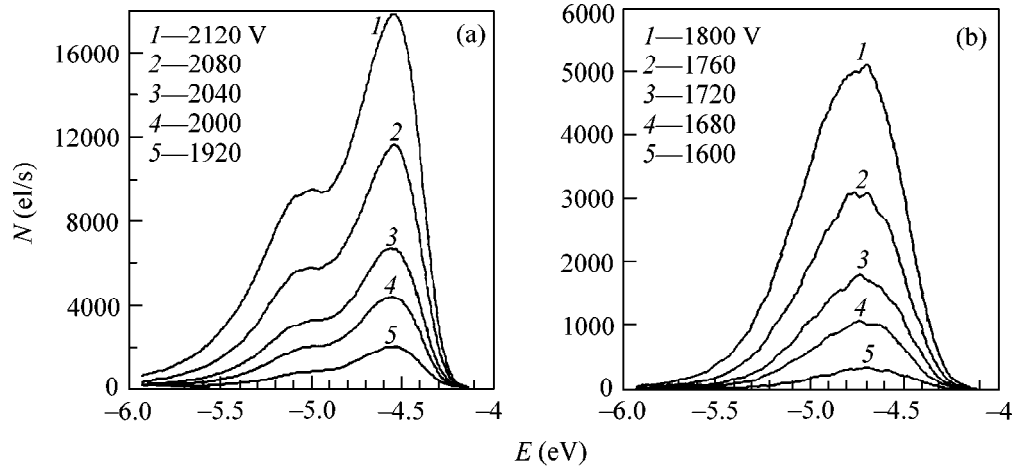
Fig. 2. Distributions of emitted electrons in the total energy at different emission voltages for two areas of emission imaging: (a) area *1* (Fig. 1) containing a grain boundary and (b) area *2* (Fig. 1) lying away from the grain boundary.
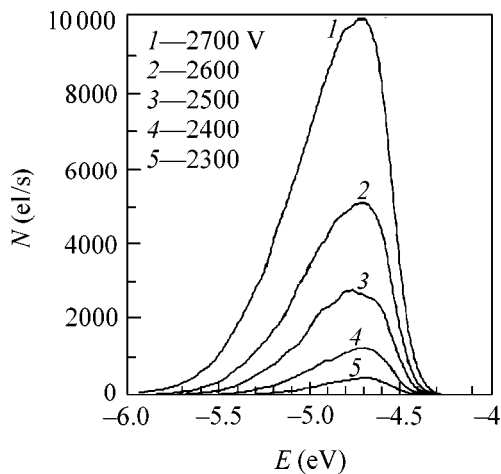

Fig. 3. Distributions of emitted electrons in the total energy at different field emission voltages for a tip annealed at 800°C in vacuum.

after annealing, their full width at half-height decreased to 0.45–0.60 eV.

The measurements of the aforementioned energy distributions with a time lag (30 min) and the same emission voltage did not lead to any changes in the form of the distributions.

Thus, significant differences are revealed between the energy characteristics of electrons emitted from SMG metal and those of electrons emitted from coarse-grained metal. These differences can be caused by the specific features of the microstructure, in particular, by the increased content of grain boundaries in the material structure and by the specific nonequilibrium state of these boundaries. In our previous publications [12–14], it was shown that these boundaries have an effective physical width of about 10 nm, which greatly exceeds the crystallographic width of the grain boundaries, and

the atoms within this width are characterized by a lower Debye temperature and a higher energy [4].

REFERENCES

1. I. D. Morokhov, L. I. Trusov, and V. I. Lapovok, *Physical Phenomena in Ultrahigh-Dispersed Media* (Nauka, Moscow, 1984).
2. R. Birringer and H. Gleiter, in *Encyclopedia of Materials, Science and Engineering*, Ed. by R. W. Cahn (Pergamon, Oxford, 1988), Suppl. Vol. 1.
3. R. Z. Valiev, A. V. Korznikov, and R. R. Mulyukov, Mater. Sci. Eng. A **168**, 141 (1993).
4. R. R. Mulyukov and M. D. Starostenkov, Acta Metall. Sin. **13**, 301 (2000).
5. O. A. Kaĭbyshev and R. Z. Valiev, *Grain Boundaries and Properties of Metals* (Metallurgiya, Moscow, 1987).
6. L. R. Zubairov, E. A. Litvinov, R. R. Mulyukov, *et al.*, Dokl. Akad. Nauk **372**, 319 (2000) [Dokl. Phys. **45**, 198 (2000)].
7. N. A. Smirnova, V. I. Levit, V. P. Pilyugin, *et al.*, Fiz. Met. Metalloved. **61**, 1170 (1986).
8. N. A. Akhmadeev, R. Z. Valiev, V. I. Kopylov, and R. R. Mulyukov, Izv. Akad. Nauk SSSR, Met., No. 5, 96 (1992).
9. R. R. Mulyukov, N. I. Noskova, and L. R. Zubairov (in press).
10. R. Z. Bakhtizin, V. M. Lobanov, and Yu. M. Yumaguzin, Prib. Tekh. Éksp., No. 4, 247 (1987).
11. A. Modinos, *Field, Thermionic and Secondary Electron Emission Spectroscopy* (Plenum, New York, 1984; Nauka, Moscow, 1990).
12. R. Z. Valiev, R. R. Mulyukov, and V. V. Ovchinnikov, Philos. Mag. Lett. **62**, 253 (1990).
13. R. Z. Valiev, R. R. Mulyukov, V. V. Ovchinnikov, and V. A. Shabashov, Scr. Metall. Mater. **25**, 2717 (1991).
14. R. R. Mulyukov, Metalloved. Term. Obrab. Met., No. 8, 34 (1998).

Translated by E. Golyamina

Instability and Reconstruction of a Thin Fluid Film under Inversion Conditions

V. B. Shikin

Institute of Solid-State Physics, Russian Academy of Sciences, Chernogolovka, Moscow region, 142432 Russia
Received June 1, 2000; in final form, July 25, 2000

The development of mechanical instability of a neutral fluid film (liquid helium or hydrogen) under inversion conditions (it does not lie on a solid substrate but hangs from a ceiling) is discussed. Critical parameters of such an instability and the character of surface reconstruction under the action of van der Waals forces, bubble pressure, and gravitational forces are determined. The interrelation with the well-known Frenkel problem of a drop on a solid substrate is pointed out. An electrostatic mechanism is proposed for the stimulation of instability of a thin helium film. This mechanism is promising for the problem of superfluid helium leakage. © *2000 MAIK "Nauka/Interperiodica".*

PACS numbers: 68.45.Kg; 67.70.+n

A fluid film hanging from a solid ceiling (inversed film) belongs to the interesting neutral two-dimensional systems demonstrating mechanical instability. Such film can be formed in a variety of ways. The most popular of them is condensation of a given portion of gas on the cooled walls of a closed reservoir, in particular, on its ceiling. This program was implemented for cryogenic fluids in [1]. Precise control of the admitted gas volume allows the thickness d of a film on the ceiling to be varied over a wide range, starting from micrometers.

A purely gravitational behavior of an inversed film is absolutely unstable. In the presence of the van der Waals forces, the mechanical equilibrium of a homogeneous film becomes possible in a finite range of its thicknesses. As the thickness increases, mechanical stability is lost in the vicinity of some critical value d_*. As in other known cases (e.g., in the problem of a charged thin fluid film [2–4]), this process is developed primarily for small wave numbers.

By analogy with the problem of a massive fluid, one may anticipate that there is a certain inhomogeneous (reconstructed) state of a film in the supercritical region where it is attached to the ceiling by a combination of forces, including bubble pressure. However, the scenario of reconstruction of an inversed film is as yet unclear. Whereas the observed periodic reconstruction of a massive fluid is mainly associated with the instability of finite wave numbers in the vicinity of the so-called capillary length [5–7], there are no such guiding arguments for films (the long-wavelength perturbations are unstable).

A variant of the stable homogeneous state of a fluid under inversion conditions was suggested in the well-known work by Frenkel [8], where the properties of drops on a solid surface tilted at an arbitrary angle to the horizon were discussed. For both incomplete and complete wettings, the drop hangs from a solid ceiling (the gravitational force detaches fluid from the substrate) to achieve the desired inhomogeneous state. However, the statement of the problem in [8] excluded the limiting transition to a homogeneous fluid film, because the van der Waals forces were not taken into account and, hence, the problem of reconstruction did not arise.

In this work, the properties of a neutral liquid helium (hydrogen) film under inversion conditions are considered with the aim of determining the criterion for its stability and elucidating the reconstruction details.

1. Let us first consider a flat thin fluid film of thickness d condensed on a solid ceiling. The equilibrium mechanical properties of the film are determined by two factors: the attraction to the ceiling by the van der Waals forces, which are capable of holding the film on a solid substrate in the flat state, and the gravitation responsible for the possible film instability.

In the standard geometry (a film on a solid substrate), the van der Waals pressure, together with gravitation, produces a monotonic potential

$$P = \rho g d - f/d^3,$$

which holds atoms of the fluid near the substrate and has a positive derivative $\partial P/\partial d > 0$. In this expression, ρ is the volume density of the fluid, g is the acceleration of gravity, and f is the van der Waals interaction constant (the retardation effects are omitted).

If the f constant has the opposite sign (a film on a ceiling), the combination

$$P = \rho g d + f/d^3$$

becomes nonmonotonic and passes through a maximum at the point d_*:

$$\partial P/\partial d_{|d_*} = 0, \quad d_*^4 = 3f/\rho g. \quad (1)$$

If $d > d_*$, the van der Waals forces are insufficient for holding a flat inversed film on the ceiling, so that the problem becomes unstable. However, if a film with $d > d_*$ ceases to be flat,

$$d(x) = d + \xi(x), \quad \int_{-L}^{+L} d(x)dx = 2Ld \quad (2)$$

($2L$ are the horizontal dimensions of the film), one can expect that mechanical equilibrium persists in some range of the δ values, where

$$\delta = (d - d_*)/d_*. \quad (3)$$

This situation is possible because the force balance in this case includes bubble pressure, which also stabilizes the film shape $d(x)$ at $d > d_*$.

It should be noted that all types of fluid films on the ceiling are unstable at nonzero temperatures $T \neq 0$. Nevertheless, if $T \ll T_o$, where T_o is the boiling temperature of a given fluid, one may speak about the metastable (existing for a finite but rather long time) mechanical equilibrium or its absence in a liquid layer with $\delta > 0$. Similar arguments were used in [8] when stating the problem of a drop on a tilted substrate.

The inhomogeneous part of the deformation $\xi(x)$ obeys the equation

$$\alpha\xi'' + \rho g\xi + \frac{f}{(d+\xi)^3} - \frac{f}{d^3} = \text{const}, \quad (\xi')^2 < 1, \quad (4)$$

where α is the surface tension and the z axis is aligned with the direction of the gravitational force. The term f/d^3 is set off from const for the sake of convenience. The limitation $(\xi')^2 < 1$ is not crucial and is used below to simplify the calculations. In addition, it will be shown that the domain of $\delta > 1$ values where the approximation of small gradients applies is sufficient for making qualitative conclusions about the problem of interest.

In the linear approximation $\xi/d \ll 1$, Eq. (4) reduces to

$$a^2\xi'' + \gamma\xi = a^2\lambda, \quad \gamma = 1 - 3f/\rho g d^4, \quad a^2 = \alpha/\rho g. \quad (5)$$

The behavior of Eq. (5) depends on the sign of combination γ, indicating once more that there is a certain critical thickness d_*, as defined in Eq. (1).

In the limit $\gamma \longrightarrow 1$, Eq. (5) transforms to the Frenkel problem [8]. The van der Waals forces drop out of this formalism [at $f \longrightarrow 0$, the constant part d automatically drops out of the $d(x)$ definition in Eq. (2)]. The influence of the substrate on the properties of a fluid drop was taken into account in [8] through the boundary conditions (by specifying wetting angle θ)

$$\xi(\pm l) = 0, \quad \xi'(\pm l) = \tan\theta, \quad \int_{-l}^{+l}\xi(x)dx = S, \quad (6)$$

where $\pm l$ is the point at which the drop profile contacts the substrate.

For a hanging drop with zero wetting angle, one has

$$\xi(x) = \lambda a^2 + 2A\cos(x/a),$$
$$l = \pi a, \quad 2A = \lambda a^2, \quad 2\lambda a^2 l = S. \quad (7)$$

Here, S is the drop volume per unit length. The $\alpha\lambda$ combination has a meaning of pressure in the drop.

It is also instructive to introduce the energy W of the Frenkel drop. Using Eq. (7), one has

$$W = -\frac{\alpha}{2}\int_{-\pi a}^{+\pi a}[(\nabla\xi)^2 - \xi^2/a^2]dx = -\frac{\alpha}{2\pi a^3}S^2, \quad (8)$$

where S is given by Eq. (6). The negative sign of energy W in Eq. (8) needs comments. Let us begin with normalization (6) signifying that the whole fluid mass is assembled as a single drop. However, problem (5), (6) allows an alternative setting: the fluid volume may be distributed among several (for simplicity, identical) drops. Let the number of these drops be equal to N, each having a mass of S/N. The total energy W_* of this complex is

$$W_* = NW_N, \quad W_N = -\frac{\alpha}{2\pi a^3}(S/N)^2,$$
$$W_* \propto N^{-1}, \quad |W_*| < |W|. \quad (8a)$$

If energies (8) and (8a) are positive, the drops will split up at a fixed S to form, in the limit, a homogeneous fluid film. Such behavior is typical of drops with zero wetting angle on a solid substrate. The same conclusion was also drawn in [8]. However, in the inversion case, drop splitting and the formation of a homogeneous film is unnatural (a homogeneous inversed film of macroscopic thickness is absolutely unstable). There is only one way to overcome this paradox: the energies W in Eq. (8) and W_* in Eq. (8a) should be negative (relative to the corresponding energies of a drop on a substrate) in the inversion case, which is stated in Eq. (8). Then, according to Eq. (8a), it is energetically advantageous for the Frenkel drops to coalesce instead of splitting; normalization per drop (6) becomes justified, and the situation becomes quite pictorial: in the problem of transformation of N drops with a fixed S into a single drop, the latter has the "lowest" center of gravity with respect to the ceiling.

2. Let us now turn to the reconstruction problem. In the $z(x) = d(x)/d_*$ terms, the first integral of Eq. (4) is

$$(z')^2 = p(z) + \text{const},$$

$$p(z) = \kappa^2 d_*^2 [-z^2 + 1/(3z^2) + \Lambda z], \quad (9)$$

$$\Lambda = a^2 \lambda/d^*, \quad \kappa^2 = a^{-2}.$$

The condition for periodicity of the $z(x)$ function,

$$(z_{max} + z_{min}) + (z_{max} + z_{min})/3z_{max}^2 z_{min}^2 - \Lambda = 0, \quad (10)$$

relates the extreme points of the inhomogeneous drop profile to each other. For given Λ and z_{max}, Eq. (10) is algebraic (of third degree) with respect to z_{min}. An analysis of the roots of this equation, in conjunction with requirement (2), leads to the conclusion that the solitonic solution is impossible [formally, such a solution does not contradict Eq. (10) and corresponds to an infinite period]. Leaving out the cumbersome general details of this proof, note that the possible solitonic solution in the limit $\delta \ll 1$ gives

$$z(x) = 1 + \xi(x), \quad 2\xi_{min} = -\xi_{max} \quad (11)$$

and should describe a single hill of height $1 + \xi_{max} > 0$ gradually transforming into asymptotic form (11) upon moving away from the hill top. This is precisely the solution which we wish to find for the reconstruction problem with the aim of substantiating the boundary conditions (6) from [8] for the hanging drop. However, solitonic solution (11) contradicts normalization requirement (2) for an arbitrary length L. This statement is also valid in the general case of arbitrary δ values.

The following alternative occurs in the absence of solitons: either the film reconstruction has a periodic character or it is deformed in an aperiodic (not solitonic) fashion. The first assumption is not valid, at least for a massive film, where the reconstruction results in a system of Frenkel drops (7). The coalescence of a group of individual drops is energetically favorable [see Eq. (8a)] but is not necessary. However, if the drops are connected by liquid bridges, the situation changes. The energetic factors and the inevitable fluctuations of drop sizes lead to hydrodynamic growth of large drops at the sacrifice of their smaller neighbors. This process develops relatively slowly (according to the throughput of narrow van der Waals bridges between the drops), so that the use of the term "drop" is especially convenient at the final stages of coalescence. With time, all intermediate drops are "eaten up" by the one which initially had the largest size. The fluid redistribution among different channels resembles the problem of coalescence in a system of pores exchanging vacancies [9].

Considering that soliton (11) cannot appear and taking into account qualitative considerations concerning the instability of a periodic system of drops, it remains to assume that the deformation of an unstable inverted fluid film evolves up to the formation of a single hill (forced soliton) with profile $z(x)$ and characteristic points at z_{min} and z_{max} determined by the expressions

$$\int_{z_{max}}^{z(\zeta)} \frac{d\xi}{\sqrt{p(\xi) - p(z_{max})}} = \zeta, \quad \zeta = \frac{x}{d_*},$$

$$\int_{z_{max}}^{z_{min}} \frac{d\xi}{\sqrt{p(\xi) - p(z_{max})}} = \frac{L}{d_*}. \quad (12)$$

Here, $p(z)$ is defined in Eq. (9), z_{max} and z_{min} are related by Eq. (10), and parameter Λ is defined by requirement (2).

The conclusion about the formation of a single hill (12) in the course of the reconstruction of an inverted fluid film is qualitatively confirmed by experiment [1].

Some analytical estimates of the characteristic parameters of the problem can be obtained for relatively small L values such that $L \geq a$ and $\delta \gg 1$. This can be done using perturbation theory with δ^{-1} as a small parameter.

In zero approximation, the fluid is mainly placed in the gravitational part of the deformed film (i.e., in the region where the thickness $d > d_*$), where the Frenkel profile $z(x)$ (7) is shifted from zero by z_{min}^o. Therefore, the definitions of z_{max}^o and Λ^o are straightforward:

$$z_{max}^o = \Lambda^o - z_{min}^o, \quad \Lambda^o = 2(\delta + 1), \quad \delta \gg 1. \quad (13)$$

The next step consists in the estimation of the z_{min}^o value with the help of Eq. (10). A qualitative distinction between the Frenkel problem and a more consistent theory with the van der Waals forces becomes evident at this step. With the known z_{max}^o and Λ^o values [see Eq. (13)] and taking into account that $z_{min}^o \ll 1$, one has from Eq. (10)

$$(z_{min}^o)^3 \simeq 1/3z_{max}^o \quad \text{or} \quad (d_{min}^o)^3 \simeq d_*^4/3d_{max}^o. \quad (14)$$

With this definition of z_{max}^o, it is easy to continue the refining and estimate the domain of applicability of the suggested perturbation theory. The theory is valid if

$$(L - \pi a)d_{min}^o \ll \pi a d_{max}^o. \quad (15)$$

Requirement (15) is readily fulfilled for $L > \pi a$ if $z_{min}^o \ll z_{max}^o$, i.e., if $\delta \gg 1$.

Let us discuss the assumption $\xi' < 1$ from Eq. 4. This requirement is fulfilled if

$$\xi_{max} < \pi a \quad \text{or} \quad Ld_*(\delta + 1) < \pi^2 a^2, \quad (16)$$

where $\xi(x)$ is defined by Eq. (7). If $d_* \ll a$ or, which is the same, $\kappa d_* \ll 1$, the domain with $\delta > 1$, where condition (16) and, hence, Eq. (4) holds, is extensive enough. For helium, $\kappa^2 \simeq 397$ cm^{-2}. As to the van der Waals constant, its typical value for glass substrates is $f \simeq 10^{-14}$ erg. As a result, the d_* value in Eq. (1) is $d_* \simeq 1.2 \times 10^{-4}$ cm and the combination $\kappa d_* \simeq 2.5 \times 10^{-3}$; i.e., the smallness of $\kappa d_* \ll 1$, necessary for Eq. (16), holds.

To conclude, the gravitational instability of an inverted fluid film and its possible stationary reconstruction are discussed in this work. It is shown (in the one-dimensional approximation) that reconstruction is possible and is aperiodic.

Note also that the stability threshold of an inverted film can be shifted by an electric field, which can easily be introduced into the problem (a film between capacitor plates). The elaboration of this scenario may be helpful in preventing the leakage of superfluid helium through the walls of a Dewar vessel. The results [10–17] on the dynamics of a gravitationally unstable liquid layer may be helpful in studying this problem.

REFERENCES

1. A. Levchenko, G. Kolmakov, L. Mezhov-Deglin, *et al.*, Fiz. Nizk. Temp. **25**, 333 (1999) [Low Temp. Phys. **25**, 242 (1999)].

2. L. P. Gor'kov and D. M. Chernikova, Pis'ma Zh. Éksp. Teor. Fiz. **18**, 119 (1973) [JETP Lett. **18**, 68 (1973)].

3. D. M. Chernikova, Fiz. Nizk. Temp. **2**, 1374 (1976) [Low Temp. Phys. **2**, 669 (1976)].

4. A. P. Volodin, M. S. Khaĭkin, and V. S. Édel'man, Pis'ma Zh. Éksp. Teor. Fiz. **26**, 707 (1977) [JETP Lett. **26**, 543 (1977)].

5. L. P. Gor'kov and D. M. Chernikova, Dokl. Akad. Nauk SSSR **228**, 829 (1976) [Sov. Phys. Dokl. **21**, 328 (1976)].

6. V. I. Mel'nikov and S. V. Meshkov, Zh. Éksp. Teor. Fiz. **82**, 191 (1982) [Sov. Phys. JETP **55**, 1099 (1982)].

7. P. Leiderer and M. Wanner, Phys. Lett. A **73**, 189 (1979).

8. Ya. Frenkel', Zh. Éksp. Teor. Fiz. **18**, 659 (1948).

9. E. M. Lifshitz and L. P. Pitaevskiĭ, *Physical Kinetics* (Nauka, Moscow, 1979; Pergamon, Oxford, 1981).

10. R. Bellman and R. Pennington, Q. J. Appl. Math. **12**, 151 (1954).

11. N. Rajappa, Acta Mech. **10**, 193 (1970).

12. N. Rajappa, J. Phys. Soc. Jpn. **28**, 219 (1970).

13. E. Ott, Phys. Rev. Lett. **29**, 1429 (1972).

14. D. Book and E. Ott, Phys. Fluids **17**, 676 (1974).

15. É. E. Son, Pis'ma Zh. Tekh. Fiz. **4**, 1023 (1978) [Sov. Tech. Phys. Lett. **4**, 413 (1978)].

16. V. Ievlev, Teplofiz. Vys. Temp. **18**, 769 (1980).

17. N. Inogamov, A. Dem'yanov, and É. Son, *Hydrodynamics of Mixing* (Mosk. Fiz.-Tekhnol. Inst., Moscow, 1999), Paragraph 10.

Translated by V. Sakun

Coulomb Blockade under Conditions of Inelastic Tunneling

L. V. Litvin, V. A. Kolosanov, D. G. Baksheev, V. A. Tkachenko, and A. L. Aseev

Institute of Semiconductor Physics, Siberian Division, Russian Academy of Sciences,
pr. Akademika Lavrent'eva 13, Novosibirsk, 630090 Russia,

e-mail: litvin@thermo.isp.nsc.ru

It is found that single-electron current oscillations in the drain–gate characteristics of a single-electron transistor fabricated by the step-edge cutoff process, as compared to a conventional single-electron transistor, are damped several times slower and do not change their phase by π as the source–drain voltage increases. This is explained by the strong nonlinearity of the current–voltage characteristics of tunnel junctions, which is caused by the inelastic character of tunneling. © *2000 MAIK "Nauka/Interperiodica".*

PACS numbers: 73.23.Hk; 73.40.Gk; 73.40.Rw

Single-electron effects were discovered for tunnel junctions with a direct elastic character of tunneling [1–3]. The Coulomb blockade effect in this case is well understood, and, for example, the current–voltage characteristics of a structure with two sequentially connected tunnel junctions can be calculated numerically. At the same time, it follows from the orthodox theory of Coulomb blockade that single-electron effects exist in structures with any conduction mechanism providing a sufficiently high junction resistance ($\gg h/e^2 \approx 26$ kΩ) [1, 4]. Nevertheless, Coulomb blockade has not been studied beyond the conditions of elastic tunneling. In this work, the case of inelastic tunneling in tunnel junctions of a single-electron transistor has been experimentally realized and analyzed.

As the thickness of the insulator interlayer (Si) in a tunnel junction of small area ($S \leq \mu$m^2) increased from 1.3 to 8.3 nm, the following succession of tunneling regimes was observed in [5]: (i) direct tunneling, (ii) resonance and inelastic resonance tunneling, and (iii) a regime resulting in a power law of the corresponding current–voltage characteristic. Based on the theory of inelastic tunneling developed in [6], the last regime can be qualified with confidence as inelastic tunneling through channels containing pairs of localized states. At a certain low temperature, inelastic tunneling is completely suppressed and gives way to elastic (direct and resonance) tunneling. However, when a source–drain voltage is applied, the inelastic channels again become effective because of the excitation of carriers by the field. In this case, two conduction channels, elastic and inelastic, will coexist in the sample.

Lateral tunnel junctions in a Ti nanowire were fabricated by the through oxidation of thin sites that form when the nanowire crosses a step previously etched in the dielectric Si$_3$N$_4$ substrate (Fig. 1) [7]. This is one variety of the step-edge cutoff method. The degree of oxidation under atmospheric conditions was controlled by the thickness of a thin (4–20 nm) high-resistance Ge film deposited over Ti in a single vacuum cycle. The nanowire was about 100 nm in width and 4–9 nm in thickness; it crossed two steps obtained by plasma etching of Si$_3$N$_4$ through a metal mask to a depth of about 15 nm. The steps were spaced at about 100 nm and formed a Coulomb island (about 100×100 nm) in the nanowire. The side gate was arranged at a distance of 150 nm from the Coulomb island. The starting metal Ti–Ge films had a resistance of 0.6–1 kΩ/□, which increased by 10–20% upon cooling the sample down to 4.2 K. Simultaneously with the evaporation of the step-crossing nanowires (lift-off technique), plain nanowires of the same sizes were deposited. This was done in order to separate the contributions to the structure resistance from the tunnel junctions themselves and from the nanowire with leads at room temperature. The junction resistance was varied from tens of kiloohms to hundreds of megaohms by selecting the thickness of the Ti and Ge layers, and its value strongly depended on temperature. The results reported in this paper were obtained for samples with a resistance of 50–300 kΩ at room temperature. Three samples of the 34 prepared exhibited periodic single-electron oscillations in the $I(U_G)$ functions of the gate voltage, which was reported in [7, 9]. This means that the resistance of each of the two tunnel junctions in these samples was $\gg h/e^2$. This

is a rather rare event because of random processes (thinning, oxidation, etc.) that participate in the formation of a tunnel junction and mesoscopic fluctuations of the junction resistance. In samples without single-electron oscillations, either one of the tunnel junctions was short-circuited or its resistance was less than h/e^2. To sufficient accuracy, the $I–V$ curve of such a sample is the characteristic of a single tunnel junction under the condition that the sample resistance is $\gg h/e^2$.

The dependence of the current on the source–drain voltage $I(U_{SD})$ for single tunnel junctions at $T = 4.2$ K was nonlinear at the applied voltages $|U_{SD}| \leq 40$ mV. The characteristics can be conventionally divided into two groups: high-symmetry (we will call them symmetric) and asymmetric (Fig. 2a, curves 1, 2, respectively). Symmetric $I–V$ curves predominantly occur in low-resistance junctions with resistance $R = (dI/dU_{SD})^{-1}\big|_{U_{SD} = 0} \leq 3$ MΩ at $T = 4.2$ K, whereas asymmetric characteristics are inherent in high-resistance junctions with $R \geq 10$ MΩ. The plots of the resistance as a function of temperature for junctions of both types mainly consist of regions described by the power law $R^{-1} \propto T^{4/3}$ (Fig. 2b). This law is typical for inelastic tunneling through chains containing pairs of localized states [6]. For this conduction mechanism, the $I–V$ curve of a tunnel junction is described by the function $I(U) \propto U^{7/3}$ [6] under the condition that the tunnel-junction area is sufficiently large, for which reason the contributions of separate channels are averaged. In experiments, one of the two branches of the $I–V$ curve (at $U_{SD} < 0$ or at $U_{SD} > 0$) is approximated well by a power function with an exponent close to 7/3; for example, curve 2 in Fig. 2a has an exponent of 2.01 at $U_{SD} < 0$, whereas the opposite branch corresponds to a more intricate dependence with a kink. With regard to the small area of a tunnel junction, which equals the product of the width of the Ti strip (100 nm) by the thickness of Ti on the step slope (≈ 3 nm), and the fixed density of localized states in a dielectric, it is unlikely that two localized states in a conducting chain are energetically close to each other. Hence, the condition $|E_i - E_j| > kT$, where E_i and E_j are the energies of localized states (the sources of localized states are the structural defects and interfaces), is most probable at the temperature $T = 4.2$ K. Under these conditions, tunneling with phonon emission, which is possible for only one of the applied voltage polarities, becomes more energetically profitable [10]. For the opposite polarity of the applied voltage, the growth of the current through a given two-impurity chain will be hindered. Therefore, it is likely that the conducting chain will change with increasing voltage, and, hence, a kink will appear in the $I–V$ curve [11]. The occurrence of symmetric $I–V$ curves (Fig. 2a, curve 1) is easily explained by the resistance $R_S(U_{SD}) =$ const connected in series with the junction: the tangents drawn from both ends of $I–V$ curve 1 in Fig. 2a are par-
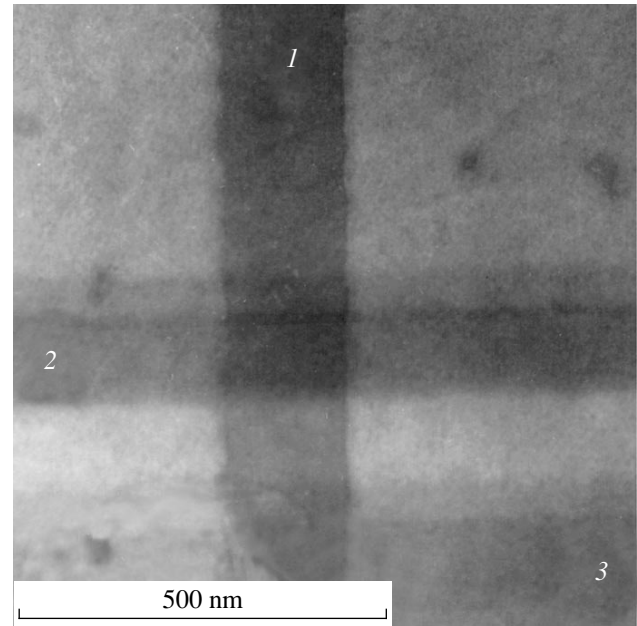
Fig. 1. Image of a single-electron transistor in a transmission electron microscope: (1) bulge at the Si_3N_4 surface, (2) Ti nanowire protected by a Ge layer, and (3) gate.

allel to each other ($R_S = 621$ kΩ at $T = 4.2$ K). The weakening of the $R(T)$ dependence with increasing temperature for junction 1 (Fig. 2b, curve 1) can be explained in the same way. Because $R(293 \text{ K}) \approx 100$ kΩ for junction 1, it is likely that the resistance R_S depends on temperature. The resistance of the transition region between the metal and the dielectric can serve as R_S, because the TiO_x crystal is a semiconductor with a bandgap of 0.1, 0.02, and 3 eV for $x = 1$, 1.5, and 2, respectively [12]. In our opinion, the weakening of the $R(T)$ dependence at $T \longrightarrow 4.2$ K (curves 1, 2 in Fig. 2b) is a consequence of the suppression of inelastic tunneling with decreasing temperature. Note that the gate functions $I(U_G)$ for two tunnel junctions whose volt–ampere characteristics are depicted in Fig. 2a exhibit a very weak dependence, and it may be assumed that $I(U_G) = $ const to within 10%. The experimental results described above suggest the conclusion that tunneling in the fabricated tunnel junctions is of an inelastic character.

In the samples with two tunnel junctions, the $I(U_{SD})$ and $I(U_G)$ curves (Fig. 3) differ significantly from the analogous curves obtained by modeling based on the orthodox theory of Coulomb blockade (inset in Fig. 3a, dashed lines in Fig. 3b). The source–drain $I–V$ curves corresponding to the polarization charges $Q_0 = 0$ and $Q_0 = e/2$ (Fig. 3a) do not cross each other at $U_{SD} = 11$ mV (the voltage determined by the specific set of parameters that ensures agreement between the model and experimental curves) as in the case of elastic tunneling (inset in Fig. 3a). The maxima in the drain–gate
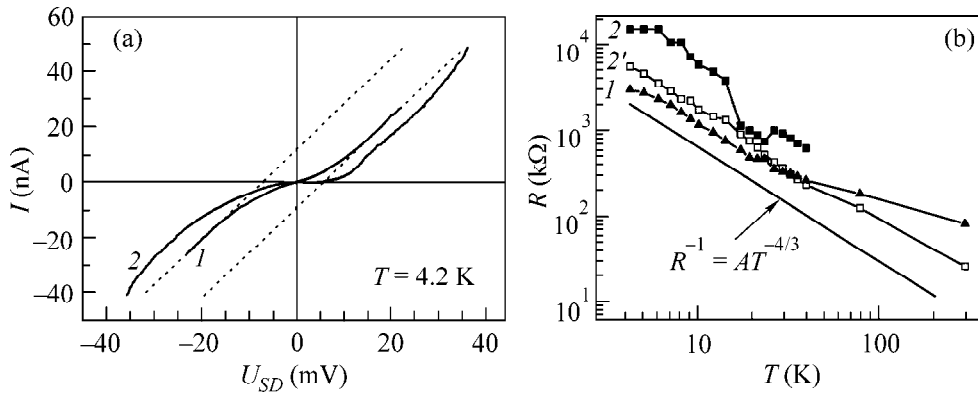
Fig. 2. (a) Two types of *I–V* curves occurring in single tunnel junctions demonstrated by the examples of junctions *1* and *2*. (b) Resistances of tunnel junctions *1* and *2* as functions of temperature (plots *2* and *2'* were recorded in succession and are displaced relative to each other as a result of switching).

current–voltage characteristics assume a sharpened shape (compare the dashed and solid curves in Fig. 3b). Single-electron oscillations in the current $I(U_G)$ are observed over a wide range of source–drain voltages U_{SD} without changing their phases by π at $U_{SD} = 11$ mV (Fig. 4).

Consider the effect of inelastic tunneling on Coulomb blockade. In the orthodox theory of Coulomb blockade [13], it is considered that an electron is thermalized after each act of tunneling. Therefore, the cases of elastic and inelastic tunneling in this theory are not distinguished. Note also that the presence of localized states inside the tunneling barrier does not affect the capacitance of the created structure and, hence, the energy characteristics of the single-electron transistor. An increase in the barrier penetrability with increasing applied voltage is the most significant consequence of inelastic tunneling that is exhibited in experiments. From here, it follows that the characteristics of a single-electron transistor under conditions of inelastic tunneling can be modeled within the orthodox theory by introducing U_{SD}-dependent resistances of tunnel junctions. Power laws $\langle G_n \rangle = \langle R_n^{-1} \rangle \propto U^{n-2/(n+1)}$, where n is the number of localized electronic states in the chain and U is the voltage applied across the junction, are typical of inelastic tunneling [6]. The current I in a single-electron transistor at a fixed U_{SD} is summed over several states of the Coulomb island, which are determined by the number of electrons on the island. Therefore, it is reasonable to use the gain in the electron energy ΔE upon tunneling through each state as eU. This method was previously used for single-electron transistors with nonlinear *I–V* curves of the tunnel junctions [14]. We described the junction resistances R_i ($i = 1, 2$)

by the function $R_i = R_{0i}/[1 + (\Delta E_i/\Delta E_{0i})^{\gamma_i}]$. Here, $\Delta E_i = 0$ if tunneling is energetically unprofitable. The two addends in the denominator reflect the two compo-

nents of the current through the junction: elastic and inelastic. The physical meaning of ΔE_{0i} is that the elastic channel dominates at voltages lower than $\Delta E_{0i}/e$ and the inelastic channel dominates at voltages higher than $\Delta E_{0i}/e$. The results of modeling are presented in Fig. 3 by solid lines and demonstrate a good agreement with experiment. The experimental curves in Fig. 4 cannot be modeled with the same high accuracy as those in Fig. 3b, because the $I(U_{SD})$ characteristics of the junctions in this sample exhibit strong mesoscopic distortions that are not described by a simple power law. The periods of single-electron oscillations in Figs. 3b and 4 differ by a factor of 1.5, probably because of the scatter in the lithographic width of the nanowires from 80 to 150 nm.

The phase of single-electron oscillations in the $I(U_G)$ plot in a conventional single-electron transistor differs by π on different sides of the crossing point of the two $I(U_{SD})$ current–voltage characteristics corresponding to the closed and open states of a single-electron transistor. The crossing of the *I–V* curves at $U_{SD} = 11$ mV (inset in Fig. 3a) is due to the fact that conduction proceeds through one of the two equally possible states of the Coulomb island in the open state and through two of the three possible states in the closed state of a single-electron transistor. As U_{SD} grows, the total number of states involved in the conduction process increases in both closed and open states of a single-electron transistor; therefore, the difference between one state and another becomes less and less significant, and single-electron current oscillations are damped. The voltage dependence of the tunnel junction resistance results in narrowing of the distribution of the probability p_n for n excessive electrons to exist on the Coulomb island. Thus, in the closed state of a single-electron transistor for $U_{SD} = 11$ mV and for the other parameters indicated in the caption to Fig. 3, the probabilities of the states $n = -1, 0$, and 1 in the case of $R_1 =$
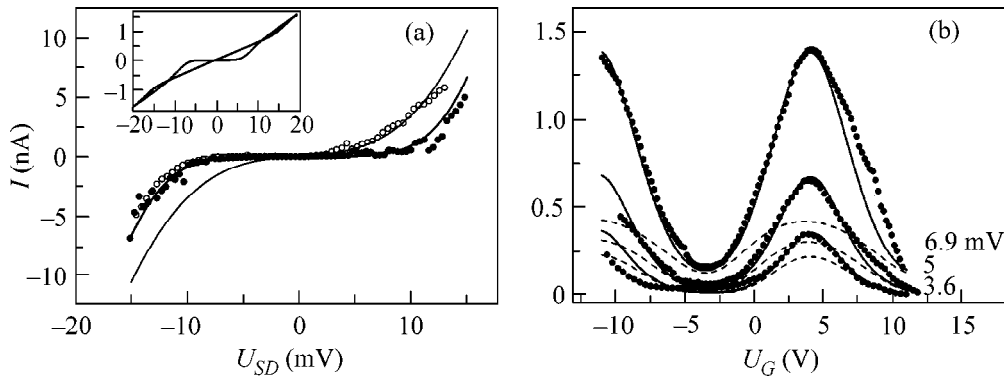
Fig. 3. Experimental (points) and calculated (solid lines) *I–V* curves of a single-electron transistor under conditions of inelastic tunneling with parameters $T = 4.2$ K, $R_{01} = 5$ MΩ, $R_{02} = 3.3$ MΩ, $C_1 = C_2 = 11$ aF, $C_g = 0.0105$ aF, $\Delta E_{01} = \Delta E_{02} = 2.3$ meV, and $\gamma_1 = \gamma_2 = 2$. (a) Source–drain characteristics; occasional switching of the polarization charge from $Q_0 = 0$ to $Q_0 = e/2$ occurred for the experimental volt–ampere characteristic (white points) at $U_{SD} > 0$; model curves are presented for $Q_0 = 0$ and $Q_0 = e/2$. (b) Gate characteristics; source–drain voltages are shown in the figure, and $Q_0 = -0.21e$. Model *I–V* curves of a single-electron transistor with elastic tunneling (R_1, R_2 = const) are shown in the inset in Fig. 2a and in dashed lines in Fig. 2b at the same parameters.

R_2 = const are 1/7, 5/7, and 1/7, respectively. In the case of $R_1 = R_2 = R(\Delta E)$, these probabilities are 1/50, 48/50, and 1/50, respectively. It is evident that one state, $n = 0$, plays the main role in the latter case, and the addition of the second current channel (through the state $n = -1$ or $n = 1$) is insignificant. Therefore, the intersection of the $I(U_{SD})$ curves measured at various U_G disappears at $U_{SD} = 11$ mV, and the phase of single-electron oscillations in the $I(U_G)$ plot becomes independent of U_{SD}. In addition, the narrowing of the distribution p_n prevents equalization of the currents through the open and closed states of a single-electron transistor upon U_{SD} growth due to an increase in the total number of current channels (n) in each of the two states of a single-elec-

tron transistor. This fact leads to deeper penetration of single-electron oscillations into the region of high U_{SD}.

Thus, inelastic tunneling qualitatively changes the manifestation of Coulomb blockade in a single-electron transistor under the condition that the resistances of both tunnel junctions are close to each other ($R_{01} \approx R_{02}$). The region of the occurrence of single-electron oscillations extends several times in the source–drain voltage, and the oscillations change their shape. Any other nonlinearities of tunnel junctions, for example, nonlinearities due to the low height of the tunneling barrier, will lead to the same result if they provide a significant increase in the current through the junction at voltages of about a half-width of the Coulomb gap.
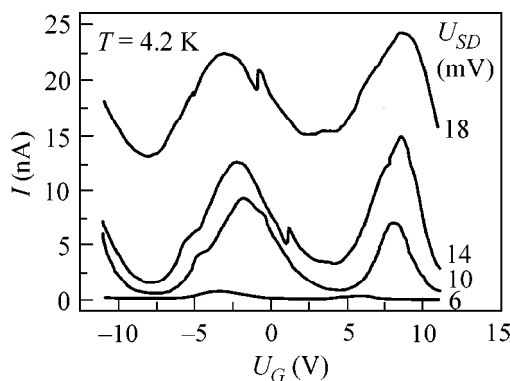
Fig. 4. single-electron oscillations in experimental $I(U_G)$ plots depicted over a wide range of source–drain voltages. The junction capacitances determined from the size of the Coulomb gap in the $I(U_{SD})$ plots are $C_1 = C_2 = 10$ aF [7].

REFERENCES

1. D. V. Averin and K. K. Likharev, Zh. Éksp. Teor. Fiz. **90**, 733 (1986) [Sov. Phys. JETP **63**, 427 (1986)].

2. L. S. Kuz'min and K. K. Likharev, Pis'ma Zh. Éksp. Teor. Fiz. **45**, 389 (1987) [JETP Lett. **45**, 495 (1987)].

3. T. A. Fulton and G. J. Dolan, Phys. Rev. Lett. **59**, 109 (1987).

4. K. K. Likharev, NATO ASI Ser., Ser. B **251**, 371 (1991).

5. M. Naito and M. R. Beasley, Phys. Rev. B **35**, 2548 (1987).

6. L. I. Glazman and K. A. Matveev, Zh. Éksp. Teor. Fiz. **94**, 332 (1988) [Sov. Phys. JETP **67**, 1276 (1988)].

7. L. V. Litvin, V. A. Kolosanov, K. P. Mogil'nikov, *et al.*, Mikroélektronika **29**, 189 (2000).

8. S. Altmeyer, B. Spangenberg, and H. Kurz, Appl. Phys. Lett. **67**, 569 (1995).

9. Z. D. Kvon, L. V. Litvin, V. A. Tkachenko, and A. L. Aseev, Usp. Fiz. Nauk **169**, 471 (1999).

10. B. I. Shklovskiĭ, Fiz. Tekh. Poluprovodn. (Leningrad) **10**, 1440 (1976) [Sov. Phys. Semicond. **10**, 855 (1976)].

11. A. O. Orlov and A. K. Savchenko, Pis'ma Zh. Éksp. Teor. Fiz. **47**, 393 (1988) [JETP Lett. **47**, 470 (1988)].

12. *Physical Constants: Handbook*, Ed. by I. S. Grigor'ev and E. Z. Meilikhova (Énergoizdat, Moscow, 1991).

13. K. K. Likharev, IBM J. Res. Dev. **32**, 144 (1988).

14. A. N. Korotkov and Yu. V. Nazarov, Physica B (Amsterdam) **173**, 217 (1991).

Translated by A. Bagatur'yants

Orbits in Large Aluminum Clusters: Five-Pointed Stars

G. V. Shpatakovskaya

Institute of Mathematical Modeling, Russian Academy of Sciences, Miusskaya pl. 4a, Moscow, 125047 Russia
e-mail: shpat@imamod.ru
Received August 2, 2000

The distinctions in the mass spectra of large sodium Na_N and aluminum Al_N clusters are discussed. A semiclassical method is used to describe the shell effects within a spherical jellium model. It allows one to analyze the relative role of different classical trajectories in the formation of electronic supershells in clusters of various sizes at zero and finite temperatures. A criterion for the hardness of the self-consistent potential is formulated. The conjecture that the five-point-star trajectories make the main contribution to the spectral oscillations for large soft-potential Al_N ($250 < N < 900$) clusters is substantiated. The computational results are in agreement with the mass spectra of the Al_N clusters at $T \simeq 300$ K. © *2000 MAIK "Nauka/Interperiodica".*

PACS numbers: 71.24.+q

1. The oscillations in the mass spectra of metal clusters may be caused by both the shell structure of electronic spectra and the positioning of ions in lattice sites [1]. Experiments show that the oscillations in the mass spectra of large aluminum Al_N [2–4] and sodium Na_N [5] clusters (N is the number of atoms in a cluster) differ significantly in shape. Whereas the oscillations for sodium proceed with beats, the aluminum clusters with $N > 250$ exhibit sinusoidal behavior with a frequency approximately twice that for sodium. The spectra of the Al_N clusters of smaller sizes represent an intricate pattern without any distinct period. In the literature, the cause of this distinction is discussed in terms of classical trajectories of electron motion in a self-consistent potential (the number of electrons in a cluster is $N_e = wN$, where w is the valence of a metal).

In [3], an attempt was undertaken to explain the experiment by invoking a spherical jellium model and the quasiclassical theory [6–9]. It was conjectured that, contrary to a hard potential of Na_N clusters, in which a triangular trajectory and a square trajectory of a close frequency dominate (the oscillations with beats result from the interference of the relevant contributions), in a soft potential of Al_N clusters with $250 < N < 900$, the main contribution comes from a single trajectory shaped like a five-pointed star. According to this theory, the clusters of larger size should have triangular and, later, square trajectories (this is confirmed by the self-consistent computation [2] of the density of states for $N_e = 4940$), leading to a change in the oscillation frequency.

An alternative explanation was suggested in [4], where the mass spectra of "cold" ($T = 100$ K) Al_N clusters were experimentally measured and analyzed over a very wide range of N values ($250 < N < 10000$). An analysis of the spectra showed that the oscillation max-

ima, numbered sequentially by the index k ($k > 25$), appeared with a constant frequency over the entire range studied and fitted the law $N \simeq 0.0104k^3$, which is readily explained by the atomic positioning in an octahedral lattice. Accordingly, the cluster shape is not a sphere but an octahedron, so that the shell filling corresponds to the assembling of one of its faces. Evidently, the spherical jellium model with uniformly distributed ions inside the sphere is not adequate in this case.

In [10], the assumption about the dominant contribution from a five-point-star orbit in the aluminum clusters was ruled out by the quantum-mechanical calculation of the density of states for $N_e = 1000$ electrons in the Saxon–Woods potential.

Nevertheless, the positions of the maxima observed in [2] for $250 < N < 430$ at $T = 295$ K agree well with the results of self-consistent calculations carried out in the same work with the jellium model, while the comparison of the mass spectra of Al_N observed at $T = 110$ K and $T = 295$ K for $N < 250$ reveals that the temperature has an appreciable effect on the shapes of the corresponding curves, indicating that the lattice melts upon temperature elevation and manifesting the electronic shell structure.

Therefore, although the contribution of the ion lattice to the oscillations in mass spectra likely dominates in aluminum at low temperatures and, hence, the spherical jellium model is inadequate in this temperature range, the role of the lattice diminishes with increasing temperature, rendering the jellium model more applicable. It is assumed in this work that the electronic structure reveals itself upon melting the lattice of "hot" clusters and that the melting temperature can be experimentally determined from the changes in the mass spectra at $N \sim 1000$. However, whereas the jellium calculations were carried out for sodium clusters over a wide range

of N values and for different temperatures [11], the respective calculations for aluminum are still lacking.

In this work, this gap is filled by studying the dependence of the oscillating part of the electronic free energy of an aluminum cluster on its size and temperature, and the assumption about the dominant role of a five-point-star orbit in the oscillations of Al_N spectra at $T \simeq 300$ K is confirmed for the N numbers experimentally observed in [3].

2. The semiclassical approach [12, 13] used in this work is based on the spherical jellium model and the extended Thomas–Fermi (ETF; see references in [14]) model, whose solution, namely, the electron density $n(r)$, the chemical potential μ, the self-consistent potential $U(r)$, and the corresponding electronic free energy $F(N_e, T)$, are assumed to be known. The ETF model well describes the average characteristics of a system, while the shell effects of interest will be studied using the following expression for the correction to the free energy (in atomic units) [13, 15]:

$$\Delta F_{sh} = -\int_{-\infty}^{\mu} d\mu' \frac{\hat{X}_{\mu'}(T)}{\sinh(\hat{X}_{\mu'}(T))} \Delta N_{sh}(\mu', 0). \quad (1)$$

Here, the operator $\hat{X}_\mu(T) = -i\pi T\partial/\partial\mu$ and $\Delta N_{sh}(\mu, 0)$ is the shell correction to the number of states with energies below μ without regard for explicit temperature dependence. In the semiclassical approximation

$$\Delta N_{sh}(\mu, 0) = \Delta N_{sh}(\mu)$$
$$= \frac{2}{\pi} {\sum_{k,s}}' \frac{(-1)^{k+s}}{k} \int_0^{\lambda_\mu} d\lambda\, \lambda \sin[2\pi(k\nu_\mu(\lambda) + s\lambda)], \quad (2)$$

where summation over k and s goes from $-\infty$ to $+\infty$; the prime over the sum sign indicates that the nonoscillating term with $k = s = 0$ is omitted; $S_{\mu\lambda} = \pi\nu_\mu(\lambda)$ is the radial action between the turning points of the electron motion with energy μ and orbital angular momentum λ in the potential $U(r)$; $\lambda_\mu = p_\mu(r_0)r_0$ is the maximum orbital angular momentum for energy μ; r_0 is the point at which the $p_\mu(r)r$ function is maximum; and $p_\mu(r) = \sqrt{2(\mu - U(r))}$.

In the semiclassical theory, the integral in Eq. (2) is calculated by the saddle-point method and the sum of contributions from the saddle points $\bar{\lambda}_j$ has the form

$$\Delta N_{sh}(\mu) = \sum_j \frac{2\bar{\lambda}_j}{\pi\sqrt{\nu_\mu''(\bar{\lambda}_j)}}$$
$$\times {\sum_{k,s}}' \frac{\sin[2\pi(k\nu_\mu(\bar{\lambda}_j) + s\bar{\lambda}_j) - \pi(k+s) + \pi/4]}{k^{3/2}}. \quad (3)$$

Here, $\nu_\mu''(\bar{\lambda}_j) = \partial^2\nu_\mu(\lambda)/\partial\lambda^2|_{\bar{\lambda}_j}$ and the $\bar{\lambda}_j$ value is determined from the relationship

$$\nu_\mu'(\bar{\lambda}_j) = \left.\frac{\partial\nu_\mu(\lambda)}{\partial\lambda}\right|_{\bar{\lambda}_j} = -\frac{s}{k}, \quad 0 \le \bar{\lambda}_j \le \lambda_\mu. \quad (4)$$

The prime at the sum sign in Eq. (3) indicates that only the leading terms are taken into account in the sums over s and k.

Differentiation of Eq. (3) with respect to μ gives the shell correction to the density of states,[1]

$$\Delta\rho_{sh}(\mu) = \sum_j \frac{4t_\mu(\bar{\lambda}_j)\bar{\lambda}_j}{\pi\sqrt{\nu_\mu''(\bar{\lambda}_j)}}$$
$$\times {\sum_{k,s}}' \frac{\cos[2\pi(k\nu_\mu(\bar{\lambda}_j) + s\bar{\lambda}_j) - \pi(k+s) + \pi/4]}{\sqrt{k}}, \quad (5)$$

while integration in Eq. (1) yields the shell correction to the free energy,

$$\Delta F_{sh}(\mu) = \sum_j \frac{\bar{\lambda}_j}{\pi t_\mu(\bar{\lambda}_j)\sqrt{\nu_\mu''(\bar{\lambda}_j)}} {\sum_{k,s}}' \frac{X_k^j(T)}{\sinh[X_k^j(T)]}$$
$$\times \frac{\cos\left[2\pi(k\nu_\mu(\bar{\lambda}_j) + s\bar{\lambda}_j) - \pi(k+s) + \dfrac{\pi}{4}\right]}{k^{5/2}}. \quad (6)$$

The following notations are introduced in these expressions:

$$X_k^j(T) = 2\pi k T t_\mu(\lambda_j), \quad t_\mu(\bar{\lambda}_j) = \left.\pi\frac{\partial\nu_\mu(\lambda)}{\partial\mu}\right|_{\bar{\lambda}_j}.$$

The derivative on the left-hand side of Eq. (4) is equal to the ratio of the frequencies of the angular and radial motions of a particle with energy μ and orbital angular momentum $\bar{\lambda}_j$ [16]. The requirement that this frequency ratio be a ratio of integers is the condition for closure of the trajectory of this motion.

Equation (5) exactly coincides with the result obtained for the central potential in [17], where it was derived by using the semiclassical approximation for the Green's function. The combination of the semiclassical approach and Eq. (1) for the correction to the free energy results in a simple expression for the directly measurable quantities [Eq. (6)]. It turns out that only those electron trajectories whose energies are equal to the chemical potential of the system should be taken into account, while the condition (4) and Eq. (1), respectively, allow one to select the main trajectories and correctly include the temperature effect.

Note that the analytical approach presented in this work is much simpler and more pictorial, especially for large complexes, than the Strutinsky method of shell

---

[1] In the semiclassical approximation, only the rapidly varying function sin[…] should be differentiated.

correction, which was applied to clusters in [14] and used earlier in nuclear physics [18, 19] and which is also based on the ETF model.

3. For a fixed saddle point $\bar{\lambda}_j$, the leading contribution to the sums over k and s in Eq. (3) comes from the minimum values $k = \bar{k}_j$ and $s = \bar{s}_j$ that form the fraction $\bar{s}_j / \bar{k}_j$ in Eq. (4). Let us refer to the corresponding smallest length trajectory as the jth orbit; then the $\pi \nu_\mu(\bar{\lambda}_j)$ and $t_\mu(\bar{\lambda}_j)$ quantities have the meaning, respectively, of the radial action and the time of electron movement between the turning points along the jth orbit. Multiplying the numerator and denominator in $\bar{s}_j / \bar{k}_j$ by an integer $m = 1, 2, 3, \ldots$, one obtains the trajectories with m periods for the movement along the jth orbit. One can thus replace the primed sum over s and k in Eqs. (3), (5), and (6) by the sum over m: $\sum'_{k,s} \ldots = \sum_{m=1}^{\infty} \ldots$, where $k = \bar{k}_j m$ and $s = \bar{s}_j m$.

For attractive potentials that are finite at the zero coordinate, the derivative $\nu'_\mu(0) = -1/2$ [20]. For hard self-consistent potentials, the derivative monotonically increases with λ from $-1/2$ to $\nu'_\mu(\lambda_\mu)$ for any number of particles. For soft potentials, the situation depends on the system size; in small clusters, this derivative may decrease or be a nonmonotonic function with a minimum, while in large clusters it is an increasing function. Consequently, the sign of the second derivative $\nu''_\mu(0)$ at the zero coordinate may serve as a criterion for the potential's hardness: $\nu''_\mu(0) > 0$ for a hard potential for any cluster size.

The difference between the hard and soft potentials is illustrated in Fig. 1, where the behavior of the $\nu'_\mu(\lambda)$ derivative is demonstrated for sodium and aluminum clusters containing different numbers of electrons N_e. The chemical and self-consistent ETF potentials were approximated by the Saxon–Woods model potential[2]

$$U(r) = -V_0[1 + e^{(r-R)/a}]^{-1}, \quad R = r_s N_e^{1/3}, \quad (7)$$

with the parameters of the aluminum ($V_0 = 0.5319$, $a = 2.7$, $r_s = r_s^b = 2.07$, and $\mu = -0.1053$) and sodium ($V_0 = 0.22$, $a = 1.4$, $r_s = r_s^b = 3.93$, and $\mu = -0.1015$) clusters taken from [3].

Let us consider sufficiently large aluminum clusters with $N_e > 250$, for which the $\nu'_\mu(\lambda)$ derivative monotonically increases with λ (Fig. 1). This implies that the
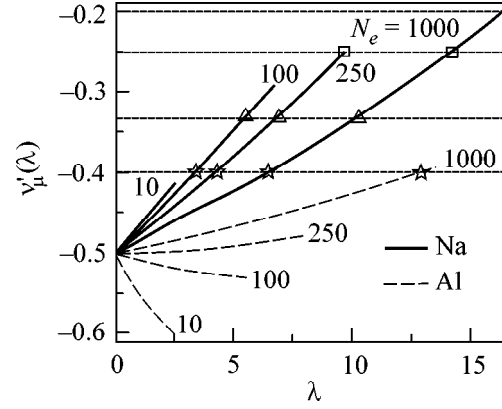

Fig. 1. Derivative $\nu'_\mu(\lambda)$ of the radial action with respect to the orbital angular momentum λ for hard (Na) and soft (Al) potentials and different numbers of particles in the cluster. Calculated using potential (7) with parameters taken from [3].

rational fractions s/k satisfying condition (4) lie in the range

$$-\nu'_\mu(\lambda_\mu) \leq \frac{s}{k} = \frac{\bar{s}_j m}{\bar{k}_j m} \leq \frac{1}{2}. \quad (8)$$

It then immediately follows that $\bar{s}_j \geq 1$ and $\bar{k}_j \geq 2$. The fractions with $\bar{s}_j = 1$ (1/2, 1/3, 1/4, …) correspond to linear, triangular, square, etc. orbits. The fractions of the type $n/(2n + 1)$, with $n = 2, 3, 4, \ldots$, lie between 1/3 and 1/2 and correspond to $(2n + 1)$-pointed stars.

The solution $\bar{s}_j / \bar{k}_j = 1/2$ always exists and corresponds to an electron moving with zero orbital angular momentum $\bar{\lambda}_0 = 0$ along a linear orbit through the center. The corresponding contribution is small for large clusters (see [12, 13]). A circular orbit with radius r_0 and maximum orbital angular momentum λ_μ [the contribution from the upper limit of integration in Eq. (2)] is also unimportant in this case.

One can see in Fig. 1 that, for a hard sodium potential, there is a contribution from the triangular orbit ($\bar{s}_j = 1$, $\bar{k}_j = 3$) in a cluster with $N_e = 100$ and, in addition, from the square ($\bar{s}_j = 1$, $\bar{k}_j = 4$) and pentagonal ($\bar{s}_j = 1$, $\bar{k}_j = 5$) trajectories in a cluster with $N_e = 1000$. On this background, the contribution from the five-pointed star $\bar{s}_j / \bar{k}_j = 2/5$ to Eq. (6) is small due to the $\bar{\lambda}_j / \bar{k}_j^{5/2}$ factor.[3]

A completely different situation occurs for aluminum (Fig. 1). Because of the weak λ dependence of the derivative in a soft potential, the triangular orbit appears only in very large clusters with $N_e \sim 3000$,

---

[2] The difference between potential (7) and the self-consistent ETF potential is discussed in [9].

[3] This is the reason why these secondary trajectories were not discussed in [12, 13], where only hard potentials were considered.
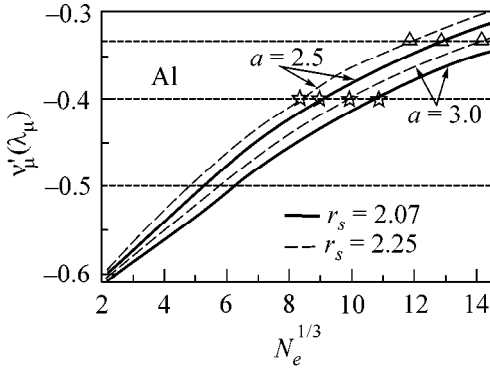
Fig. 2. Plots of the derivative $v'_\mu (\lambda_\mu)$ of radial action at the maximum orbital angular momentum vs. aluminum cluster size $N_e^{1/3}$, as calculated using potential (7) with different parameters r_s and a.
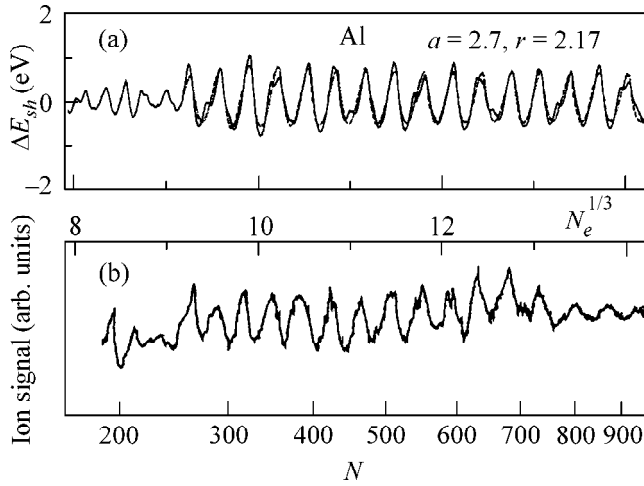

Fig. 3. (a) Shell correction to the total electronic energy of the aluminum cluster at $T = 0$ vs. cluster size $N_e^{1/3}$, as calculated by Eq. (6) without taking into account the triangular trajectory. (b) Oscillations in the ion signal in the mass spectra of Al$_N$ clusters [3].

while the smaller clusters, e.g., with $N_e = 1000$, are dominated by an orbit shaped like a five-pointed star. However, it is seen from a comparison of Eqs. (5) and (6) that the dominance of this orbit in Eq. (5) for the correction to the density of states is not as apparent as in Eq. (6); the calculations show that the oscillation amplitudes for the five-pointed and seven-pointed stars differ in Eq. (5) by only a factor of 1.36, whereas the contribution from the five-pointed star in Eq. (6) is 3.3 times greater than that from the seven-pointed star. Because of this, it is difficult to distinguish a well-defined period near the Fermi surface when considering the sum over trajectories in Eq. (5) as a function of μ at a fixed $N_e = 1000$. This might be the reason why the conclusions drawn in [10] were negative.

4. It is seen from Eq. (8) and Fig. 1 that the cluster sizes N_e^j for which new saddle points $\bar\lambda_j$ arise can be estimated from the condition $v'_\mu (\lambda_\mu; N_e^j) = -\bar{s}_j/\bar{k}_j$. To do this, it is sufficient to know the dependence of $v'_\mu (\lambda_\mu)$ on the cluster size N_e. The relevant function calculated for aluminum by the formula $v'_\mu (\lambda_\mu) = [3 + U''(r_0) r_0^2 / p_\mu^2 (r_0)]^{-1/2}$ [13] is shown in Fig. 2 for various values of parameters r_s and a. One can see in Fig. 2 that a decrease in r_s is equivalent to an increase in a, i.e., to the softening of the potential.

Self-consistent calculations suggest [9] that r_s depends weakly on N_e. Hence, as N_e increases, the curves corresponding to large r_s should gradually transform into a curve corresponding to the radius $r_s = r_s^b$ of the Wigner–Zeits cell in bulk metal. To account for this effect, the calculations were carried out first for the shell correction (6) to the total electronic energy of Al$_N$ at $T = 0$ using potential (7) with $r_s = 2.17 > r_s^b$. Figure 3 presents (a) the results of calculations without inclusion of the triangular trajectories and (b) the measured oscillations in the mass spectra of aluminum clusters. The dashed line in the calculated curve (Fig. 3a) indicates the contribution from the five-point-star trajectory. It dominates at $N_e > 250$ ($N_e^{1/3} > 9.1$), while the contributions from other star-shaped trajectories are small in this mass range. The cosine argument for the five-point-star trajectory depends linearly on $N_e^{1/3}$:

$$5v_\mu(\bar\lambda_*) + 2\bar\lambda_* = -2.75317 + 3.1487 N_e^{1/3}, \quad (9)$$

resulting in a periodic dependence on this variable. At $N_e > 250$, curve (a) fits curve (b) well, both structurally and in period. Note also that the chaotic portions of the calculated and experimental spectra exhibit similar behavior at $N_e < 250$ (calculations show that it is caused by the contributions from the star-shaped trajectories with $\bar{s}_j/\bar{k}_j = 3/7, 4/9, 5/11,$ and $6/13$).

A triangular trajectory with $r_s = 2.17$ is expected to appear at $N_e^\Delta = 2450$ ($N_e^{1/3} \simeq 13.5$). Since the corresponding oscillation amplitude is ~3.3 eV, this trajectory immediately becomes dominant; it oscillates with almost halved frequency. The relevant term in the cosine argument depends linearly on $N_e^{1/3}$: $3v_\mu(\bar\lambda_\Delta) + \bar\lambda_\Delta = -3.2568 + 1.7605 N_e^{1/3}$. However, when considering the above-mentioned $r_s(N_e)$ dependence, one should use a smaller r_s value for the self-consistent potential in approximation (7) in this range of N_e values. This is indirectly confirmed by a small (although distinguishable in Fig. 3b) change in the frequency of

experimental oscillations at $N_e^{1/3} > 13$. We note parenthetically that the frequency would not change if the spectrum were determined by the ion lattice.

Setting $r_s = r_s^b = 2.07$, one obtains for the five-pointed star the $5\nu_\mu(\bar{\lambda}_*) + 2\bar{\lambda}_* = -2.9435 + 3.0249\,N_e^{1/3}$ dependence instead of Eq. (9); i.e., the period indeed increases slightly. The N_e^Δ value for this r_s value is equal to 2750 ($N_e^{1/3} \geq 14$), and the spectra should be rearranged at $N > 900$.

To estimate the temperature-induced decay of the electronic shell oscillations, the temperature multiplier in Eq. (6) should be evaluated for the five-pointed star. The calculations show that the characteristic reciprocal temperature $2\pi\bar{k}_j\,t_\mu(\lambda_j)$ increases for this orbit from 900 to 1350 upon increasing N_e from 750 to 3000. It follows that the temperature multiplier differs (for $m = 1$) only slightly from unity at $T = 300$ K $\simeq 0.001$ au and decreases, respectively, from 0.88 to 0.75. For the triangular trajectory, the characteristic reciprocal temperature is on the order of 600 at $N_e \sim 3000$ and the corresponding multiplier is 0.95. Therefore, if the lattice is molten at $T = 300$ K, the oscillations due to electronic shells should manifest themselves in full measure.

REFERENCES

1. T. P. Martin, T. Bergmann, H. Göhlich, and T. Lange, Chem. Phys. Lett. **172**, 209 (1990).

2. J. L. Persson, R. L. Whetten, H. P. Cheng, and R. S. Berry, Chem. Phys. Lett. **186**, 215 (1991).

3. J. Lermé, M. Pellarin, J. L. Vialle, *et al.*, Phys. Rev. Lett. **68**, 2818 (1992).

4. T. P. Martin, U. Näher, and H. Schaber, Chem. Phys. Lett. **199**, 470 (1992).

5. J. Pederson, S. Bjørnholm, J. Borggreen, *et al.*, Nature **353**, 733 (1991).

6. M. C. Guitzwiller, J. Math. Phys. **8**, 1979 (1967); **10**, 1004 (1969); **12**, 343 (1971).

7. R. Balian and C. Bloch, Ann. Phys. **69**, 76 (1972).

8. M. V. Berry and M. Tabor, Proc. R. Soc. London, Ser. A **349**, 101 (1976); **356**, 375 (1977).

9. H. Nishioka, K. Hansen, and B. R. Mottelson, Phys. Rev. B **42**, 9377 (1990).

10. J. Mansikka-aho, M. Manninen, and H. Nishioka, Phys. Rev. B **48**, 1837 (1993).

11. O. Genzken and M. Brack, Phys. Rev. Lett. **67**, 3286 (1991).

12. G. V. Shpatakovskaya, Pis'ma Zh. Éksp. Teor. Fiz. **70**, 333 (1999) [JETP Lett. **70**, 334 (1999)]; cond-mat/0001116.

13. G. V. Shpatakovskaya, Zh. Éksp. Teor. Fiz. **118**, 87 (2000) [JETP **91**, 76 (2000)].

14. C. Yannouleas and Uzi Landman, Phys. Rev. B **48**, 8376 (1993).

15. D. A. Kirzhnits, Yu. E. Lozovik, and G. V. Shpatakovskaya, Usp. Fiz. Nauk **111**, 3 (1975) [Sov. Phys. Usp. **16**, 587 (1975)].

16. L. D. Landau and E. M. Lifshitz, *Course of Theoretical Physics*, Vol. 1: *Mechanics* (Nauka, Moscow, 1982; Pergamon, New York, 1988).

17. M. C. Guitzwiller, J. Math. Phys. **11**, 1791 (1970).

18. C. Guet and M. Brack, Z. Phys. A **297**, 247 (1980).

19. M. Brack and P. Quentin, Nucl. Phys. A **361**, 35 (1981).

20. D. A. Kirzhnits and G. V. Shpatakovskaya, Zh. Éksp. Teor. Fiz. **62**, 2082 (1972) [Sov. Phys. JETP **35**, 1088 (1972)].

Translated by V. Sakun

The Conductivity of the Spin-Polarized Two-Dimensional Electron Gas: Exchange/Correlation and Strong Disorder Effects[1]

A. Gold

Centre d'Elaboration de Matériaux et d'Etudes Structurales, CNRS, 31055 Toulouse, France
Received August 3, 2000

The conductivity of a spin-polarized two-dimensional electron gas is calculated and compared with the conductivity of the unpolarized electron gas. Disorder effects are considered within the self-consistent current relaxation theory, which gives rise to a crossover point from metallic to insulating behavior. Many-body effects due to exchange and correlation are taken into account and are described by a local-field correction. Our calculations are in good agreement with recent experimental results on the magnetoresistance of silicon inversion layers. © 2000 MAIK "Nauka/Interperiodica".

PACS numbers: 73.50.–h; 71.30.+h

In recent experiments, the transport properties of a two-dimensional electron gas (2DEG), as realized in Si inversion layers and GaAs heterostructures, have been studied by applying a parallel magnetic field [1–13]. The term "parallel magnetic field" means that the magnetic field is in the plane of the electron gas. The renewed interest in the metal–insulator transition (MIT) [14–19] in a 2DEG initiated much interest in transport measurements. In the metallic phase, a strong positive magnetoresistance was found. The experimental fact that the magnetoresistance saturates above the magnetic field B_c, corresponding to a totally polarized electron system, was interpreted as a manifestation of the importance of spin polarization [8, 9].

In a recent paper [20], we compared the transport properties of an unpolarized and a polarized 2DEG and found a positive magnetoresistance. Our calculation was made for weak disorder, and the screening behavior was treated within the random phase approximation. The random phase approximation is valid if the Wigner–Seitz parameter $r_s = (\pi N a^{*2})^{-1/2}$ is small, which is not the case in the experiments; $a^* = 22.9$ Å is the effective Bohr radius, defined with the effective mass m^* and the background dielectric constant ϵ_L, and N is the electron density. Moreover, at a low electron density, the disorder effects in Si inversion layers are large, because the MIT takes place around $N = N_c \approx 1 \times 10^{11}$ cm^{-2} ($r_s = 7.8$). For a relatively high density $N > 2N_c$, our theory was in fair agreement with experimental results [8, 9].

Very recent experiments [10, 13] concerning the magnetoresistance showed that our theory [20] failed to describe experiments for $N < 2N_c$. Therefore, in this paper, we take into account exchange correlation

effects, which are important for large r_s, and we consider multiple scattering effects, which lead to a MIT at low carrier density.

We assume that the 2DEG electron gas has zero width in the direction perpendicular to the interface and consider only charged impurity scattering. Screening effects are taken into account within the random phase approximation and include exchange/correlation effects (many-body effects) described by the local-field correction (LFC) [21]. Such a theory is also valid in the dilute limit where r_s is large. Multiple scattering effects are treated within the self-consistent current relaxation theory [22–26]. In this paper we apply the transport theory for an interacting electron gas in two dimensions [22, 26] and screening effects, including exchange and correlation, are taken into account by using an analytical expression for the LFC [27].

The electron density defines the Fermi wave number k_F of the 2DEG via $N = g_s g_v k_F^2 / 2\pi$. Here, g_v and g_s are the valley and the spin degeneracy factors, respectively. For Si inversion layers and Si quantum wells, we use $g_v = 2$. For zero field, the spin degeneracy is $g_s = 2$, while for large magnetic fields the degeneracy factor is given by $g_s = 1$. We assume that the disorder is due to charged impurities of density N_i located in the plane of the electron gas and the random potential for wave number q is given by $\langle |U(q)|^2 \rangle = N_i (2\pi e^2 / \epsilon_L q)^2$ [28]. A magnetic field applied parallel to the 2DEG plane leads to a Zeeman energy $\Delta E = \pm g^* \mu_B B / 2$; g^* is the effective Landé g factor. The system is totally spin polarized if ΔE is larger than the Fermi energy ϵ_F. This condition defines a critical magnetic field B_c for complete spin polarization, which is given by $B_c = 2\epsilon_F / g^* \mu_B$. In the following, we discuss the conductivity for the unpolar-

---

[1] This article was submitted by the author in English.

ized electron gas ($B = 0$) and for the fully polarized electron gas ($B \geq B_c$).

The LFC $G(q)$ for wave number q takes into account corrections to the random-phase approximation due to exchange and correlations. The LFC is important for small distances and for small electron densities [29]. We use theory [27], where the LFC is written in a Hubbard form with three coefficients $C_i(r_s)$, which are calculated self-consistently by using the Singwi–Tosi–Land–Sjölander approach [21]: $G(q) = 1.402 r_s^{2/3} q/[2.644 q_0^2 C_1(r_s)^2 + q^2(C_2(r_s)^2 - qq_0 C_3(r_3)]^{1/2}$ with $q_0 = 2/r_s^{2/3} a^*$. The LFC reduces the screening properties of an electron gas compared to the random phase approximation—the Coulomb interaction potential $V(q) = 2\pi e^2/q$ in the screening function is replaced by $[1 - G(q)]V(q)$.

In the self-consistent current relaxation theory [23], the dynamical conductivity is expressed in terms of the current relaxation kernel. The current relaxation kernel represents a generalized inverse scattering time. The current modes decay into density modes, and the current relaxation kernel is expressed by the golden rule expression with the squared coupling matrix element $qU(q)$ (the gradient of the random potential) and the density of final states (the density correlation function). The density correlation function depends on the current relaxation kernel, and this gives rise to a self-consistent theory for the conductivity of the 2DEG. For details, we refer the reader to [22]. We note that mobility measurements of the 2DEG in strongly disordered remote doped GaAs/Al$_x$Ga$_{1-x}$As heterostructures have successfully been described by our theory [25, 26].

In our approach, quantum interference effects for noninteracting electrons [30], which lead to weak localization effects, are ignored. We have argued before that the "relevance of interference effects for the strongly disordered *interacting* 2DEG is not understood" [22]. We claim that the recent measurements [17] of the temperature-dependent conductivity of Si inversion layers near the MIT reinforce our argument.

In the transport theory [22] for the strongly disordered 2DEG with Coulomb interaction effects, the conductivity σ at zero temperature is given by [24, 26]

$$\sigma = \sigma_0(1 - A), \qquad (1a)$$

where $\sigma_0 = Ne^2\tau_0/m^*$ and τ_0 is the scattering time at zero temperature calculated in the Born approximation [28]; $1/\tau_0$ is proportional to the impurity density N_i and is expressed by [22]

$$\frac{1}{\tau_0} = \frac{1}{4\pi m^* N} \int_0^\infty dq\, q^3 \frac{\langle|U(q)|^2\rangle \Phi_0''(q, \omega = 0)}{[1 + V(q)[1 - G(q)]X_0(q)]^2}. \quad (1b)$$

$\Phi_0(q, \omega)$ is the density–density correlation function of the free 2DEG for wave number q and frequency ω, and $X_0(q)$ is the Lindhard function in two dimensions [28].

The parameter A describes multiple scattering effects and is given by [22]

$$A = \frac{1}{4\pi N^2} \int_0^\infty dq\, q \frac{\langle|U(q)|^2\rangle X_0(q)^2}{[1 + V(q)[1 - G(q)]X_0(q)]^2}. \quad (1c)$$

For small impurity concentration and (or) high electron density, the parameter A is small and can be neglected. In this limit, the theory is described by the lowest order result σ_0. The conductivity becomes zero for $A = 1$, which means that for a fixed impurity density, a critical electron concentration N_c exists and the conductivity is zero for $N \leq N_c$. The condition $A = 1$ describes the MIT. For $N_c \approx 10^{11}$ cm^{-2}, we find $A = (N_c/N)^{1.7}$ and we conclude that A becomes small for $N \gg N_c$.

We have calculated A numerically by taking into account exchange and correlation via the LFC. For 10^{10} cm$^{-2} < N_c < 10^{12}$ cm^{-2}, we find, for the nonpolarized 2DEG,

$$N_c/N_i \approx 10.5[10^{11} \text{ cm}^{-2}/N_c]^{0.75} \qquad (2a)$$

and, for the fully polarized 2DEG,

$$N_c/N_i \approx 12.5[10^{11} \text{ cm}^{-2}/N_c]^{0.75}. \qquad (2b)$$

From Eq. (2) we conclude that for $N_c \approx 10^{11}$ cm^{-2}, as found in experiments [19], one impurity localizes about 11 electrons. This shows that the localized electrons are not bound to impurities, as in the hydrogen atom—localized states are different from bound states, and the physics of an impurity band is not appropriate in this case. If we neglect correlation effects and only take into account exchange effects, we find $N_c/N_i \approx 2.3[10^{11}$ cm$^{-2}/N_c]^{0.33}$ for the unpolarized 2DEG. We conclude that correlation effects are important in order to get realistic numbers for N_c.

In Fig. 1, we show N_i versus N_c for the unpolarized system and the fully polarized system. We see that, for a given N_i, the critical electron density N_c for the polarized system is larger than for the unpolarized electron gas, in agreement with experiments, and we find numerically $N_c(B \geq B_c) \approx 1.1 N_c(B = 0)$. This relation means that a magnetic field can suppress metallic behavior. From experiment it was deduced that $N_c(B \geq B_c) \approx 1.4 N_c(B = 0)$ [1]. We believe that finite extension effects (orbital effects), which lead to a larger effective mass for the 2DEG when a parallel magnetic field is applied [28], will increase $N_c(B \geq B_c)$.

The impurity density is not known from experiment. We determine N_i by the conductivity at high electron density $N \gg N_c$ using $\sigma \approx \sigma_0$. With N_i determined, the critical density N_c is defined by $A = 1$. In Fig. 2, we show the conductivity versus density for $N_i = 4 \times 10^9$ cm^{-2} in comparison with recent experimental results from [10].
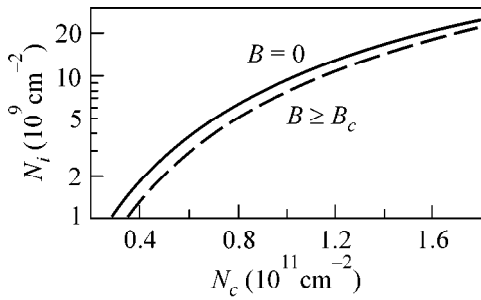
Fig. 1. Critical electron density N_c for a given impurity density N_i of a 2DEG in Si with no spin polarization (solid line) and with full spin polarization (dashed line).
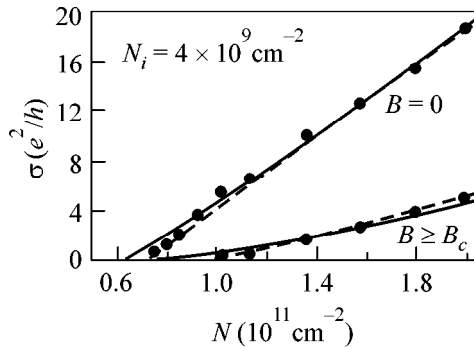

Fig. 2. Conductivity σ in units of e^2/h as a function of the electron density N for an impurity density $N_i = 4 \times 10^9$ cm^{-2} as solid lines. The unpolarized electron gas ($B = 0$) shows a higher conductivity than the polarized electron gas ($B \geq B_c$). The solid circles are experimental results [10] for inversion Si layers for $B = 0$ and $B \geq B_c$. The dashed lines represent our fits to the experimental data; see the text.
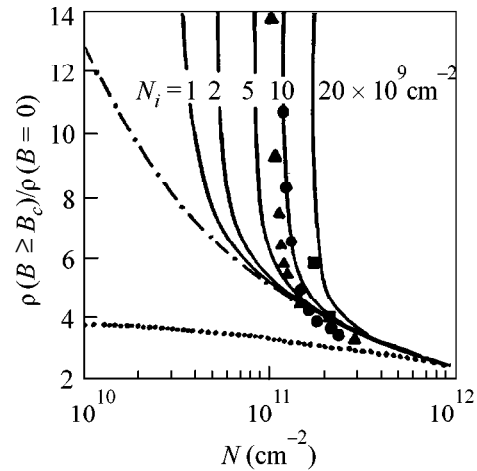

Fig. 3. Resistivity ratio $\rho(B \geq B_c)/\rho(B = 0)$ as a function of the electron density N for parameters corresponding to inversion Si layers. The dotted line represents the calculation within the random phase approximation. The dash–dotted line includes many-body effects (exchange and correlation) via the LFC. The solid lines include multiple scattering effects (the MIT), and the results for different impurity densities N_i are shown. The solid points represent experimental results for three different inversion Si layers: solid squares from Okamoto *et al.* [8], solid triangles from Pudalov *et al.* [10], and solid circles from Shashkin *et al.* [13].

At high electron densities ($N > 1.5 \times 10^{11}$ cm^{-2}), there is a good agreement, and even at lower densities good qualitative agreement is obtained. The conductivity scale for the unpolarized system is larger by about a factor of 4 than for the polarized system due to σ_0 [20]. The discrepancies between theory and experiment seen in Fig. 2 for $N < 1.5N_c$ are due to the fact that our theory is not able to predict the critical electron density for the MIT in *perfect* agreement with the experiment. The experimental data [10] can be fitted by $\sigma(B = 0) = 10.5(e^2/h)(N - N_c)/N_c$ with $N_c = 7.2 \times 10^{10}$ cm^{-2} and by $\sigma(B \geq B_c) = 4.8(e^2/h)[N - N_c]/N_c$ with $N_c = 9.8 \times 10^{10}$ cm^{-2}; see Fig. 2. We conclude that $N_c(B \geq B_c)/N_c(B = 0) = 1.36$, in reasonable agreement with earlier experimental results [1].

From our numerical results for A and σ_0 and $N < 1.5N_c$ (see Fig. 2), we get for the unpolarized electron gas ($B = 0$)

$$\sigma = \frac{e^2}{h}0.53\frac{N_c}{N_i}\left[\frac{N_c}{10^{11}\ \text{cm}^{-2}}\right]^{0.44}\left(\frac{N - N_c}{N_c}\right) \qquad (3a)$$

and for the polarized electron gas ($B \geq B_c$), we find

$$\sigma = \frac{e^2}{h}0.10\frac{N_c}{N_i}\left[\frac{N_c}{10^{11}\ \text{cm}^{-2}}\right]^{0.79}\left(\frac{N - N_c}{N_c}\right). \qquad (3b)$$

These results are in qualitative agreement with the conductivity near the MIT, as observed in the hole system of GaAs/Al$_x$Ga$_{1-x}$As [18].

In Fig. 3, we show the resistivity ratio $\rho(B \geq B_c)/\rho(B = 0)$ versus electron density. The lowest order result within the random phase approximation is shown by the dotted line. Exchange/correlation effects are taken into account for the dash–dotted line, where multiple scattering effects are neglected; and, in this approximation, the ratio $\rho(B \geq B_c)/\rho(B = 0)$ does not depend on the impurity density. Multiple scattering effects, which lead to a MIT, are taken into account for the solid lines. Experimental results [8, 10, 13] are in good agreement with the theory if we compare them with the solid line for $N_i \approx 1 \times 10^{10}$ cm^{-2}. The strong enhancement $\rho(B \geq B_c)/\rho(B = 0) \longrightarrow \infty$, seen in Fig. 3, is due to the MIT at N_c in the fully polarized 2DEG. It would be interesting to study inversion Si layers with an impurity density $N_i \approx 1 \times 10^9$ cm^{-2}. For such structures, the exchange correlation enhancement of $\rho(B \geq B_c)/\rho(B = 0)$ could be better observed than in the samples of [10] and [13]; see Fig. 3. We believe that the 2DEG in Si/Si$_{1-x}$Ge$_x$, where disorder effects are reduced by remote doping, is an ideal system for testing separately the interaction and disorder effects.

It was argued that finite width effects are important in GaAs/Al$_x$Ga$_{1-x}$As heterostructures [12] and lead to orbital effects, which are neglected in our model. Orbital effects have recently been discussed for a non-interacting 2DEG [31].

In conclusion, we have shown that our theory of the transport properties of an unpolarized and a polarized 2DEG, where strong disorder and interaction effects are taken into account, is in astonishing agreement with very recent experimental data on inversion Si layers.

REFERENCES

1. V. T. Dolgopolov, G. V. Kravchenko, A. A. Shashkin, and S. V. Kravchenko, Pis'ma Zh. Éksp. Teor. Fiz. **55**, 701 (1992) [JETP Lett. **55**, 733 (1992)].

2. D. Simonian, S. V. Kravchenko, M. P. Sarachik, and V. M. Pudalov, Phys. Rev. Lett. **79**, 2304 (1997).

3. V. M. Pudalov, G. Brunthaler, A. Prinz, and G. Bauer, Pis'ma Zh. Éksp. Teor. Fiz. **65**, 887 (1997) [JETP Lett. **65**, 932 (1997)].

4. D. Simonian, S. V. Kravchenko, M. P. Sarachik, and V. M. Pudalov, Phys. Rev. B **57**, R9420 (1998).

5. M. Y. Simmons, A. R. Hamilton, M. Pepper, *et al.*, Phys. Rev. Lett. **80**, 1292 (1998).

6. K. M. Mertes, D. Simonian, M. P. Sarachik, *et al.*, Phys. Rev. B **60**, R5093 (1999).

7. J. Yoon, C. C. Li, D. Shahar, *et al.*, Phys. Rev. Lett. **84**, 4421 (2000).

8. T. Okamoto, K. Hosoya, S. Kawaji, and A. Yagi, Phys. Rev. Lett. **82**, 3875 (1999).

9. T. Okamoto, K. Hosoya, S. Kawaji, *et al.*, cond-mat/9906425 (1999).

10. V. M. Pudalov, G. Brunthaler, A. Prinz, and G. Bauer, cond-mat/0004206 (2000).

11. S. A. Vitkalov, H. Zheng, K. M. Mertes, and M. P. Sarachik, cond-mat/0004201 (2000).

12. V. S. Khrapai, E. V. Deviatov, A. A. Shashkin, and V. T. Dolgopolov, cond-mat/0005377 (2000).

13. A. A. Shashkin, S. V. Kravchenko, V. T. Dolgopolov, and T. M. Klapwijk, cond-mat/0007402 (2000).

14. S. V. Kravchenko, G. V. Kravchenko, J. E. Furneaux, *et al.*, Phys. Rev. B **50**, 8039 (1994).

15. S. V. Kravchenko, W. E. Mason, G. E. Bowker, *et al.*, Phys. Rev. B **51**, 7038 (1995).

16. S. V. Kravchenko, D. Simonian, M. P. Sarachik, *et al.*, Phys. Rev. Lett. **77**, 4938 (1996).

17. S. V. Kravchenko and T. M. Klapwijk, Phys. Rev. Lett. **84**, 2909 (2000).

18. Y. Hanein, D. Shahar, J. Yoon, *et al.*, Phys. Rev. B **58**, R7520 (1998).

19. E. Abrahams, S. V. Kravchenko, and M. P. Sarachik, Rev. Mod. Phys. (in press); cond-mat/0006055 (2000).

20. V. T. Dolgopolov and A. Gold, Pis'ma Zh. Éksp. Teor. Fiz. **71**, 42 (2000) [JETP Lett. **71**, 27 (2000)].

21. K. S. Singwi and M. P. Tosi, Solid State Phys. **36**, 177 (1981).

22. A. Gold and W. Götze, Solid State Commun. **47**, 627 (1983); Phys. Rev. B **33**, 2495 (1986); A. Gold, Phys. Rev. Lett. **54**, 1079 (1985).

23. W. Götze, Solid State Commun. **27**, 1393 (1978); J. Phys. C **12**, 1279 (1979); Philos. Mag. B **43**, 219 (1981).

24. D. Belitz, A. Gold, and W. Götze, Z. Phys. B **44**, 273 (1981).

25. A. Gold, Appl. Phys. Lett. **54**, 2100 (1989).

26. A. Gold, Phys. Rev. B **44**, 8818 (1991).

27. A. Gold, Z. Phys. B **103**, 491 (1997).

28. T. Ando, A. B. Fowler, and F. Stern, Rev. Mod. Phys. **54**, 437 (1982).

29. G. G. Mahan, *Many-Particle Physics* (Plenum, New York, 1990).

30. P. A. Lee and T. V. Ramakrishnan, Rev. Mod. Phys. **57**, 287 (1985).

31. S. Das Sarma and E. H. Hwang, Phys. Rev. Lett. **84**, 5596 (2000).